NORTHWESTERN UNIVERSITY

Three problems in microfluidics: Electrokinetic instability, electrohydrodynamic self-assembly , and slip

A DISSERTATION

SUBMITTED TO THE GRADUATE SCHOOL
IN PARTIAL FULFILLMENT OF THE REQUIREMENTS

for the degree

DOCTOR OF PHILOSOPHY

Field of Mechanical Engineering

By

Hua-Yi Hsu

EVANSTON, ILLINOIS

DECEMBER 2008

ABSTRACT

Three problems in microfluidics: Electrokinetic instability, electrohydrodynamic self-assembly, and slip

Hua-Yi, Hsu

This thesis deals with three problems encountered in micro- and nano-fluidics: linear stability analysis of electrokinetic mixing in microchannels, development of a general purpose numerical technique for fully resolved simulation of electrohydrodynamic particulate flows, and studying the phenomenon of molecular scale slip next to boundaries in micro- and nano-channels.

Mixing in microscale devices is not easy due to the laminar flow conditions. Hence, various strategies are being proposed to mix fluids in microfluidic devices. One such approach is based on so-called electrokinetic instabilities.

Self-assembly can be an important means for micro/nanoscale fabrication. A fundamental understanding of this process is still missing. Such an understanding could help in developing better strategies to obtain optimal deposition pattern. One part of this thesis is focused on developing a fundamental numerical tool to investigate such problems.

In continuum fluid dynamics, the no-slip boundary condition is typically used. However, slip is typically reported in small scale devices. Slip can be helpful to reduce the flow resistance and thus reduce the energy requirement in micro- and nano-channels. In this thesis it is explored whether it is possible to reproduce molecular scale slip behavior through continuum equations. This approach leads to insights into the mechanism of slip in the context of continuum equations. It could also be useful in developing multiscale computational techniques.

ACKNOWLEDGMENTS

I would like to express my gratitude to all those who gave me the possibility to complete this thesis. I want to thank my advisor Professor Neelesh Patankar who gave me most help and guidance in all the time of research for and writing of this thesis. Graduate research assistantships from NSF through CAREER grant CTS-134546 to Prof. Patankar, and NER grant CMS-0304135 to Profs. Ruoff and Patankar are gratefully acknowledged. I also want to thank my family who gave me the most supports and strengths. Thanks for all my colleagues and friends, you guys acompany me to finish this long journey and always give me lots of assistance and encouragemtnts.

Table of Contents

References 103

List of Figuras

CHAPTER 1

Introduction

Fluid is a continuously deforming substance. To study fluid behavior there are two commonly used approaches: microscopic approach which is focused on molecular motion and macroscopic approach which considers local average movement over many molecules. To study the molecular motion, Molecular Dynamics (MD) is often used, however, it is computationally expensive if the fluid domain is not small. The continuum hypothesis has been used for solving macroscopic fluid problems. In this case, the fluid motion is described in terms of conservation equations for mass, momentum and energy. The no-slip boundary condition is typically applied for most fluid problems. During the past decade, micro and nano-scale technology has been developing. At this scale molecular scale effects may become important in capturing fluid behavior. However, often continuum theory has been successful in describing observed phenomena.

This thesis deals with three problems encountered in micro- and nano-fluidics: understanding electrokinetic mixing in microchannels, development of a general purpose numerical technique for fully resolved simulation of electrohydrodynamic particulate flows, and studying the phenomenon of molecular scale slip next to boundaries in micro- and nano-channels. Electrokinetic mixing is studied by linear stability analysis. The numerical technique for electrohydrodynamic particulate flow is based on a new immersed boundary algorithm [**4, 5**]. The problem of slip is focused on a novel approach to resolve molecular scale slip behavior by using continuum equations.

Mixing in microscale devices is not easy due to the laminar flow conditions. Hence, various strategies are being proposed to mix fluids in microfluidic devices. One such approach is based on so-called electrokinetic instabilities. Such instabilities are induced by an electric field applied in the presence of two miscible liquids with different electrical conductivities.

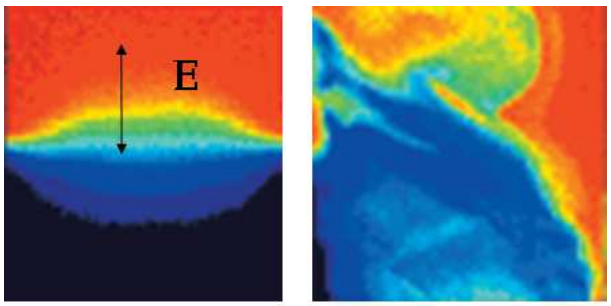

Figure 1.1. Mixing between two fluids with different conductivities. The external AC field is applied perpendicular to the interface inducing the instability that causes mixing [**6**].

Rapid mixing due to an electrokinetic instability can be induced beyond a critical threshold of the applied AC and/or DC electric field [**6, 7, 8**] (see Figure 1.1). However, mixing due to instabilities is not always desirable. Sometimes instabilities need to be avoided, e.g., in Field Amplified Sample Stacking (FASS)[**9, 10**]. It is critically important to understand the basic parameters that characterize these instabilities so that they could either be harnessed or controlled depending on the application. One objective of this thesis is to study such instabilities in electrolytic systems.

Carbon nanotubes (CNTs) have been studied since their discovery in 1991 [**11**]. In particular, carbon nanotubes (CNTs) can be used in nanoscale electronic devices[**12**] because of their unique electrical and mechanical properties[**13, 14**]. Self-assembly can be an important means for micro/nanoscale fabrication. J. Lee and co-workers have reported deposition of CNTs between two electrodes using a combination of AC and DC electric fields [**1**]. Figures (1.2) and (1.3) show that the deposition pattern of multiwalled carbon nanotubes (MWCNTs) is strongly dependent on the ratio of the DC and AC electric fields. A fundamental understanding of the deposition process is still missing. Such an understanding could help in developing better strategies to obtain optimal deposition pattern. One part of this thesis is focused on developing a fundamental numerical tool to investigate such problems.

In continuum fluid dynamics, the no-slip boundary condition is typically used at the walls. This implies that the fluid adjacent to the surface of a solid boundary moves at the same tangential velocity as the solid. Slip at the fluid-solid interface has been investigated

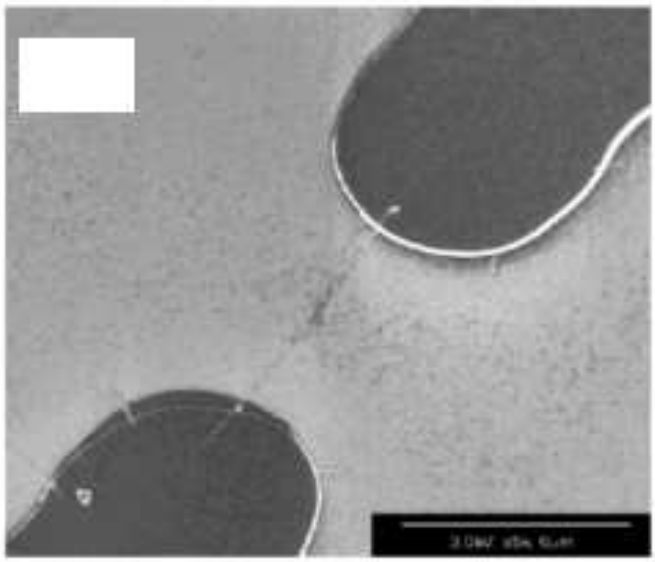

Figure 1.2. A MWCNT deposited between two non-flat electrodes [**1**].

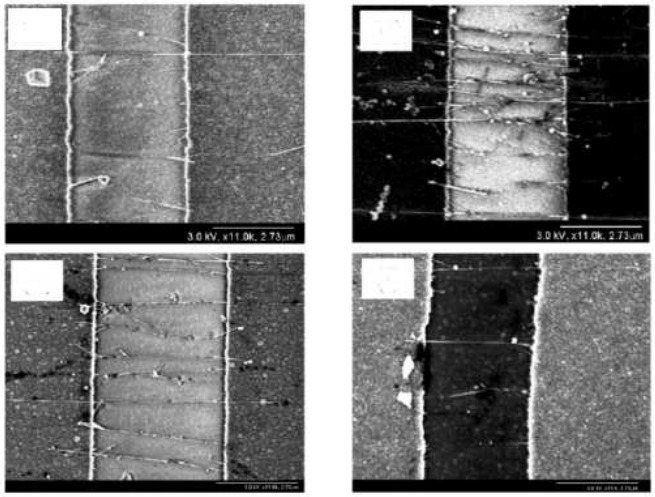

Figure 1.3. An SEM image of MWCNT deposition at different value of E_{dc}/E_{ac}. Top-left: $E_{dc}/E_{ac} = 0$, Top-right: $E_{dc}/E_{ac} = 0.41$, Bottom-left: $E_{dc}/E_{ac} = 0.32$, Bottom-right: $E_{dc}/E_{ac} = 0.22$ [**1**].

experimentally[**15, 16**], numerically, and analytically [**17, 18, 19, 20, 21, 3, 22, 23, 24, 25, 26**]. The resistance in micro and nano scale channels is large due to which it costs more energy to pump the liquid through the channel. In this case, slip next to the wall can be helpful to reduce the flow resistance and thus reduce the energy requirement.[**27, 28, 29, 30, 31**]

Molecular dynamic simulations have been useful to study the molecular scale slip behavior at the fluid-solid interface. The most common approach is the soft sphere model with

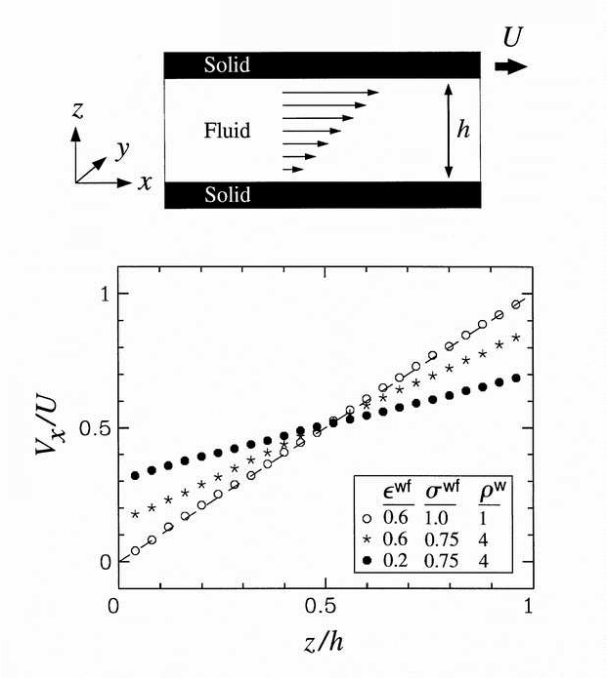

Figure 1.4. Results from molecular dynamic simulation of Couette flow [**2**]. The velocity of the top wall is 1 and the bottom wall is 0.

Lennard-Jones potential [**32, 2, 23, 18, 19**] (see Figure 1.4). However, MD simulations are computationally expensive. Specifically, for multiscale problems coupling molecular dynamic simulations at the fluid-solid interface with outer regions where continuum simulations are reasonable is a computational challenge. Hence, in this thesis it is explored whether it is possible to reproduce molecular scale slip behavior through continuum equations. It will be seen that continuum approach also leads to insights into the mechanism of slip.

Thus, the focus of this thesis is on the following three problems:

(1) Instabilities in electrolytic systems also called electrokinetic instabilities for strong electrolyte solutions. This is presented in Chapters 2 and 3.

(2) A numerical scheme to solve the motion of particles in electrohydrodynamic flows. This is presented in Chapter 4.

(3) In Chapter 5, the problem of slip is considered.

CHAPTER 2

The electrokinetic instability: Infinite domain

2.1. Introduction

Mixing of fluids in microfluidic devices is of interest in many applications. However, mixing in microchannels is difficult since the flow is laminar and in the Stokes regime (Re<<1). Thus, the need to enhance mixing has become an important issue.

The instability at the interface, between two miscible liquids with identical mechanical properties but different electrical conductivities, due to an external electric field has been observed and studied by Santiago and co-workers [**6, 33, 34, 8, 7, 35, 36**]. They called this the electrokinetic instability because the miscible liquids were highly conducting electrolyte solutions. They found that the flow was unstable no matter whether the externally applied electric field was parallel or perpendicular to the interface. It was found that when one electric field was applied, an instability was observed beyond a threshold value of the electric field (keeping the remaining parameters same) [**35**]. It was also found that the instability, with an external electric field perpendicular to the interface, was more unstable.

In this chapter the above instability is studied. Our work is focused on developing an analytic tool to characterize this instability. The methodology is based upon the work by Patankar [**37**]. He analyzed an instability where the electric field is parallel to the interface between two miscible liquids. We will consider below a case where the electric field is perpendicular to the interface. The objective is to find the appropriate parameters to describe this instability.

2.2. Governing equations

Two miscible liquids of identical mechanical properties but different electrical conductivities separated by a sharp interface is considered. Santiago and co-workers have modeled this

instability problem by using a diffuse interface in the base state and a convection-diffusion equation for the electrical conductivity [**6, 8, 7, 35**]. Patankar [**37**] has proposed a sharp interface assumption, which makes the analysis easier, and is useful to solve this same problem. The interface is defined with respect to the base state and it is an Eulerian surface. It is defined as the location of the sharp change in the electrical conductivity in the base state. The interface is fixed since it is independent of the perturbed state in the stability analysis.

An external electric field $\mathbf{E}$ is applied in the y-direction which is perpendicular to the interface, where $\mathbf{j}$ is the unit vector in the y-direction. Liquid a is above the interface, and Liquid b is below it (see Figure 2.1). The domain is infinite. The flow of liquids a and b is

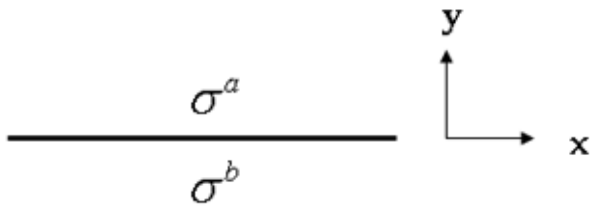

Figure 2.1. Geometry of the domain.

governed by the continuity and momentum equations.

$$\nabla \cdot \mathbf{u} = 0, \tag{2.1}$$

$$\rho \frac{\partial \mathbf{u}}{\partial t} + \rho(\mathbf{u} \cdot \nabla)\mathbf{u} = -\nabla p + \mu \nabla^2 \mathbf{u} + \rho_b \mathbf{E}, \tag{2.2}$$

where $\mathbf{u}$ is the velocity field, ρ is the density, p is the dynamic pressure (gravity is balanced by the hydrostatic component), and μ is the viscosity. The last term in Equation (2.2) is the external body force term due to the electrohydrodynamic force. The electric field is $\mathbf{E} = -\nabla\phi$, where ϕ is the electric potential. The bulk charge density ρ_b in the liquids is

$$\rho_b = \nabla \cdot (\varepsilon \mathbf{E}), \tag{2.3}$$

where ε is the permittivity. The material properties ρ, μ and ε are assumed to be the same and constant in both liquids a and b. The conservation of charge is given by

$$\frac{D\rho_b}{Dt} - \nabla \cdot (\sigma \nabla \phi) = 0, \tag{2.4}$$

where D/Dt denotes the material derivative. It is assumed that liquids a and b are strong electrolytes so that the electrical conductivities are high. As a result, the charge conservation equation becomes the current continuity equation given by

$$\nabla \cdot (\sigma \mathbf{E}) = 0, \tag{2.5}$$

where the electrical conductivity σ is different in liquids a and b. In electrolytes, the electrical conductivities depend on the concentration of the charged species and their mobilities [**38**]. For simplicity, it is assumed here that each of the liquids a and b are binary electrolytes made of the same two charged species. The concentrations of the charged species are different in the two liquids. Hence, the electrical conductivity in the two liquids will be different. It is further assumed that the two charged species have equal and opposite unit charge and that they have identical mobilities. It is now essential to identify the appropriate governing equation for the electrical conductivity. To that end it is useful to consider prior work which is discussed below.

The instability with the electric field parallel to the interface has been studied theoretically by Hoburg and Melcher [**39**]. In their analysis, they modeled the interface between the miscible liquids by a diffuse layer of exponentially varying electrical conductivity. It was assumed that the conductivity is governed by a hyperbolic equation

$$\frac{D\sigma}{Dt} = 0. \tag{2.6}$$

It was found that the configuration is always unstable even for small interface thickness. The analysis by Hoburg and Melcher [**39**] could not model the threshold for the instability as observed in experiments [**6, 35, 8, 7**]. To resolve this issue, Santiago and co-workers [**35, 8, 7**] considered a modified equation for σ that added a diffusion term to Equation

(2.6):

$$\frac{D\sigma}{Dt} = D_\sigma \nabla^2 \sigma, \tag{2.7}$$

where D_σ is the diffusion coefficient for the electrical conductivity and is assumed to be the same in both the liquids. They modeled the interface by a diffuse profile for the conductivity near the interface. Their linear stability analysis captured the threshold behavior observed in the experiments. Due to the above results in literature, in this work, we will consider Equation (2.7) as the governing equation for σ.

The governing equations for this problem can be summarized as follows:

$$\left.\begin{aligned} &\varepsilon \nabla^2 \phi = -\rho_b, \\ &\nabla \cdot (\sigma \mathbf{E}) = 0, \\ &\frac{D\sigma}{Dt} = D_\sigma \nabla^2 \sigma, \\ &\nabla \cdot \mathbf{u} = 0, \\ &\rho \frac{\partial \mathbf{u}}{\partial t} + \rho(\mathbf{u} \cdot \nabla)\mathbf{u} = -\nabla p + \mu \nabla^2 \mathbf{u} + \rho_b \mathbf{E}. \end{aligned}\right\} \tag{2.8}$$

The jump conditions, at the Eulerian interface defined above, corresponding to Equation (2.8) are listed below [**40**]

$$\rho_s = \|\varepsilon \mathbf{E}\| \cdot \mathbf{n}, \tag{2.9}$$

$$\|\sigma \mathbf{E}\| \cdot \mathbf{n} = 0, \tag{2.10}$$

$$\|\sigma \mathbf{u} - D_\sigma \nabla \sigma\| \cdot \mathbf{n} = 0, \tag{2.11}$$

$$\|\mathbf{u}\| \cdot \mathbf{n} = 0, \tag{2.12}$$

$$\mathbf{n} \cdot \|\boldsymbol{\tau} - \rho \mathbf{u}\mathbf{u}\| \cdot \mathbf{n} = 0, \text{and } \mathbf{t} \cdot \|\boldsymbol{\tau} - \rho \mathbf{u}\mathbf{u}\| \cdot \mathbf{n} = 0, \tag{2.13}$$

where $\boldsymbol{\tau} = -p\mathbf{I} + \mu(\nabla \mathbf{u} + \nabla \mathbf{u}^T) + \varepsilon \mathbf{E}\mathbf{E} - \frac{\varepsilon}{2}\mathbf{E} \cdot \mathbf{E}\mathbf{I}$, and $\|\|$ denotes the value of the variables at the interface in liquid a minus the value in liquid b. $\mathbf{n}$ is a unit normal to the interface pointing into liquid a. $\boldsymbol{\tau}$ is the electrohydrodynamic stress in the fluid which includes the Maxwell stress component given by $\varepsilon \mathbf{E}\mathbf{E} - \frac{\varepsilon}{2}\mathbf{E} \cdot \mathbf{E}\mathbf{I}$. Equation (2.9) gives the surface charge

density ρ_s at the interface which follows from Equation (2.3). Equation (2.10) states the current continuity at the interface which is from the equation of conservation of charge (Equation 2.5). Equation (2.11), which follows from Equation (2.7), plays a key role in the stability analysis since it introduces electrohydrodynamic coupling in the problem. Equation (2.12) shows the normal velocity continuity at the interface. Equation (2.13) is a result of the momentum equation at the interface.

2.3. Linear stability analysis

To study the instability, linear stability analysis will be done. An arbitrary perturbation can be a combination of sets of normal modes. This normal mode method will lead to an eigenvalue problem. The method of linear stability analysis includes sinusoidal perturbations on a base state, which is the flow whose stability is being investigated. For example, in the present study the perturbation for the x-component of velocity will be

$$u'(\mathbf{x}, t) = u(y)e^{-ikx+st}, \tag{2.14}$$

where $u(y)$ is a complex number, k is the wave number of the perturbation, and s is the growth rate. k is real while s can be complex. If the real part of $s > 0$, then it is an unstable mode.

2.3.1. Problem formulation

Figure (2.1) shows the flow domain. Semi-infinite domains are considered here in both liquids a and b. A sharp Eulerian interface is defined in the center of the domain. The material properties ρ, μ and ε are assumed to be the same and constant in both liquids a and b. Only the conductivities are different in liquid a and b. The base state has a flat interface parallel to the x-direction. The y-direction is perpendicular to the interface. Since the domain is unbounded and symmetric with respect to the z-direction, the problem is considered as a two-dimensional problem in the x-y plane. Assume that there is no electroosmotic flow in

the base state. The base solution is given by

$$
\left.
\begin{aligned}
&\mathbf{u_0} = \mathbf{0}, \\
&\rho_{b0} = 0, \\
&\sigma_0 = \sigma_0^a \quad \text{in liquid } a, \\
&\sigma_0 = \sigma_0^b \quad \text{in liquid } b, \\
&\mathbf{E_0}^a = \frac{I_0}{\sigma_0^a}\mathbf{j}, \qquad \mathbf{E_0}^b = \frac{I_0}{\sigma_0^b}\mathbf{j}, \\
&\rho_{s0} = -\frac{-\varepsilon_0 I_0 \Delta\sigma_0}{\sigma_0^a \sigma_0^b}, \\
&p_0^a = \frac{\varepsilon I_0^2}{2(\sigma_0^a)^2}, \qquad p_0^b = \frac{\varepsilon I_0^2}{2(\sigma_0^b)^2},
\end{aligned}
\right\} \tag{2.15}
$$

where ρ_{b0} is the bulk free charge per unit volume inside the fluid, ρ_{s0} is the charge per unit area at the interface, $\Delta\sigma_0 = \sigma_0^a - \sigma_0^b$, and subscript 0 denotes the variables in the base state. I_0 is a constant current in y-direction. A disturbed state is considered by superimposing a perturbation on the base solution. Note that the conductivity profile in the base state will diffuse with time. We introduce an approximation by assuming that the conductivity profile is "frozen" with a sharp jump at the interface. This is not a fully consistent approximation but it is found to be reasonable when the time scale of the instability is short [**35, 8**].

After linearization, the governing equations under the assumption of a "frozen" base state for the perturbations are

$$
\left.
\begin{aligned}
&\nabla \cdot \mathbf{u}' = 0, \\
&\varepsilon \nabla^2 \phi' = -\rho_b', \\
&\sigma_0 \nabla^2 \phi' - \frac{I_0}{\sigma_0}\frac{\partial \sigma'}{\partial y} = 0, \\
&\frac{\partial \sigma'}{\partial t} = D_\sigma \nabla^2 \sigma', \\
&\rho \frac{\partial \mathbf{u}'}{\partial t} = -\nabla p' + \mu \nabla^2 \mathbf{u}' + \rho_b' \mathbf{E_0}
\end{aligned}
\right\} \tag{2.16}
$$

where superscript $'$ denotes perturbations. The dimensional form of the perturbations is given by

$$\begin{pmatrix} \mathbf{u}' \\ p' \\ \phi' \\ \rho_b' \\ \sigma' \\ v_{\text{int}}' \end{pmatrix} = \begin{pmatrix} \mathbf{u}(y) \\ p(y) \\ \phi(y) \\ \rho_b(y) \\ \sigma(y) \\ v_{\text{int}} \end{pmatrix} e^{-ikx+st}, \tag{2.17}$$

where v_{int} is the y velocity component at the interface, k is the wave number of the perturbation, s is the growth rate, and $\mathbf{u}$, p, ϕ, ρ_b and σ are the amplitude of the perturbations, k is real while s can be complex. A positive real part of s implies an unstable mode. This approach leads to the condition for the onset of the temporal instability.

The governing equations are non-dimensionalized by using the following scales

$$\begin{aligned} &Length \rightarrow H, \phi' \rightarrow \frac{I_0 H}{\sigma_m}, E' \rightarrow \frac{I_0}{\sigma_m}, \rho_b' \rightarrow \frac{\varepsilon I_0}{H\sigma_m}, p' \rightarrow \frac{\varepsilon I_0^2}{\sigma_m^2} \\ &\sigma' \rightarrow \sigma_m (= \frac{(\sigma_0^a + \sigma_0^b)}{2}), Velocity \rightarrow \frac{H\varepsilon I_0^2}{\sigma_m^2 \mu}, time \rightarrow \frac{\mu \sigma_m^2}{\varepsilon I_0^2}. \end{aligned} \tag{2.18}$$

Since there is no geometric length scale in this problem, the inverse of the wave number k of the perturbation is chosen as the length scale i.e. $H = 1/k$. The velocity scale is obtained by balancing the viscous and electrical forces in the momentum equation. After non-dimensionalization, the perturbation equations become

$$\left.\begin{aligned} &\nabla \cdot \mathbf{u}' = 0, \\ &\nabla^2 \phi' = -\rho_b', \\ &\sigma_{0N}^2 \nabla^2 \phi' - \frac{\partial \sigma'}{\partial y} = 0, \\ &Pe \frac{\partial \sigma'}{\partial t} = \nabla^2 \sigma', \\ &Re \frac{\partial \mathbf{u}'}{\partial t} = -\nabla p' + \nabla^2 \mathbf{u}' + \frac{\rho_b'}{\sigma_{ON}} \mathbf{j}. \end{aligned}\right\} \tag{2.19}$$

where same symbols have been retained for the non-dimensional variables.

The non-dimensional parameters in the governing equations are

$$\left.\begin{aligned} Re &= \frac{\rho\varepsilon I_0^2}{\mu^2\sigma_m^2 k^2}, \\ Pe &= \frac{\varepsilon I_0^2}{\mu D_\sigma \sigma_m^2 k^2}, \\ \sigma_{0N} &= \frac{2\sigma_0}{\sigma_0^a + \sigma_0^b}, \end{aligned}\right\} \tag{2.20}$$

where Re is the Reynold's number, Pe is the Peclet number which is a ratio of convection and diffusion terms, and σ_{0N} is the non-dimensionalized value of σ_0 in each liquid.

In the non-dimensional form of Equation (2.17), we put $k = 1$ since the length is non-dimensionalized by $1/k$, and s will be understood to be non-dimensionalized by the inverse of the time scale. Inserting the non-dimensional form of Equation (2.17) into Equation (2.19) and simplifying we get

$$\left.\begin{aligned} &(D^2 - 1 - Pes)\sigma = 0, \\ &(D^2 - 1)\phi = \frac{D\sigma}{\sigma_{ON}^2}, \\ &(D^2 - 1 - Res)(D^2 - 1)\upsilon = -\frac{D\sigma}{\sigma_{ON}^3}, \\ &u = -iD\upsilon, \\ &p = (D^2 - 1 - Res)D\upsilon, \end{aligned}\right\} \tag{2.21}$$

where s is the non-dimensional growth rate, D denotes the derivative with respect to y, and u, v are the x, y components of velocity respectively. The solution of Equation (2.21) along the y-direction as $y \to \pm\infty$ in liquids a and b, respectively, should approach zero. This gives the following solutions for liquids a and b

$$\left.\begin{aligned} \sigma^a &= A^a e^{-\lambda y}, \\ \phi^a &= B^a e^{-y} + \frac{D\sigma^a}{(\sigma_{0N}^a)^2(Pes)}, \\ \upsilon^a &= C^a e^{-y} + D^a e^{-qy} - \frac{D\sigma^a}{(Pes - Res)(Pes)(\sigma_{0N}^a)^3}, \end{aligned}\right\} \tag{2.22}$$

$$\left.\begin{aligned} \sigma^b &= A^b e^{\lambda y}, \\ \phi^b &= B^b e^y + \frac{D\sigma^b}{(\sigma^b_{0N})^2(Pes)}, \\ v^b &= C^b e^y + D^b e^{qy} - \frac{D\sigma^b}{(Pes - Res)(Pes)(\sigma^b_{0N})^3}, \end{aligned}\right\} \tag{2.23}$$

where λ and q are positive and are given by

$$\left.\begin{aligned} \lambda &= \sqrt{1 + Pes}, \\ q &= \sqrt{1 + Res}. \end{aligned}\right\} \tag{2.24}$$

Superscripts a or b denote liquids a or b, respectively. A, B, C and D's with superscript are constants.

The linearized jump conditions for the electrical conductivity at the interface are given by

$$\left.\begin{aligned} \|\sigma\| &= 0, \\ \|D\sigma\| &= Pev_{\text{int}}\Delta\sigma_{ON}, \end{aligned}\right\} \tag{2.25}$$

where $v_{\text{int}} = v^a = v^b = \dfrac{(v^a + v^b)}{2}$ at $y = 0$ is the amplitude of the non-dimensional perturbation velocity at the interface, and $\Delta\sigma_{ON} = \sigma^a_{ON} - \sigma^b_{ON}$. The jump conditions in Equation (2.25) follow by assuming that there is no self-sharpening mechanism that creates discontinuities in the electrical conductivity. This is reasonable, since the diffusive behavior of σ is important in this problem [**40**]. The second jump condition in Equation (2.25) follows from Equation (2.11). Using these conditions, we get the solution for A^a and A^b as

$$A^a = A^b = -\frac{Pev_{\text{int}}\Delta\sigma_{ON}}{2\lambda}. \tag{2.26}$$

To solve for B^a and B^b, we use the interface jump conditions for the electric potential:

$$\left.\begin{aligned} \|\phi\| &= 0, \\ \|\sigma_{ON} D\phi\| + \sigma_{y=0}\frac{\Delta\sigma_{0N}}{\sigma^a_{0N}\sigma^b_{0N}} &= 0. \end{aligned}\right\} \tag{2.27}$$

The first jump condition in Equation (2.27) follows by assuming that no double layers are formed at the interface. This is reasonable since the interface is not insulating and the current carrying species can pass from one side of the interface to the other [**40**]. The second jump condition in Equation (2.27) follows from Equation (2.10). Thus, B^a and B^b are

$$B^a = \frac{Pev_{\text{int}} \triangle \sigma_{0N}^2}{4\sigma_{0N}^a \sigma_{0N}^b (\lambda^2 - 1)\lambda} - \frac{Pev_{\text{int}} \triangle \sigma_{0N} (\sigma_{0N}^{a2} + \sigma_{0N}^{b2})}{4(\lambda^2 - 1)\sigma_{0N}^a \sigma_{0N}^{b2}}, \tag{2.28}$$

$$B^b = \frac{Pev_{\text{int}} \triangle \sigma_{0N}^2}{4\sigma_{0N}^a \sigma_{0N}^b (\lambda^2 - 1)\lambda} + \frac{Pev_{\text{int}} \triangle \sigma_{0N} (\sigma_{0N}^{a2} + \sigma_{0N}^{b2})}{4(\lambda^2 - 1)\sigma_{0N}^{a2} \sigma_{0N}^b}. \tag{2.29}$$

The linearized jump conditions for the velocity (from Equation 2.12) and the stress (from Equation 2.13) at $y = 0$ give

$$\left.\begin{aligned} \|v\| &= 0, \\ \|u\| &= 0, \\ \| - p + 2Dv - \frac{D\phi}{\sigma_{0N}} \| &= 0, \\ \|D^2 v + v - \frac{\phi}{\sigma_{0N}} \| &= 0. \end{aligned}\right\} \tag{2.30}$$

Note that the jump condition for u is due to the no-slip condition. This is reasonable since no double-layers are formed at the interface. Inserting the solutions for velocity in Equations (2.22) and (2.23) into Equation (2.30), we get five equations for five unknowns: C^a, C^b, D^a, D^b, and v_{int}. All the equations are homogeneous. The equations can be represented in the following matrix form

$$\begin{pmatrix} 1 & -1 & 1 & -1 & f_1 \\ 1 & 1 & q & q & f_2 \\ 1 & 1 & q^3 & q^3 & f_3 \\ 1 & -1 & q & q^2 & f_4 \\ 1 & 1 & 1 & 1 & f_5 \end{pmatrix} \begin{pmatrix} C^a \\ C^b \\ D^a \\ D^b \\ v_{\text{int}} \end{pmatrix} = \begin{pmatrix} 0 \\ 0 \\ 0 \\ 0 \\ 0 \end{pmatrix} \tag{2.31}$$

$$f_1 = -\frac{Pe\Sigma(\Gamma-2)}{2(\lambda^2-1)(\lambda^2-q^2)}\sqrt{\frac{\Gamma-3}{\Gamma+1}}, \tag{2.32}$$

$$f_2 = \frac{\lambda Pe\Sigma\Gamma}{2(\lambda^2-1)(\lambda^2-q^2)}, \tag{2.33}$$

$$f_3 = \frac{\lambda^3 Pe\Gamma}{2(\lambda^2-1)(\lambda^2-q^2)} + \frac{Pe\Gamma}{2(\lambda^2-1)}(\frac{1}{\lambda} + (\Gamma-1) - \lambda\Gamma), \tag{2.34}$$

$$f_4 = \frac{\lambda^2 Pe\Sigma(\Gamma-2)}{2(\lambda^2-1)(\lambda^2-q^2)}\sqrt{\frac{\Gamma+1}{\Gamma-3}} + \frac{Pe\Gamma}{2(\lambda^2-1)}\sqrt{\frac{\Gamma-3}{\Gamma+1}}$$

$$+ \frac{Pe\Sigma(\Gamma-1)^2}{2(\lambda^2-1)\sqrt{(\Gamma+1)(\Gamma-3)}} - \frac{Pe\Sigma(\Gamma-2)}{2(\lambda^2-1)}\sqrt{\frac{\Gamma+1}{\Gamma-3}}, \tag{2.35}$$

$$f_5 = \frac{Pe\Sigma\Gamma}{2(\lambda^2-1)(\lambda^2-q^2)} - 2. \tag{2.36}$$

where $\Sigma = \frac{\Delta\sigma_{0N}^2}{\sigma_{0N}^{a2}\sigma_{0N}^{b2}}$ and $\Gamma = \frac{\sigma_{0N}^a}{\sigma_{0N}^b} + \frac{\sigma_{0N}^b}{\sigma_{0N}^a} + 1$. Setting the determinant of the matrix to zero gives the dispersion equation. All symbolic manipulations were done using Mathematica.

2.3.2. The critical condition for instability

The dispersion equation obtained from manipulations in Mathematica is

$$-(4\Gamma(1+\sqrt{1+ST})((1+S)^{\frac{3}{2}}\sqrt{1+ST}+$$

$$\sqrt{1+S}(1+ST)+(1+S)\sqrt{1+ST}(1+\sqrt{1+ST})))$$

$$+P_\Sigma(\sqrt{1+S}-\Gamma\sqrt{1+S}+\sqrt{1+ST})=0, \tag{2.37}$$

where $S = Pes$, $P_\Sigma = Pe\Sigma\Gamma$, and $T = \frac{Re}{Pe}$. The maximum growth rate for this problem is the largest root of the dispersion equation. It can be verified that the maximum growth rate is positive and real.

When the system is marginally stable i.e. when the maximum growth rate $S = 0$, then P_Σ is found to be independent of T and is a function of Γ. The marginal stability condition

gives the critical condition for the onset of the instability. It is given by

$$\left.\begin{aligned} P_{\Sigma}^{cri} &= \frac{32\Gamma}{\Gamma-2}, \\ \Rightarrow (\frac{\varepsilon {E_{\text{mean}}}^2}{D_\sigma \mu k^2})^{cri} &= \frac{32}{(\Gamma-2)\Sigma}, \end{aligned}\right\} \tag{2.38}$$

where $E_{\text{mean}} = \dfrac{I_0}{\sigma_m}$. Equation (2.38) gives the critical electric field for the instability of a mode of wave number k, when the material properties of the liquids are given. Figure (2.2) shows a plot of P_{Σ}^{cri} as a function of Γ.

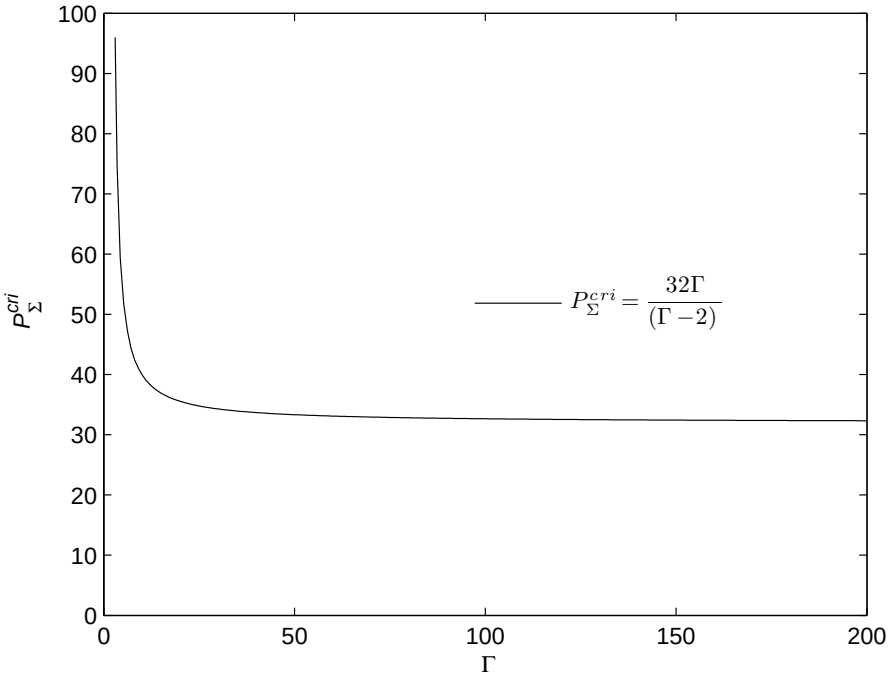

Figure 2.2. The marginal stability curve (P_{Σ}^{cri} vs. Γ) identifying the critical condition for the onset of instability.

2.3.3. The mechanism of instability

Figure (2.3) shows a plot of the streamlines for a typical unstable mode. The streamfunction plotted in Figure (2.3) is given by $\psi = Real|-iv(y)e^{-ix}|$. The parameters are $T = 0.05$, $S = 25$, $P_\Sigma = 683.3914$, $\dfrac{\sigma_{0N}^a}{\sigma_{0N}^b} = 10$, and $\Gamma = 11.1$. The $y = 0$ line is the Eulerian interface and one wavelength of the unstable mode is plotted. The higher conductivity fluid occupies

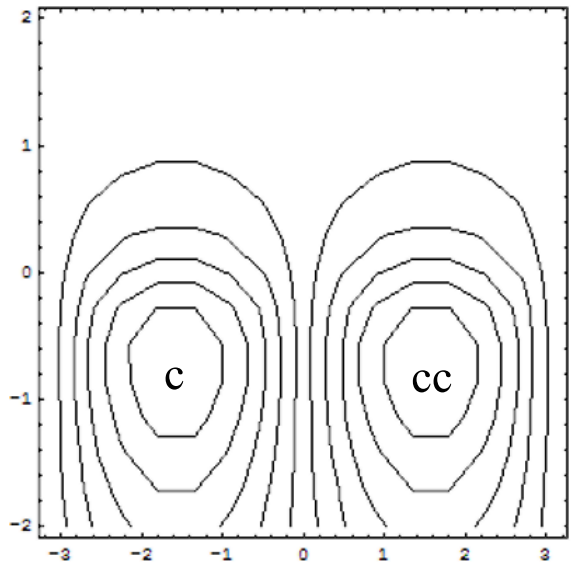

Figure 2.3. Streamlines of an unstable mode in an infinite domain where the applied electric field is perpendicular to the interface between the two liquids. Clockwise rotation of the fluid is denoted by 'c' and counterclockwise rotation is denoted by 'cc'.

the upper part ($y > 0$) and the lower conductivity is in the lower part ($y < 0$). Two counter-rotating cells of the fluid that are asymmetric with respect to the Eulerian interface $y = 0$ are found.

To elucidate the mechanism of the instability, we consider a perturbation velocity at the Eulerian interface $v'_{\text{int}} = cos(x)$. The velocity disturbance at the interface leads to a perturbation field for the conductivity due to the electrohydrodynamic coupling in the interface condition given by Equation (2.25). The perturbation to the electrical conductivity is obtained from Equations (2.22), (2.23) and (2.26):

$$\sigma'^{a} = -\frac{Pe\Delta\sigma_{ON}}{2\lambda}e^{-\lambda y}cos(x), \qquad \sigma'^{b} = -\frac{Pe\Delta\sigma_{ON}}{2\lambda}e^{\lambda y}cos(x). \tag{2.39}$$

It follows from Equation (2.39) that a region of lower electrical conductivity is formed when v_{int} is maximum, and higher electrical conductivity is formed when v_{int} is minimum. This is depicted in Figure (2.4) with vertical bold arrows at locations of maximum and minimum velocities.

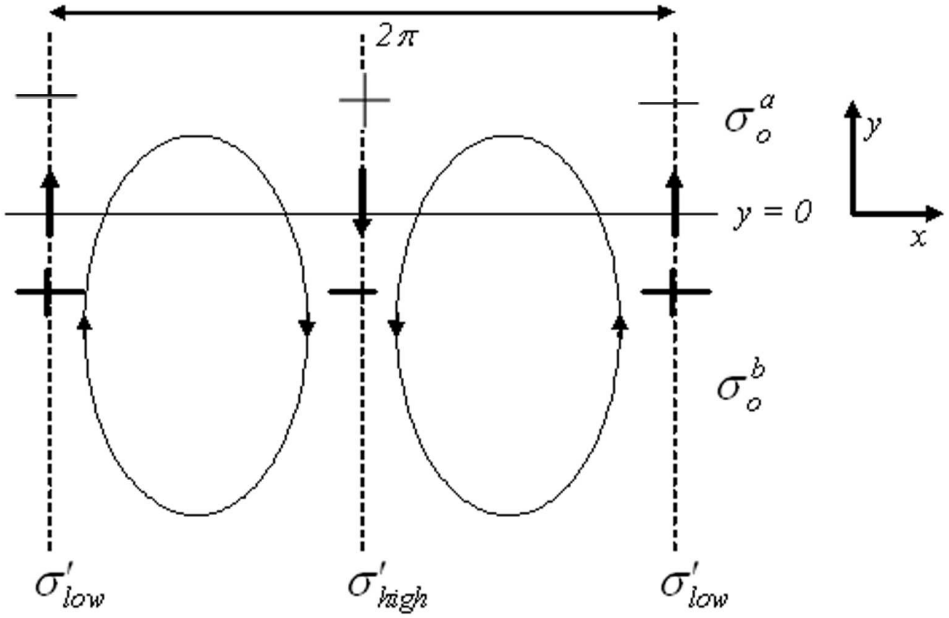

Figure 2.4. A schematic depicting the key aspects of the mechanism of instability. One wavelength of the perturbation field is shown. The Eulerian interface is located at $y = 0$. Liquid a in the upper half ($y > 0$) has greater electrical conductivity in the base state. The bold arrows on the Eulerian interface indicate the perturbation velocity at the interface. The x locations of high and low values of the perturbed electrical conductivity are shown. The positive and negative signs indicate the bulk charge in the domain. Bold signs indicate greater bulk charge for $y < 0$.

The second and third of Equation (2.19) imply $\rho'_b = -\frac{1}{\sigma_{ON}^2}\frac{\partial \sigma'}{\partial y}$. Thus, a negative bulk charge density is formed in regions where the conductivity increases with respect to the y-direction, and a positive bulk charge density is formed where the conductivity decreases with respect to the y-direction. The bulk charge density is created because of the diffusive equation for the electrical conductivity which also causes the electrohydrodynamic coupling. For the case being considered here, the perturbation bulk charge density in the two liquids is given by

$$\rho_b'^a = -\frac{Pe\Delta\sigma_{ON}}{2\sigma_{ON}^{a2}} e^{-\lambda y} cos(x), \qquad \rho_b'^b = \frac{Pe\Delta\sigma_{ON}}{2\sigma_{ON}^{b2}} e^{\lambda y} cos(x). \tag{2.40}$$

Equation (2.40) implies that at a given distance from the Eulerian interface and a given x location, the magnitude of the bulk charge density in Liquid a is much smaller than the

corresponding value in Liquid b. In addition, the charges have opposite signs (see Figure 2.4). This gives an asymmetric distribution of the perturbation bulk charge density in the fluid domain and leads to a body force in the momentum equations for both liquids (see Equation 2.19). The body force due to the bulk charge is dominant in Liquid b and is in the direction of the initial perturbation velocity at the interface (see Figure 2.4). This gives rise to a cellular flow that reinforces the initial perturbation thus resulting in an instability shown in Figure (2.3).

2.3.4. Comparison with the parallel electric field case

It has been reported that when the electric field is applied perpendicular to the interface the system is more unstable compared to the parallel electric field case [**6**].

We consider this issue by comparing the critical condition for instability for these cases. The critical condition for the instability of the parallel electric field case is given by [**37**],

$$\left.\begin{aligned} P_{\Sigma\parallel}^{cri} &= 32, \\ \Rightarrow (\frac{\varepsilon {E_0}^2}{D_\sigma \mu k^2})^{cri} &= \frac{32}{\Sigma_\parallel}, \end{aligned}\right\} \tag{2.41}$$

where $\Sigma_\parallel = \dfrac{\Delta\sigma_{0N}^2}{\sigma_{0N}^a \sigma_{0N}^b}$. Comparison between Equations (2.38) and (2.41) implies that the perpendicular electric field case is more unstable compared to the parallel electric field case. This is discussed below.

Consider parameters: $\sigma^a/\sigma^b = 10$, $\mu = 0.001 kg/ms$, $\varepsilon = 6.9 \times 10^{-10} C/Vm$, $\rho = 1000 kg/m^3$, and $D_\sigma = 10^{-9} m^2/s$. We express Σ's in terms of σ_a and σ_b rather than σ_{0N}^a and σ_{0N}^b in both parallel and perpendicular electric field cases, Thus

$$\Sigma_\parallel = \frac{(\sigma^a - \sigma^b)^2}{\sigma^a \sigma^b} = 8.1. \tag{2.42}$$

Using equation (2.41), we get

$$(\frac{\varepsilon {E_0}^2}{D_\sigma \mu k^2})^{cri} = \frac{32}{8.1} \approx 3.95. \tag{2.43}$$

For the perpendicular electric field case, we have

$$\left.\begin{aligned} \Sigma &= \left(\frac{(\sigma^a)^2 - (\sigma^b)^2}{2\sigma^a\sigma^b}\right) = 24.5025, \\ \Gamma &= \frac{\sigma^a}{\sigma^b} + \frac{\sigma^b}{\sigma^a} + 1 = 11.1. \end{aligned}\right\} \tag{2.44}$$

Using equation (2.38), we get

$$\left(\frac{\varepsilon E\text{mean}^2}{D_\sigma \mu k^2}\right)^{cri} = \frac{32}{\Sigma(\Gamma - 2)} = \frac{32}{24.5025 \times 9.1} \approx 0.143. \tag{2.45}$$

Comparing Equations (2.43) and (2.45), we see that the electric field needed to achieve the instability state in the parallel case is large than the perpendicular electric field case. Thus, we conclude that the perpendicular case is more unstable than the parallel case.

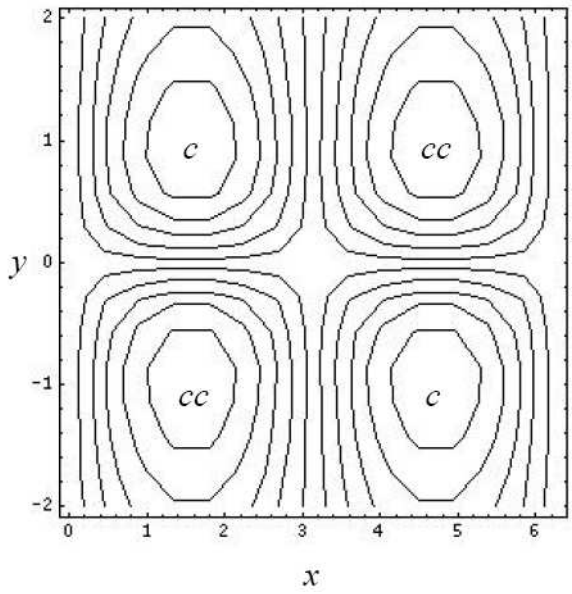

Figure 2.5. Streamlines of an unstable mode in infinite domain where the applied electric field is parallel to the interface between the two liquids [**37**].

This difference is due to the difference in the flow pattern in the unstable modes. Figure (2.5) shows that the parallel electric field case has a different cellular flow pattern in the unstable mode [**37**]. Two pairs of counter rotating vortices are produced in the parallel electric field case. This flow pattern is much less asymmetric and gives rise to weaker flows. In the perpendicular electric field case the asymmetry is much stronger primarily due to

the current flowing perpendicular to the interface in the base state. This results in stronger destabilizing forces in the perpendicular electric field case thus making it more unstable.

2.4. Conclusion

In this chapter the instability at the interface between two miscible liquids with identical mechanical properties but different electrical conductivities was analyzed. Linear stability analysis was done by considering a sharp interface between adjacent liquids in the base state. This approach enabled, for the first time, an analytic solution for the critical condition of the electrokinetic instability. For the perpendicular electric field case, it was seen that the instability depends on a non-dimensional parameter P_Σ defined in the Equation (2.38). This parameter was not identified in any of the prior studies.

This approach also enabled an analysis of the mechanism of instability which was not clearly understood from prior work. Specifically, it was found that any velocity perturbation at the interface leads to a varying electrical conductivity in its vicinity due to the electrohydrodynamic coupling in the following interface condition

$$\|\sigma\mathbf{u} - D_\sigma \nabla\sigma\| \cdot \mathbf{n} = 0. \tag{2.46}$$

The above interface condition as the source of electrohydrodynamic coupling was not previously identified. This in turns leads to a bulk charge density that gives a body force in the fluid equations. The body force generates a cellular motion that results in the instability.

We showed, consistent with prior experimental results, that the perpendicular electric field case is more unstable compared to the parallel electric field case. The reason for this is the greater asymmetry in the perpendicular field case that results in larger destabilizing electrohydrodynamic force.

Detailed experimental investigation of the perpendicular electric field case is not available in literature at this time. Hence, a quantitative comparison with experiments is not possible in this case like it was possible for the parallel electric field case [**37**].

Typical experimental devices have microchannels. In the analysis in this chapter we did not consider the effect of a microchannel geometry on the instability. This will be considered in the next chapter.

CHAPTER 3

The electrokinetic instability: Shallow channel

In this chapter we extend the linear stability analysis introduced in the previous chapter to the case of a shallow microchannel geometry that is typical in microfluidic devices [**6, 35**]. The objective is to quantify the influence of the device geometry on the instability.

3.1. Problem formulation

The shallow channel geometry is shown in Figure (3.1). The domain is unbounded in the x-direction. The depth of the channel is $2d$ which is much smaller than the width $2H$. There is an external electrical field applied perpendicular to the interface (y-direction) between two liquids a and b. Assume that there is no electroosmotic flow, and there is no charge in the base state. The base state is the same as that in Equation (2.15). As noted in the previous chapter, the perturbations are governed by the following equations

$$\left.\begin{aligned} &\nabla \cdot \mathbf{u}' = 0, \\ &\varepsilon \nabla^2 \phi' = -\rho_b', \\ &\sigma_0 \nabla^2 \phi' - \frac{I_0}{\sigma_0}\frac{\partial \sigma'}{\partial y} = 0, \\ &\frac{\partial \sigma'}{\partial t} = D_\sigma \nabla^2 \sigma', \\ &\rho \frac{\partial \mathbf{u}'}{\partial t} = -\nabla p' + \mu \nabla^2 \mathbf{u}' + \rho_b' \mathbf{E_0}. \end{aligned}\right\} \tag{3.1}$$

The governing equations are non-dimensionalized by using the following scales

$$\begin{aligned} &x, y \to H, z \to d, \phi' \to \frac{I_0 H}{\sigma_m}, E' \to \frac{I_0}{\sigma_m}, \rho_b' \to \frac{\varepsilon I_0}{H \sigma_m}, p' \to \frac{\varepsilon I_0^2}{\sigma_m^2}, \\ &\sigma' \to \sigma_m (= \frac{(\sigma_0^a + \sigma_0^b)}{2}), Velocity \to \frac{H \beta^2 \varepsilon I_0^2}{\sigma_m^2 \mu}, time \to \frac{\mu \sigma_m^2}{\beta^2 \varepsilon I_0^2}. \end{aligned} \tag{3.2}$$

where $\beta = d/H << 1$ for a shallow channel.

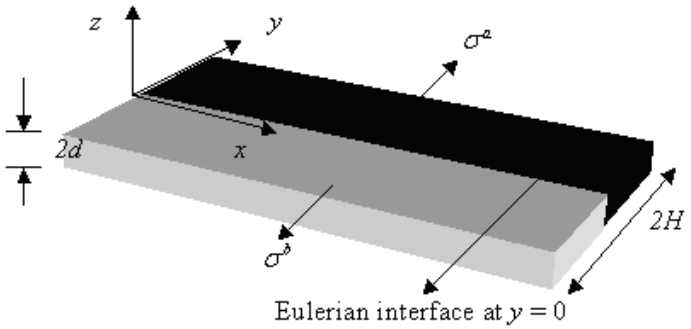

Figure 3.1. The shallow channel geometry.

For a shallow channel, Hele-Shaw equations for the perturbations can be obtained by considering the limit $\beta \to 0$ in the governing equations. It follows that, in the leading order, $\phi' = \phi'(x, y)$, $\sigma' = \sigma'(x, y)$, and $\rho_b' = \rho_b'(x, y)$. To arrive at this form it is assumed that $\partial\phi'/\partial z = \partial\sigma'/\partial z = 0$ at the top and bottom walls. These conditions imply that the walls are insulating and that the charged species do not penetrate the walls, respectively. Both conditions are realistic. This leads to a two-dimensional problem for ϕ', σ' and ρ_b' in the $x-y$ plane.

The fluid equations in the Hele-Shaw limit imply that, to the leading order, the velocity component in the vertical direction is zero and the pressure $p' = p'(x, y)$. The horizontal velocity in the $x-y$ plane, to the leading order, is of the form $\mathbf{u}'(x, y, z) = 1.5(1-z^2)\mathbf{u}_m'(x, y)$ [**41, 35**], where the variables are non-dimensional. The velocity vector has only $x - y$ components and $\mathbf{u}_m'$ is the perturbation velocity at a given location that is averaged with respect to the z direction. This form assumes that the viscous stress due to the change of $\mathbf{u}'$ in the z direction dominates over changes in the other directions. Thus, the velocity profile is locally parabolic with respect to the z direction (the lubrication approximation). Using

these approximations, the governing equations become

$$\left.\begin{aligned} &\nabla_H \cdot \mathbf{u}'_m = 0, \\ &\nabla_H^2 \phi' = -\rho'_b, \\ &\sigma_{0N}^2 \nabla_H^2 \phi' - \frac{\partial \sigma'}{\partial y} = 0, \\ &Pe \frac{\partial \sigma}{\partial t} = \nabla_H^2 \sigma, \\ &Re\beta^2 \frac{\partial \mathbf{u}'_m}{\partial t} = -\nabla p' + \beta^2 \nabla_H^2 \mathbf{u}'_m - 3\mathbf{u}'_m + \frac{\rho'_b}{\sigma_{ON}} \mathbf{j}, \end{aligned}\right\} \tag{3.3}$$

where ∇_H denotes the gradient in the $x - y$ plane. All variables carry same meaning as in the previous chapter unless specified. The non-dimensional parameters are given by

$$\left.\begin{aligned} Re &= \frac{\beta^2 H^2 \rho \varepsilon I_0^2}{\mu^2 \sigma_m^2}, \\ Pe &= \frac{\beta^2 H^2 \varepsilon I_0^2}{\mu D_\sigma \sigma_m^2}, \\ \sigma_{0N} &= \frac{2\sigma_0}{\sigma_0^a + \sigma_0^b}, \end{aligned}\right\} \tag{3.4}$$

where σ_0 is as defined in the previous chapter.

It should be noted that the terms involving β^2 in the last of equation (3.3) should be dropped in the Hele-Shaw limit. However, Chen *et al.* [**35**] recommend, based on their work on the parallel electric field case, that those terms be retained to approximately capture the viscous effects due to the flow in the $x - y$ plane. This is clearly not a fully consistent formulation and they refer to this as the modified Hele-Shaw formulation [**35**]. A rigorous analysis will require the matching of the "inner" solution in the thin viscous layers near the vertical walls with the "outer" Hele-Shaw solution. Such an analysis will not be considered here. Instead, following Chen *et al.* [**35**], an approximate approach based on Equation (3.3) will be considered where the inertia and the horizontal viscous terms are retained.

The novelty of our effort is the use of a sharp interface approach in the linear stability analysis. Assuming perturbations of the form given by Equation (2.17) the governing

equations become

$$\left.\begin{aligned}
&(D^2-k^2-Pes)\sigma=0,\\
&(D^2-k^2)\phi=\frac{D\sigma}{\sigma_{ON}^2},\\
&(D^2-k^2-Res-\frac{3}{\beta^2})(D^2-k^2)v_m-\frac{k^2D\sigma}{\beta^2\sigma_{ON}^3},\\
&u_m=-\frac{iDv_m}{k},\\
&p=\frac{(\beta^2(D^2-k^2)-\beta^2 s-3)Dv_m}{k^2},
\end{aligned}\right\} \tag{3.5}$$

where we use the same notation as in the previous chapter unless stated otherwise. Solutions of the governing equations are given by

$$\left.\begin{aligned}
\sigma^a &= A^a\sinh\lambda y+B^a\cosh\lambda y,\\
\phi^a &= C^a\sinh\lambda y+D^a\cosh\lambda y+\frac{D\sigma^a}{(\sigma_{0N}^a)^2(\lambda^2-k^2)},\\
v^a &= E^a\sinh\lambda y+F^a\cosh\lambda y+G^a\sinh\lambda y+H^a\cosh\lambda y\\
&\quad -k^2\frac{D\sigma^a}{\beta^2(\sigma_{0N}^a)^3(\lambda^2-q^2)(\lambda^2-k^2)},
\end{aligned}\right\}$$

$$\left.\begin{aligned}
\sigma^b &= A^b\sinh\lambda y+B^b\cosh\lambda y,\\
\phi^b &= C^b\sinh\lambda y+D^b\cosh\lambda y+\frac{D\sigma^b}{(\sigma_{0N}^b)^2(\lambda^2-k^2)},\\
v^b &= E^b\sinh\lambda y+F^b\cosh\lambda y+G^b\sinh\lambda y+H^b\cosh\lambda y\\
&\quad -k^2\frac{D\sigma^b}{\beta^2(\sigma_{0N}^b)^3(\lambda^2-q^2)(\lambda^2-k^2)}.
\end{aligned}\right\}$$

Superscripts a or b denote liquids a or b, respectively. A, B, C, D, E, F, G and H are constants. λ and q are positive and are given by

$$\left.\begin{aligned}
\lambda &= \sqrt{k^2+Pes},\\
q &= \sqrt{k^2+Res+\frac{3}{\beta^2}}.
\end{aligned}\right\}$$

Now we must use the boundary and interface conditions to solve for the constants in the solution.

As noted in the previous chapter, the linearized jump conditions for electrical conductivity at the interface are

$$\left.\begin{aligned} \|\sigma\| &= 0, \\ \|D\sigma\| &= Pev_{int}\sigma_{0N}. \end{aligned}\right\}$$

The linearized boundary conditions for electrical conductivity at the side walls (i.e. at $y = \pm 1$) are given by $D\sigma = 0$. The interface conditions together with the boundary conditions give the following solution for the constants

$$\left.\begin{aligned} A^a = -A^b &= -\frac{Pev_{\text{int}}\Delta\sigma_{0N}}{2\lambda}, \\ B^a = B^b &= -\frac{Pev_{\text{int}}\Delta\sigma_{0N}}{2\lambda\tanh\lambda}, \end{aligned}\right\}$$

where $\Delta\sigma_{0N} = \sigma^a_{0N} - \sigma^b_{0N}$, and $v_{\text{int}} = v^a_m = v^b_m = \dfrac{v^a_m + v^b_m}{2}$ at $y = 0$ is the y component of velocity at the interface.

The interface conditions for the electrical potential are

$$\left.\begin{aligned} &\|\phi\| = 0, \\ &\|\sigma_{0N} D\phi\| + \sigma_{y=0}\frac{\Delta\sigma_{0N}}{\sigma^+_{0N}\sigma^-_{0N}} \end{aligned}\right\} \text{ at y=0.}$$

Since there are electrodes at $y = \pm 1$, there is no perturbation of the electric potential at those boundaries. This implies $\phi = 0$ at $y = \pm 1$. Using these interface and boundary conditions we solve for C^a, C^b, D^a, and D^b to obtain

$$\left.\begin{aligned} C^a &= \frac{\Delta\sigma_{0N}}{4\sigma^a_{0N}\sigma^b_{0N}}\frac{k}{\lambda^2-k^2}\left(\frac{-1}{\tanh\lambda}\right)\frac{Pev_{\text{int}}\Delta\sigma_{0N}}{\lambda} + \frac{\text{Pe}v_{\text{int}}\Delta\sigma_{0N}\sigma^b_{0N}}{4(\lambda^2-k^2)\tanh k}\frac{\sigma^{a2}_{0N}+\sigma^{b2}_{0N}}{\sigma^{a2}_{0N}\sigma^{b2}_{0N}}, \\ C^b &= \frac{\Delta\sigma_{0N}}{4\sigma^a_{0N}\sigma^b_{0N}}\frac{k}{\lambda^2-k^2}\left(\frac{1}{\tanh\lambda}\right)\frac{Pev_{\text{int}}\Delta\sigma_{0N}}{\lambda} + \frac{\text{Pe}v_{\text{int}}\Delta\sigma_{0N}\sigma^a_{0N}}{4(\lambda^2-k^2)\tanh k}\frac{\sigma^{a2}_{0N}+\sigma^{b2}_{0N}}{\sigma^{a2}_{0N}\sigma^{b2}_{0N}}, \\ D^a &= -\tanh k C^a, \\ D^b &= \tanh k C^b. \end{aligned}\right\}$$

The interface conditions for velocity are $\|Dv_m\| = 0$ (which follows from $\|u_m\| = 0$) and $\|v_m\| = 0$ at $y = 0$. The velocity boundary conditions are $v_m = 0$ and $Dv_m = 0$ (i.e. $u_m = 0$) at $y = \pm 1$. The stress conditions at the interface are $\| - p + 2\beta^2 Dv - \dfrac{D\phi}{\sigma_{0N}}\| = 0$

and $\|D^2v + v - \frac{\phi}{\sigma_{0N}}\| = 0$. Using these conditions together with Equations (3.6) and (3.6) we get eight equations for the constants E, F, G and H in liquids a and b. Only four of those equations and the equation $v_{\text{int}} = \frac{v_m^a + v_m^b}{2}$ contribute to the dispersion equation for the maximum growth rate. These equations are given below in a matrix form

$$\begin{pmatrix} \sinh k & \cosh k & \sinh q & \cosh q & 0 \\ k\cosh k & k\sinh k & q\cosh q & q\sinh q & -\frac{k^2\lambda^2 P_\Sigma}{2\lambda\sinh\lambda(\lambda^2-q^2)(\lambda^2-k^2)} \\ q & 0 & q & 0 & -\frac{k^2\lambda^2 P_\Sigma}{2\lambda\tanh\lambda(\lambda^2-q^2)(\lambda^2-k^2)} \\ k^3 & 0 & q^3 & 0 & f(k,\lambda,q,\Gamma,P_\Sigma) \\ 0 & 1 & 0 & 1 & (\frac{k^2 P_\Sigma}{2(\lambda^2-k^2)(\lambda^2-q^2)-2}) \end{pmatrix} \begin{pmatrix} E^s \\ F^t \\ G^s \\ H^t \\ v_{\text{int}} \end{pmatrix}$$

(3.6)
$$= \begin{pmatrix} 0 \\ 0 \\ 0 \\ 0 \\ 0 \end{pmatrix}$$

In Equation (3.6), $E^s = E^a - E^b$ and $F^t = F^a + F^b$. G^s and H^t are defined similarly. $P_\Sigma = Pe\Sigma\Gamma/\beta^2$, where $\Sigma = \frac{\Delta\sigma_{0N}^2}{\sigma_{0N}^{a2}\sigma_{0N}^{b2}}$ and $\Gamma = \frac{\sigma_{0N}^a}{\sigma_{0N}^b} + \frac{\sigma_{0N}^b}{\sigma_{0N}^a} + 1$.

Setting the determinant of the matrix in equation (3.6) to zero gives the dispersion equation. All symbolic manipulations were done in Mathematica.

3.2. Results

The dispersion equation gives P_Σ as a function of $\lambda, k, q,$ and Γ.

$$\begin{aligned}
P_\Sigma = -(32\Gamma\lambda(-k^2+\lambda^2)q(k^2-q^2)(\lambda^2-q^2)(k\mathrm{cosh}q\mathrm{sinh}k - q\mathrm{cosh}k\mathrm{sinh}q)) \\
/(k^2(\frac{1}{2}(-1+\Gamma)k\lambda q(\lambda^2-q^2)\mathrm{coth}k(31+\mathrm{cosh}k^2 - 16\mathrm{cosh}k\mathrm{cosh}q + \mathrm{sinh}k^2) \\
+8\mathrm{coth}\lambda(q(-\Gamma\lambda^2q^2 + k^2((-2+\Gamma)\lambda^2+2q^2)) - q(-\Gamma\lambda^2q^2 + k^2((-2+\Gamma)\lambda^2+2q^2)) \\
\mathrm{cosh}k\mathrm{cosh}q + k(k^2((-1+\Gamma)\lambda^2+q^2) + q^2((-1+\Gamma)\lambda^2+q^2))\mathrm{sinh}k\mathrm{sinh}q) + \\
\lambda(-8q\mathrm{cosh}q(-(-1+\Gamma)k(\lambda^2-q^2)\mathrm{csch}k + \Gamma\lambda(k^2-q^2)\mathrm{csch}\lambda + k(\Gamma k^2 + \\
\lambda^2 - \Gamma\lambda^2 - q^2)\mathrm{sinh}k + \mathrm{cosh}k(8\Gamma\lambda q(k^2-q^2)\mathrm{csch}\lambda + (-1+\Gamma)kq(\lambda^2-q^2)\mathrm{sinh}k - \\
8(q^2((-1+\Gamma)\lambda^2+q^2) + k^2((-1+\Gamma)\lambda^2 + (1-2\Gamma)q^2))\mathrm{sinh}q)))).
\end{aligned}$$

(3.7)

P_Σ can also be expressed as a function of $k, \mathrm{Pes}, (\mathrm{Res} + \dfrac{3}{\beta^2}),$ and Γ i.e.

$$P_\Sigma = f(\lambda, k, q, \Gamma) = g(k, \mathrm{Pes}, (\mathrm{Res} + \frac{3}{\beta^2}), \Gamma). \tag{3.8}$$

For marginal stability at low Re we take $Re \to 0$ and $s \to 0$. In this case P_Σ depends on $\Gamma, k,$ and β i.e.

$$P_\Sigma = f(\Gamma, k, \beta). \tag{3.9}$$

The trends of P_Σ will be considered next. Although there are no systematic data available for the onset of instability for the perpendicular case, we will first use parameters corresponding to typical experimental values [**35**]. To that end, we will use $d = 5.5\mu m$, $H = 78\mu m$, $\rho = 1000kg/m^3$, $\mu = 0.001kg/ms$, $\varepsilon = 6.9 \times 10^{-10}C/Vm$, $D_\sigma = 10^{-9}m^2/s$, and $\dfrac{\sigma_0^a}{\sigma_0^b} = 10$. This implies $\beta = 0.07$, $\Gamma = 11.1$, and $\Sigma = 24.5$. The only free variables are I_0/σ_m and k. In this case, P_Σ is therefore the non-dimensional parameter that represents the variation of I_0/σ_m which is an average measure of the external electric field.

Figure (3.2) shows the marginal stability curve of P_Σ vs.the wavenumber k obtained from the dispersion equation discussed above. It is seen that there is a critical value of the P_Σ (or correspondingly I_0/σ_m) below which the system is stable. This is consistent with the threshold type behavior seen in experiments [**6**]. Figure (3.2) shows that the system becomes unstable at $P_\Sigma^{crit} = 40211.4$. This implies a critical value of $(I_0/\sigma_m)^{crit} = 0.06kV/cm$. Typical values in experiments are $0.1 - 1kV/cm$ [**6, 35**]. This suggests that an instability should be observed under experimental conditions and the limited data available [**6**] are consistent with these calculations.

Figure (3.2) also shows that at $P_\Sigma^{crit} = 40211.4$ the unstable wave corresponds to $k = 13.6$ which implies a wavelength of the instability that is 0.23 times the channel width. Typical wavelengths of the instability are reported to be of the order of the device width [**6**].

The critical value for the onset of instability P_Σ^{crit} identified in Figure (3.2) depends on the the conductivity ratio of the two liquids (i.e. on Γ) and also on the channel height to width ratio (i.e. on β). This is considered next.

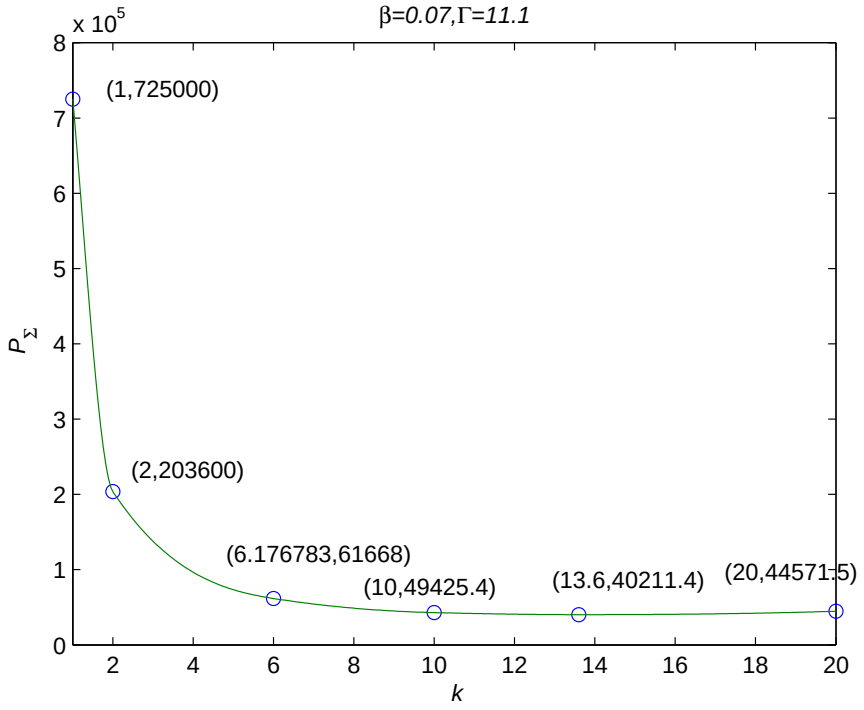

Figure 3.2. The marginal stability curve of P_Σ vs. k for β=0.07 and Γ=11.1.

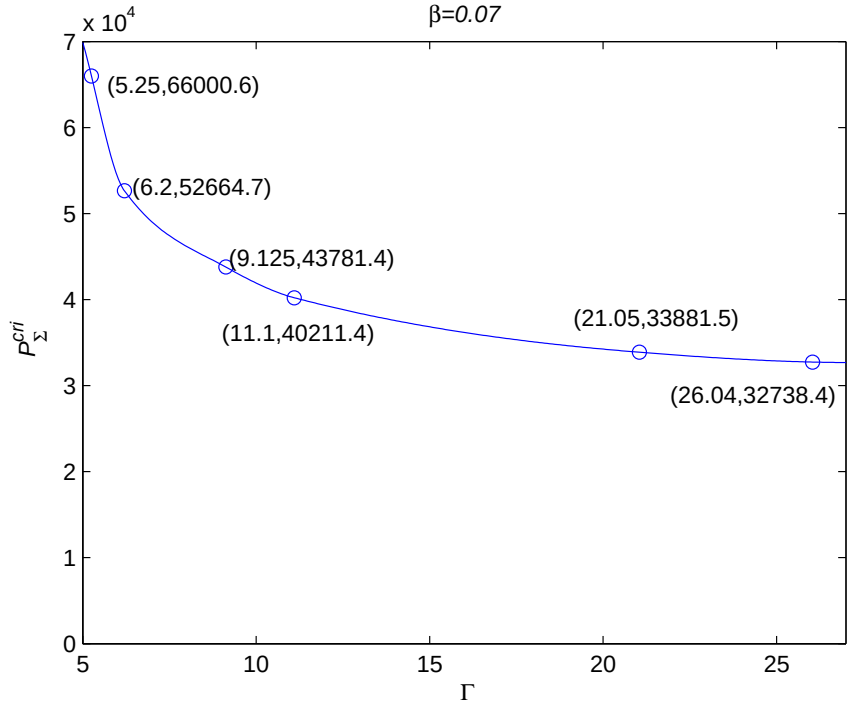

Figure 3.3. Plot of P_{Σ}^{cri} vs. Γ indicating the critical condition for the onset of instability at β=0.07.

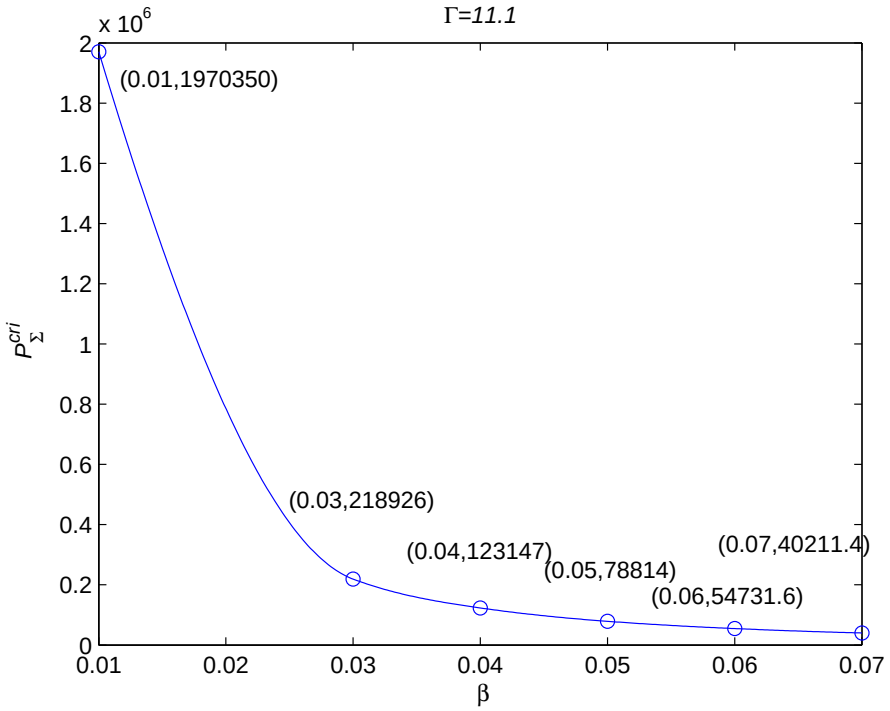

Figure 3.4. Plot of P_{Σ}^{cri} vs. β indicating the critical condition for the onset of instability at Γ=11.1.

Figure (3.3) shows P_{Σ}^{cri} vs. Γ indicating the critical condition for the onset of instability at $\beta = 0.07$. As expected, when Γ increases the critical value of P_{Σ} decreases. It implies that the system is more unstable with a larger conductivity ratio between the two liquids.

Figure (3.4) shows P_{Σ}^{cri} vs. β indicating the critical condition for the onset of instability at $\Gamma = 11.1$. As β decreases, i.e. as the channel becomes more shallow, the critical value of P_{Σ} increases. It implies that the shallow nature of the channel has a stabilizing effect on the instability. Thus, it would be a better device design for applications such as Field Amplified Sample Stacking (FASS) where it is desirable to avoid electrokinetic instabilities. Our approach can provide a formal theoretical estimate for the desired aspect ratio of the channel.

Finally, we compare the cases where the electric field is applied parallel or perpendicular to the liquid-liquid interface. Using the same parameters as those used in Figure (3.2), it was found that the critical electric field for the onset of instability for the parallel electric field case is $0.08kV/cm$ [**37**]. Comparing this with the value of $0.06kV/cm$ computed above for the perpendicular electric field case, it is implied that the perpendicular electric field case is more unstable. Although we have compared these numbers at the experimentally relevant condition, this trend continues at other parameters.

The reason for greater instability of the perpendicular electric field case is same as that discussed in the previous chapter.

3.3. Conclusion

In this chapter the instability at the interface between two miscible liquids with identical mechanical properties but different electrical conductivities was analyzed at experimentally relevant conditions. Specifically, the effect of the microchannel geometry was studied for the perpendicular electric field case.

Our linear stability analysis based on a sharp interface approach, once again, enabled us to identify the appropriate parameters to characterize the instability. The relevant parameters are P_{Σ}, β, and Γ as defined in the chapter.

The analysis captured the threshold type behavior for the onset of instability. It showed that larger conductivity ratio has a destabilizing effect, while the shallow nature of the channel has a stabilizing effect on the instability. Although these trends are not surprising, our approach provides a quantitative tool to estimate these effects. Finally, our approach successfully captures the experimental observation that the perpendicular electric field case is more unstable.

CHAPTER 4

Numerical simulation of electrohydrodynamic particulate flows

4.1. Introduction

Electrohydrodynamic self-assembly of particles is an important tool in micro- and nano-scale fabrication process. For example, carbon nanotubes (CNTs) can be used in nanoscale electronic devices because of their unique electrical and mechanical properties[**13, 14**]. J. Lee and co-workers have reported deposition of CNTs between two electrodes using a combination of AC and DC electric fields [**1**] (also see Figures 1.2 and 1.3).

The process of electrohydrodynamic self-assembly can be based on electrophoretic and/or dielectrophoretic forces. Charged particles experience a force due to an external electric field. This is the electrophoretic force. Dielectrophoresis (DEP), which was a term coined by Pohl [**42**], is the motion of uncharged polarizied particles in a *non-uniform* electric field.

DEP based deposition process leads to many interesting observations. For example, Figures (1.2) and (1.3) show that the deposition pattern of multiwalled carbon nanotubes (MWCNTs), between electrodes, is strongly dependent on the ratio of the DC and AC electric fields. A fundamental understanding of such phenomena is still missing.

In this chapter the objective is to formulate and complete an initial implementation of a fundamental numerical tool capable of investigating electrohydrodynamic particulate flows. Such a tool, which is not currently available in literature, would eventually be useful in developing better strategies for electrohydrodynamic self-assembly. Studying the self-assembly process itself is not the focus of this work. It is also noted that after the initial development, this approach was further developed in collaboration with Prof. W.-K. Liu's group [**43, 44**]. Detailed quantitative tests of this approach can be found elsewhere [**44**].

The chapter is organized as follows. In section (4.2) we will review the dipole moment theory for dielectrophoresis, which is based on approximations. In section (4.3) our numerical approach will be presented, and results will be presented in section (4.4).

4.2. Background: The dipole moment theory

In this section the dipole moment theory for DEP, which is based on approximations, is summarized. Dipole moment theory is not accurate for arbitrarily shaped bodies or when the particle size is not small compared to the external length scale imposed by the geometry, or when there are multiple particles that are electrohydrodynamically interacting.

4.2.1. DEP force: DC field

Figure (4.1) shows a dielectric particle of radius R and permittivity ε_2 immersed in a dielectric fluid of infinite extent and of permittivity ε_1. The particle and the fluid are subjected to a uniform electric field of magnitude E_0 as shown. Note that $\mathbf{E}_0 = E_0\hat{\mathbf{z}}$, where bold variables are vectors and $\hat{\mathbf{z}}$ is the unit vector in the z-direction.

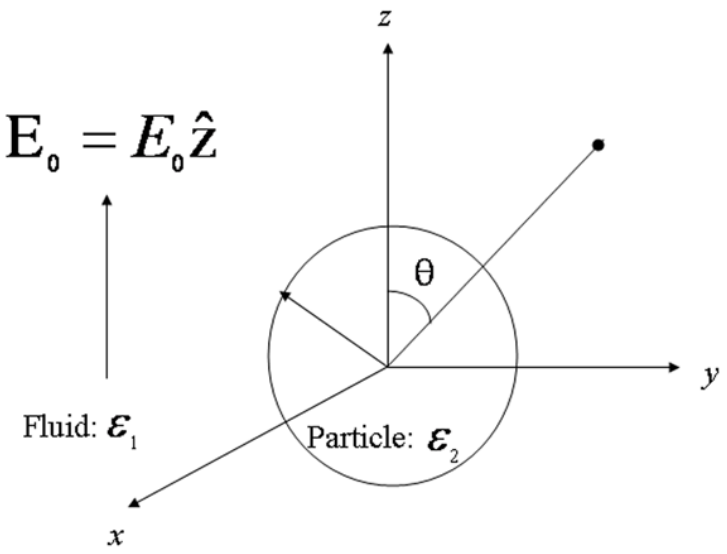

Figure 4.1. A dielectric sphere of radius R and permittivity ε_2 immersed in a dielectric liquid of permittivity ε_1 and subjected to a uniform electric field of magnitude E_0 [**45**].

The analytic solution for this problem is [**45**]:

$$\phi(r,\theta) = -E_0 r\cos\theta + \frac{A\cos\theta}{r^2}, \quad r > R, \tag{4.1}$$

$$\phi(r,\theta) = -Br\cos\theta, \quad r < R, \tag{4.2}$$

where ϕ is the electric potential, θ and r are the polar angle and the radial position in a spherical coordinate system (see Figure 4.1), and

$$A = \frac{\varepsilon_2 - \varepsilon_1}{\varepsilon_2 + 2\varepsilon_1} R^3 E_0, \tag{4.3}$$

$$B = \frac{3\varepsilon_1}{\varepsilon_2 + 2\varepsilon_1} E_0. \tag{4.4}$$

Note that the potential field ϕ_{dipole} of a point dipole of dipole moment p_{eff} directed in the z-direction is [**45**]

$$\phi_{dipole} = \frac{p_{eff} cos\theta}{4\pi\varepsilon_1 r^2}. \tag{4.5}$$

Comparing the far field solution in Equation (4.1) with the potential field due to a point dipole in Equation (4.5), it can be deduced that the effective dipole moment p_{eff} induced due to the presence of the particle is

$$\mathbf{p}_{eff} = p_{eff}\hat{\mathbf{z}} = 4\pi\varepsilon_1 K R^3 E_0 \hat{\mathbf{z}}, \tag{4.6}$$

where K is known as the Clausius-Mossotti factor is given by

$$K(\varepsilon_1, \varepsilon_2) = \frac{\varepsilon_2 - \varepsilon_1}{\varepsilon_2 + 2\varepsilon_1}. \tag{4.7}$$

Thus, the effect of the presence of the particle in an external electric field can be approximated in terms of an induced dipole of strength given in Equation (4.6). The electric field due to this induced dipole is a good approximation to the exact solution in Equation (4.1) in the farfield.

If the external electric field has a gradient, then the interaction of the induced dipole with the gradient of electric field gives a net force on the particle. This is the DEP force

[**45**]. If the length scale at which the external electric field varies is much larger than the particle size, then the DEP force can be approximated by the dot product of the induced dipole moment and the gradient of the electric field [**45**]. In the case depicted in Figure (4.1) it implies that

$$\mathbf{F}_{DEP} = \mathbf{p}_{eff} \cdot \nabla \mathbf{E}_0 = 2\pi\varepsilon_1 R^3 K \nabla(\mathbf{E}_0 \cdot \mathbf{E}_0) = 2\pi\varepsilon_1 R^3 K \nabla E_0^2, \tag{4.8}$$

where $\mathbf{E}_0$ is the external electric field in the absence of the particle and the gradient of this unperturbed electric field is computed at the location of the center of the spherical particle. Equation (4.8) gives the DEP force due to a DC field when both the particle and the fluid are perfect dielectrics (i.e. perfect insulators).

Equation (4.8) implies that the DEP force is in the direction of increasing magnitude of the external electric field if $\varepsilon_2 > \varepsilon_1$. This is called positive DEP. In this case the particle migrates toward the location where the external electric field is high. When $\varepsilon_2 < \varepsilon_1$ the DEP force is in the direction of decreasing magnitude of the external electric field. This is called negative DEP and the particle migrates toward the location where the external electric field is low.

4.2.2. DEP force: AC field

In the presence of an AC field, analysis similar to that discussed above leads to the following expression for the DEP force on a sphere [**45, 46**]

$$\langle \mathbf{F}_{DEP} \rangle = 2\pi\varepsilon_1 R^3 Re[\underline{K}(\omega)] \nabla E_{0,rms}^2, \tag{4.9}$$

where $\langle\rangle$ denotes time-averaged value, Re denotes real value of the term inside the bracket, subscript rms denotes the root mean square value of the external AC field of magnitude E_0 in the z-direction, and a bar under a variable denotes a complex variable, e.g., $\underline{K}(\omega)$ is the complex Clausius-Mossotti factor given by

$$\underline{K} = \frac{\varepsilon_2 - \varepsilon_1 - i(\sigma_2 - \sigma_1)/\omega}{\varepsilon_2 + 2\varepsilon_1 - i(\sigma_2 + 2\sigma_1)/\omega}. \tag{4.10}$$

In the above equation σ_1 and σ_2 are the electrical conductivities of the fluid and the particle, respectively, and $i = \sqrt{-1}$. Note that in this case a lossy dielectric is considered, i.e., it is not a perfect insulator. Therefore, the electrical conductivities are non-zero. $Re[\underline{K}(\omega)]$ required to calculate the DEP force is given by

$$Re[\underline{K}] = \frac{\varepsilon_2 - \varepsilon_1}{\varepsilon_2 + 2\varepsilon_1} + \frac{3(\varepsilon_1\sigma_2 - \varepsilon_2\sigma_1)}{\tau_{MW}(\sigma_2 + 2\sigma_1)^2(1 + \omega^2\tau_{MW})^2}, \tag{4.11}$$

where τ_{MW} is the Maxwell-Wagner charge relaxation time which is defined as

$$\tau_{MW} = \frac{\varepsilon_2 + \varepsilon_1}{\sigma_2 + 2\sigma_1}. \tag{4.12}$$

The high and low frequency limits of $Re[\underline{K}]$ can be identified as follows

$$Re[\underline{K}] = \begin{cases} \dfrac{\sigma_2 - \sigma_1}{\sigma_2 + 2\sigma_1} & \omega\tau_{MW} << 1, \\ \dfrac{\varepsilon_2 - \varepsilon_1}{\varepsilon_2 + 2\varepsilon_1} & \omega\tau_{MW} >> 1. \end{cases} \tag{4.13}$$

Thus, DC conduction governs the low-frequency DEP behavior, and dielectric polarization governs the high-frequency behavior.

Finally, it is noted that positive(negative) DEP will be observed when the sign of $Re[\underline{K}(\omega)]$ is positive(negative). This sign will depend not only on the material parameters, i.e., the permittivities and the conductivities, but also on the imposed frequency ω.

The above results will be used to qualitatively validate our numerical method.

4.3. Numerical formulation

The numerical formulation is presented in this section. The solution process has two primary steps. In the first step, the AC or DC electric field is solved for a given configuration of the particles. Once the electric field is obtained, the electrical force at any location is obtained based on the Maxwell stress. In the second step the fluid-particle problem is solved together with the electrical force computed in step one. The fluid-particle solution gives the velocity field of the fluid as well as the translational and rotational velocities of the particles. The particle positions are updated and same steps are repeated to calculate a solution for

the next time step. The sections below are organized consistent with the above two step process.

4.3.1. Governing equations for the electric field

The governing equations for the electric field are presented below for a general case of an AC field. The equations for the DC case follow as a special case with zero frequency.

The electric field $\underline{\mathbf{E}}$ is the gradient of a scalar potential $\underline{\phi}$

$$\underline{\mathbf{E}} = -\nabla\underline{\phi}. \tag{4.14}$$

In the equation above and in those to follow, bold variables are vectors or tensors, and the underbar denotes a complex variable. Since we consider an AC field, in general, it is convenient to consider the electric field and its potential as complex variables. The electric field obeys the following equation at any point in the domain:

$$\nabla \cdot (\varepsilon\nabla\underline{\phi}) = -\underline{\rho_b}, \tag{4.15}$$

where ε is the permittivity which is a function of location (i.e. it depends on whether a given location is in the fluid or the particle). The conservation of bulk charge ρ_b is given by

$$\frac{D\underline{\rho_b}}{Dt} - \nabla \cdot (\sigma\nabla\underline{\phi}) = 0, \tag{4.16}$$

where σ is the electrical conductivity which is also a function of location. In an AC field we write

$$\left.\begin{aligned} \underline{\rho_b} &= \underline{\hat{\rho}_b} e^{i\omega t}, \\ \underline{\phi} &= \underline{\hat{\phi}} e^{i\omega t}, \end{aligned}\right\}$$

where ω is the angular frequency, and variables with hat are the amplitudes (which can be complex numbers). Inserting Equation (4.17) into Equation (4.16), and assuming that the contribution from the convection term in Equation (4.16) is negligible, this is reasonable for

low Reynolds number flows, we get

$$i\omega \underline{\hat{\rho}}_b e^{i\omega t} = \nabla \cdot (\sigma \nabla \underline{\hat{\phi}}) e^{i\omega t}. \tag{4.17}$$

Eliminating $e^{i\omega t}$ from both sides of Equation (4.17) we get,

$$\underline{\hat{\rho}}_b = -\nabla \cdot (\frac{i\sigma}{\omega} \nabla \underline{\hat{\phi}}). \tag{4.18}$$

Using this in Equation (4.15), we get

$$\begin{aligned} \nabla \cdot (\varepsilon \nabla \underline{\hat{\phi}}) &= \nabla \cdot (\frac{i\sigma}{\omega} \nabla \underline{\hat{\phi}}), \\ \Rightarrow \nabla \cdot ((\varepsilon - \frac{i\sigma}{\omega}) \nabla \underline{\hat{\phi}}) &= 0. \end{aligned} \tag{4.19}$$

By defining complex permittivity as

$$\underline{\varepsilon} = \varepsilon + \frac{\sigma}{i\omega}. \tag{4.20}$$

Equation (4.19) can be rewritten as

$$\nabla \cdot (\underline{\varepsilon} \nabla \underline{\hat{\phi}}) = 0. \tag{4.21}$$

This is simply a Laplace equation with complex variables. This equation together with the boundary condition for $\hat{\phi}$ can be discretized and solved for the complex amplitude of the electrical potential in the entire domain for the given position of the particle (note that multiple particles case is no different). The complex permittivity $\underline{\varepsilon}$ is different in the particle and fluid domains. Thus, Equation (4.21) represents a combined fluid-particle equation for the entire domain.

Once the electric field is obtained by solving Equation (4.21), it can be used to calculate the electrical force in the domain. This is discussed next.

4.3.2. Electrical force

The electrical force is calculated based on the Maxwell stress $\boldsymbol{\sigma}_M$ [**40, 46**]. The procedure is discussed below.

The Maxwell stress $\boldsymbol{\sigma}_M$ is given by [**40**]

$$\boldsymbol{\sigma}_M = \varepsilon \mathbf{E}\,\mathbf{E} - \frac{\varepsilon}{2}(\mathbf{E}\cdot\mathbf{E})\mathbf{I}, \tag{4.22}$$

where $\mathbf{I}$ is the identity tensor. The divergence of the Maxwell stress is the electrical body force at any location in the domain. It is given by

$$\nabla\cdot\boldsymbol{\sigma}_M = \nabla\cdot(\varepsilon\mathbf{E})\mathbf{E} - \frac{1}{2}\nabla\varepsilon(\mathbf{E}\cdot\mathbf{E}). \tag{4.23}$$

In case of AC fields, the Maxwell stress $\boldsymbol{\sigma}_M$ is given by

$$\boldsymbol{\sigma}_M = \varepsilon Re(\underline{\mathbf{E}})Re(\underline{\mathbf{E}}) - \frac{\varepsilon}{2}Re(\underline{\mathbf{E}})\cdot Re(\underline{\mathbf{E}})\mathbf{I}, \tag{4.24}$$

where $\underline{\mathbf{E}} = \hat{\underline{\mathbf{E}}}e^{i\omega t}$. The real part of $\underline{\mathbf{E}}$ can be expressed as:

$$Re(\underline{\mathbf{E}}) = \frac{1}{2}(\underline{\mathbf{E}} + \underline{\mathbf{E}}^*), \tag{4.25}$$

where superscript * indicates the complex conjugate. Rewriting the Maxwell stress we get:

$$\boldsymbol{\sigma}_M = \underbrace{\varepsilon\frac{1}{2}(\underline{\mathbf{E}} + \underline{\mathbf{E}}^*)\frac{1}{2}(\underline{\mathbf{E}} + \underline{\mathbf{E}}^*)}_{(1)} - \underbrace{\frac{\varepsilon}{8}(\underline{\mathbf{E}} + \underline{\mathbf{E}}^*)\cdot(\underline{\mathbf{E}} + \underline{\mathbf{E}}^*)\mathbf{I}}_{(2)}. \tag{4.26}$$

If the frequency time scale is much shorter (i.e. at high frequencies) than the particle response time scale, then only the time averaged electrical body force is of interest. To that end, the time averaged Maxwell stress is calculated by averaging over the time period T of

the imposed frequency. This done below.

$$\begin{aligned}
&\frac{1}{T}\int_0^T \boldsymbol{\sigma}_{M,1} dt \\
&= \frac{1}{T}\int_0^T \frac{\varepsilon}{4}(\underline{\mathbf{E}}\,\underline{\mathbf{E}} + \underline{\mathbf{E}}\,\underline{\mathbf{E}}^* + \underline{\mathbf{E}}^*\underline{\mathbf{E}} + \underline{\mathbf{E}}^*\underline{\mathbf{E}}^*) dt \\
&= \frac{1}{T}\int_0^T \frac{\varepsilon}{4}(\underline{\hat{\mathbf{E}}}\underline{\hat{\mathbf{E}}} e^{2i\omega t} + \underline{\hat{\mathbf{E}}} e^{i\omega t}\underline{\hat{\mathbf{E}}}^* e^{-i\omega t} + \underline{\hat{\mathbf{E}}}^* e^{-i\omega t}\underline{\hat{\mathbf{E}}} e^{i\omega t} + \underline{\hat{\mathbf{E}}}^*\underline{\hat{\mathbf{E}}}^* e^{-2i\omega t}) dt \\
&= \frac{1}{T}\int_0^T \frac{\varepsilon}{4}(\underline{\hat{\mathbf{E}}}\underline{\hat{\mathbf{E}}}^* + \underline{\hat{\mathbf{E}}}^*\underline{\hat{\mathbf{E}}}) dt \\
&= \frac{\varepsilon}{4}(\underline{\hat{\mathbf{E}}}\underline{\hat{\mathbf{E}}}^* + \underline{\hat{\mathbf{E}}}^*\underline{\hat{\mathbf{E}}}),
\end{aligned}$$

where $\boldsymbol{\sigma}_{M,1}$ corresponds to the terms identified as (1) in equation (4.26). Similarly, we get

$$\begin{aligned}
&\frac{1}{T}\int_0^T \boldsymbol{\sigma}_{M,2} dt \\
&= \frac{1}{T}\int_0^T \frac{-\varepsilon}{8}(\underline{\mathbf{E}} \cdot \underline{\mathbf{E}} + \underline{\mathbf{E}} \cdot \underline{\mathbf{E}}^* + \underline{\mathbf{E}}^* \cdot \underline{\mathbf{E}} + \underline{\mathbf{E}}^* \cdot \underline{\mathbf{E}}^*)\mathbf{I} dt \\
&= \frac{1}{T}\int_0^T \frac{-\varepsilon}{8}(\underline{\hat{\mathbf{E}}} \cdot \underline{\hat{\mathbf{E}}} e^{2i\omega t} + \underline{\hat{\mathbf{E}}} e^{i\omega t} \cdot \underline{\hat{\mathbf{E}}}^* e^{-i\omega t} + \underline{\hat{\mathbf{E}}}^* e^{-i\omega t} \cdot \underline{\hat{\mathbf{E}}} e^{i\omega t} + \underline{\hat{\mathbf{E}}}^* \cdot \underline{\hat{\mathbf{E}}}^* e^{-2i\omega t})\mathbf{I} dt \\
&= \frac{1}{T}\int_0^T \frac{-\varepsilon}{8}(\underline{\hat{\mathbf{E}}} \cdot \underline{\hat{\mathbf{E}}}^* + \underline{\hat{\mathbf{E}}}^* \cdot \underline{\hat{\mathbf{E}}})\mathbf{I} dt \\
&= -\frac{\varepsilon}{4}|\underline{\hat{\mathbf{E}}}|^2\mathbf{I},
\end{aligned}$$

where $\boldsymbol{\sigma}_{M,2}$ corresponds to the terms identified as (2) in Equation (4.26). Substituting Equations (4.27)and (4.27) into Equation (4.26), the time averaged Maxwell stress $\langle \boldsymbol{\sigma}_M \rangle$ is given by:

$$\langle \boldsymbol{\sigma}_M \rangle = \frac{\varepsilon}{4}(\underline{\hat{\mathbf{E}}}\,\underline{\hat{\mathbf{E}}}^* + \underline{\hat{\mathbf{E}}}^*\underline{\hat{\mathbf{E}}} - |\underline{\hat{\mathbf{E}}}|^2\mathbf{I}). \tag{4.27}$$

The electrical body force sought at a point is the divergence of the time averaged Maxwell stress, i.e. $\nabla \cdot \langle \boldsymbol{\sigma}_M \rangle$. It is given by

$$\nabla \cdot \langle \boldsymbol{\sigma}_M \rangle = \frac{1}{4}([\nabla \cdot (\varepsilon\underline{\hat{\mathbf{E}}})]\underline{\hat{\mathbf{E}}}^* + [\nabla \cdot (\varepsilon\underline{\hat{\mathbf{E}}}^*)]\underline{\hat{\mathbf{E}}} - \nabla\varepsilon|\underline{\hat{\mathbf{E}}}|^2). \tag{4.28}$$

This body force term will be used in the fluid-particle equations of motion. Adding this body force in the particle domain gives the net electrical force on the particle which includes the DEP force.

The time averaged body force will be used under the assumption that the frequency is high such that the particle response time scale is much larger than the frequency time scale. Thus, the fluid-particle motion will be determined in response to the time averaged electrical force. The governing equations for fluid-particle motion are considered next.

4.3.3. Governing equations for fluid-particle motion

Consider a simple case with one spherical particle in the fluid. Extension to multiple particles is straightforward. The entire computational domain which includes both the fluid and the particle is denoted by Ω. P(t) is the particle domain that changes with time, and ∂P is the interface between the particle and the fluid. Γ is the fluid boundary which is not shared with the particle. The combined equations for the fluid-particle domain are:

$$\rho(\frac{\partial \mathbf{u}}{\partial t} + (\mathbf{u}\cdot\nabla)\mathbf{u}) = -\nabla p + \mu\nabla^2\mathbf{u} + \rho\mathbf{g} + \mathbf{f} + \nabla\cdot\langle\boldsymbol{\sigma}_M\rangle \qquad \text{in } \Omega, \tag{4.29}$$

$$\nabla\cdot\mathbf{u} = 0 \qquad \text{in } \Omega, \tag{4.30}$$

$$\nabla\cdot(\mathbf{D}[\mathbf{u}]) = 0 \qquad \text{in P(t)}, \tag{4.31}$$

$$\mathbf{D}[\mathbf{u}]\cdot\mathbf{n} = 0 \qquad \text{on } \partial\text{P(t)}, \tag{4.32}$$

$$\mathbf{u} = \mathbf{u}_\Gamma(t) \qquad \text{on } \Gamma, \tag{4.33}$$

where $\mathbf{u}$ is the fluid velocity, p is the pressure, μ is the fluid viscosity, ρ is the density $= \rho_f$ in the fluid and $= \rho_s$ in the particle, and $\mathbf{g}$ is the gravitational acceleration. $\mathbf{f}$ is non-zero only in the particle domain and arises as a result of the rigid motion constraint in the particle domain represented by Equations (4.31) and (4.32), where $\mathbf{n}$ is a unit normal on the particle surface and $\mathbf{D}[\mathbf{u}]$ is the deformation-rate tensor [**47**]. In this formulation the particle is treated as if it is a fluid with an additional rigid motion constraint. The fluid-particle system is driven by the electrical body force $\nabla\cdot\langle\boldsymbol{\sigma}_M\rangle$.

The fluid-particle equations of motion are solved by an algorithm developed by Sharma and Patankar [**48, 49**]. That algorithm is summarized next for completeness.

4.3.4. Computational algorithm

Numerical simulation techniques for solid-fluid flows have been developed for the past decade. These techniques are called Direct Numerical Simulations (DNS). The Navier-Stokes equations governing the motion of the fluid are solved coupled with the rigid- body motion of the particles. The numerical algorithm we used here has been developed by Hu and co-workers [**50, 51, 52**]. The equivalence of the computational algorithm presented below to the governing equations of fluid-particle motion presented above will not be discussed here and can be found elsewhere [**48, 49**].

The governing equations are solved by a fractional time stepping approach analogous to that proposed by Kim and Moin [**53**]. Given the velocity field of the fluid and the translational and rotational velocities, $\mathbf{U}$ and $\boldsymbol{\omega}$, respectively, of the particle up to time instant t^n, the algorithm solves for the solution at a new time t^{n+1}. The steps are given as follow:

(1) Update the position of the particle based on the latest known translational and rotational velocities. This gives the new configuration of the domain. Solve for the electrical potential (Equation 4.21) and calculate the electrical body force (Equation 4.23 for DC or Equation 4.28 for AC) for this new configuration.

(2) Solve for $\hat{\mathbf{u}}$ satisfying the following equation in Ω

$$\begin{aligned} &\rho_f\left(\frac{\hat{\mathbf{u}}-\mathbf{u}^n}{\Delta t}\right)+\frac{\rho_f}{2}[3\nabla\cdot(\mathbf{u}^n\mathbf{u}^n)-\nabla\cdot(\mathbf{u}^{n-1}\mathbf{u}^{n-1})] \\ &+H^{n+1}(\rho_s-\rho_f)\left[\frac{(\mathbf{U}^n+\boldsymbol{\omega}^n\times\mathbf{r})-(\mathbf{U}^{n-1}+\boldsymbol{\omega}^{n-1}\times\mathbf{r})}{\triangle t}\right] \\ &=\frac{\mu}{2}\nabla^2(\hat{\mathbf{u}}+\mathbf{u}^n)+H^{n+1}(\rho_s-\rho_f)\mathbf{g}+\mathbf{f}^n+\nabla\cdot\langle\boldsymbol{\sigma}_M\rangle^{n+1}, \end{aligned} \tag{4.34}$$

where superscript denotes time instant, $\mathbf{r}$ is the coordinate with respect to the particle centroid, and H is a heaviside function defined by:

$$H(\mathbf{x})=\begin{cases} 1 & \mathbf{x}\in P, \\ 0 & \mathbf{x}\in\Omega\setminus P. \end{cases} \tag{4.35}$$

For the convective term a second-order explicit Adams-Bashforth scheme is used. A second order Crank-Nicholson scheme is used for the viscous term.

(3) Correct the velocity field $\hat{\mathbf{u}}$ to get the corrected velocity field $\hat{\hat{\mathbf{u}}}$ which satisfies the continuity equation $\nabla \cdot \hat{\hat{\mathbf{u}}} = 0$ in Ω. This is done by the following steps:

(a) Solve for a scalar field ψ such that

$$\rho_f(\frac{\hat{\hat{\mathbf{u}}} - \hat{\mathbf{u}}}{\triangle t}) = -\nabla\psi. \tag{4.36}$$

By imposing the incompressibility constraint $\nabla \cdot \hat{\hat{\mathbf{u}}} = 0$, we get the equation for ψ:

$$\nabla^2\psi - \frac{\rho_f}{\Delta t}\nabla \cdot \hat{\mathbf{u}} = 0. \tag{4.37}$$

(b) Compute $\hat{\hat{\mathbf{u}}}$ after solving for ψ

$$\hat{\hat{\mathbf{u}}} = -\frac{\Delta t}{\rho_f}(\nabla\psi) + \hat{\mathbf{u}}. \tag{4.38}$$

(c) Set $\mathbf{u}^{n+1} = \hat{\hat{\mathbf{u}}}$ in the fluid domain $\Omega/P(t)$, and calculate the pressure p^{n+1} as follows:

$$p^{n+1} = \psi + \frac{\Delta t\mu}{2\rho_f}\nabla^2\psi. \tag{4.39}$$

ψ is related to the original pressure p[**53**]

(4) Correct the velocity field $\hat{\hat{\mathbf{u}}}$ in the particle domain $P(t)$.

(a) Solve for $\hat{\hat{\hat{\mathbf{u}}}}$ satisfying the following equation:

$$\rho_f(\frac{\hat{\hat{\hat{\mathbf{u}}}} - \hat{\hat{\mathbf{u}}}}{\Delta t}) - H^{n+1}(\rho_s - \rho_f)[\frac{(\mathbf{U}^n + \boldsymbol{\omega}^n \times \mathbf{r}) - (\mathbf{U}^{n-1} + \boldsymbol{\omega}^{n-1} \times \mathbf{r})}{\Delta t}] = -\frac{\mathbf{f}^n}{2}. \tag{4.40}$$

(b) Do rigid body projection and acceleration correction:

$$\rho_f(\frac{\mathbf{u}^{n+1} - \hat{\hat{\hat{\mathbf{u}}}}}{\Delta t}) + H^{n+1}(\rho_s - \rho_f)[\frac{(\mathbf{U}^{n+1} + \boldsymbol{\omega}^{n+1} \times \mathbf{r}) - (\mathbf{U}^n + \boldsymbol{\omega}^n \times \mathbf{r})}{\Delta t}] = \frac{\mathbf{f}^{n+1}}{2}, \tag{4.41}$$

$$\Rightarrow [H^{n+1}\rho_s + (1-H^{n+1})\rho_f]\mathbf{u}^{n+1} = \rho_f \hat{\hat{\mathbf{u}}} + H^{n+1}(\rho_s - \rho_f)(\mathbf{U}^n + \boldsymbol{\omega}^n \times \mathbf{r}) + \frac{\mathbf{f}^{n+1}}{2}\Delta t. \tag{4.42}$$

To solve for $\mathbf{u}^{n+1}$, we need to know $\mathbf{f}^{n+1}$. We can get $\mathbf{f}^{n+1}$ by projecting $\hat{\hat{\mathbf{u}}}$ onto a rigid body motion in the particle domain. To that end, split $\hat{\hat{\mathbf{u}}}$ as given below

$$\hat{\hat{\mathbf{u}}} = (\hat{\hat{\mathbf{U}}} + \hat{\hat{\boldsymbol{\omega}}} \times \mathbf{r}) + \hat{\hat{\mathbf{u}}}', \tag{4.43}$$

where

$$M\hat{\hat{\mathbf{U}}} = \int_p \rho_s \hat{\hat{\mathbf{u}}} dx, \tag{4.44}$$

$$\mathbf{I}_p \cdot \hat{\hat{\boldsymbol{\omega}}} = \int_p \mathbf{r} \times \rho_s \hat{\hat{\mathbf{u}}} dx. \tag{4.45}$$

M is the mass of the particle and $\mathbf{I}_p$ is the moment of inertia of the particle. It can be shown that [**48, 49**]

$$\mathbf{f}^{n+1} = -\frac{2\rho_f \hat{\hat{\mathbf{u}}}'}{\Delta t}. \tag{4.46}$$

Equation (4.41) can now be used to solve for $\mathbf{u}^{n+1}$ in the particle domain.

Finally, it is noted that adding Equations (4.34), (4.36), (4.40), and (4.41) gives the time discretized momentum equation of the combined fluid-particle motion. The 3D spatial discretization is done by using second-order central differencing scheme. A control volume method is used, and all the elliptic equations are solved by using Fast Fourier Transform (FFT) solvers. A fixed staggered[**54**] grid is used in the entire domain. An immersed body approach is used to implement the rigid motion constraint [**47, 48, 49**].

4.4. Results

In this section we will first present results pertaining to the electric field solution. That will be followed by problems pertaining to a particle moving due to an electrical force in DC and AC fields. All simulations are done in 3D domains.

Note that in all the computations reported here we have chosen values for parameters to test the code and not necessarily to solve a specific physical situation. Hence, it is implied that all the parameters are non-dimensional with some appropriate scale and therefore we will not provide physical units in our discussion below.

4.4.1. Computation of the electric field and the electrical force

As an example of the computation of the electric field, here we consider a problem with a DC field. The computational domain is a cubic box of length $L = 1$ filled with fluid and one spherical particle is placed in the center of the box. The grid size is $\Delta x = \Delta y = \Delta z = 0.025$. Using the governing Equation (4.21), we solve for the electric potential ϕ. The boundary conditions used here are (see Figure 4.2)

$$\begin{cases} \phi = 0 \quad at \quad x = -L/2 \\ \phi = 1 \quad at \quad x = L/2 \\ \dfrac{\partial \phi}{\partial y} = 0 \quad at \quad y = -L/2 \\ \dfrac{\partial \phi}{\partial y} = 0 \quad at \quad y = L/2 \\ \dfrac{\partial \phi}{\partial z} = 0 \quad at \quad z = -L/2 \\ \dfrac{\partial \phi}{\partial z} = 0 \quad at \quad z = L/2 \end{cases} \tag{4.47}$$

The other parameters are: the particle permittivity $\varepsilon_2 = 1$, the fluid permittivity $\varepsilon_1 = 20$, and the radius of the particle $R = 0.2L$. The objective of this simulation is to quantitatively compare the electric field solution with the known analytic solution for a particle in an infinite domain in Equations (4.1) and (4.2). The computational domain size is chosen large enough compared to the particle size so that such a comparison can be done.

Figures (4.3) and (4.4) show the analytic and numerical potential fields, respectively. We have confirmed that the quantitative agreement between the two solutions is very good.

Next we consider the electrical body force. It can be shown that in case of materials with constant permittivities, no bulk charge, and an imposed DC field, the body force $\nabla \cdot \boldsymbol{\sigma}_M = 0$ [**40**]. This is because according to Equation (4.23) there two contributions to the body

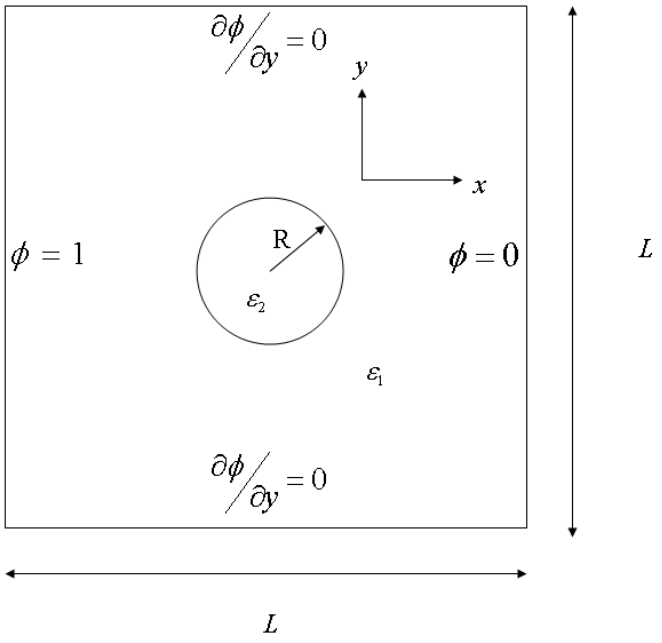

Figure 4.2. The view in a x-y plane (except the front and back walls) of a three-dimensional domain to compute the electric field and the electrical force. The imposed electric field is uniform in the farfield.

force. The second term is zero since $\nabla\varepsilon = 0$ in the fluid and particle domains where the permittivities are constant. The first term on the right hand side of Equation (4.23) is also zero because $\nabla \cdot (\varepsilon \mathbf{E}) = 0$ when there is no bulk charge in the domain. However, there is a surface force on the particle due to the jump in the permittivities [**40**]. In our immersed boundary approach, this surface force appears as a bulk force at the particle boundary region where the permittivity changes from its value in the bulk liquid to that of the bulk solid. Figure (4.5) shows the x component of the body force term $\nabla \cdot \boldsymbol{\sigma}_M$ in the fluid-particle domain calculated according to Equation (4.23). It is in agreement with the discussion above. The body force is zero in the bulk fluid and particle domains, and it is non-zero only in the particle boundary region. It is also noted that the force distribution is symmetric as expected for this problem so that there is no net force on the particle. Similar trend is

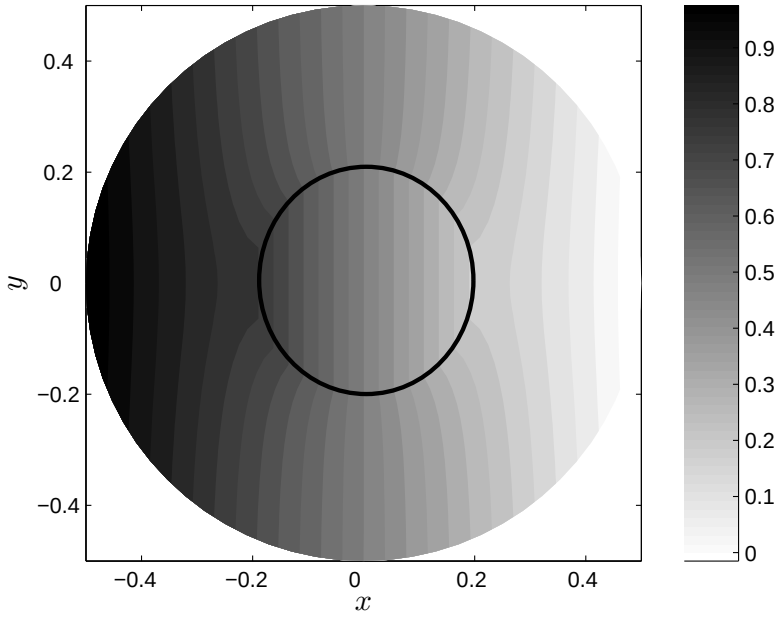

Figure 4.3. The analytic solution of the electrostatic potential for a particle in an infinite domain. The solution in the mid-x-y plane is shown.

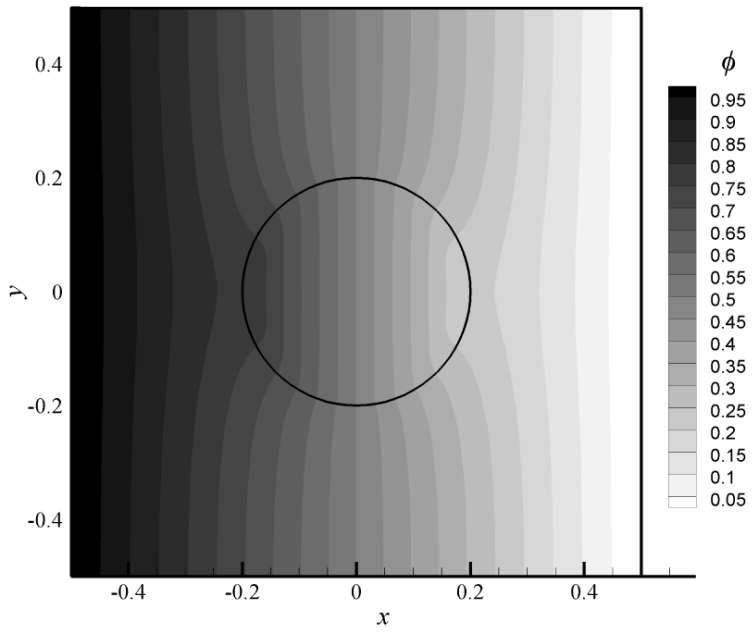

Figure 4.4. The 3D numerical solution of the electrostatic potential for a particle in a large cubic domain. The solution in the mid-x-y plane is shown.

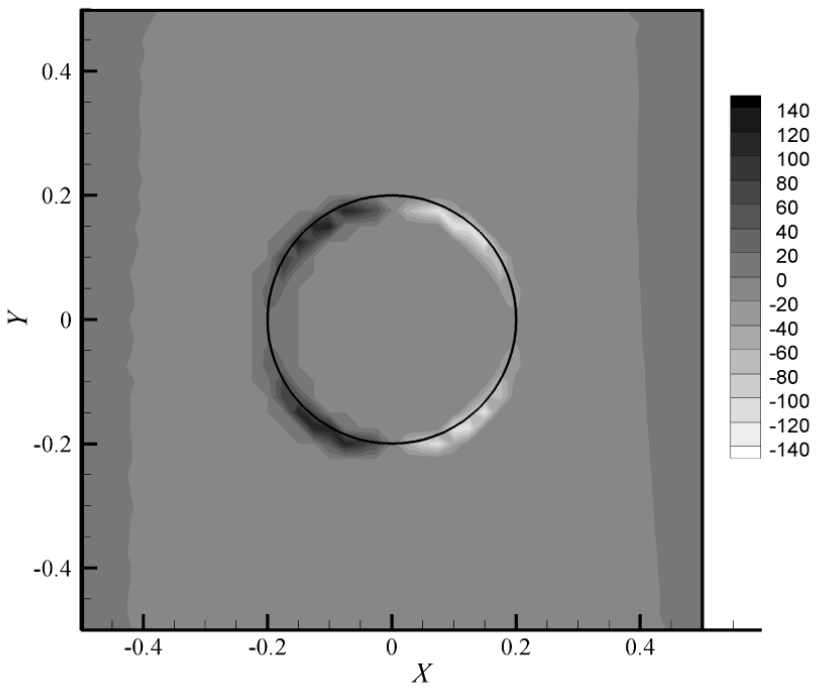

Figure 4.5. The x-component of the electrical body force shown in the mid x-y plane of the domain.

observed for other components of force. This also leads to a zero net torque on the body as expected in this case.

4.4.2. Computation of electrohydrodynamic particulate motion

In this section, we consider the problem of fluid-particle motion cause by electrical force, specifically the DEP force. All the domain of computation simulations for the electrohydrdynamic particulate motion is a cubic box of length $L = 2$ filled with fluid, and one spherical particle is placed in the center of the box. Particle radius is $R = 0.15$. The grid size is $\Delta x = \Delta y = \Delta z = 0.05$. The fluid properties were taken as: density $\rho_f = 2$, and viscosity $\mu = 0.25$. The density of the particle is $\rho_s = 3$. The discrete time step $\Delta t = 0.005$.

4.4.2.1. Uniform DC electric field. The case of a uniform DC field imposed in the far field was considered in the previous section (Figures 4.2 - 4.4). The electric field was

solved and the electrical body force was computed. In this section we report the solution of fluid-particle motion according to the algorithm described in section (4.3.4).

As discussed before, there is no net force on the particle in this configuration. This is expected. The particle has no net charge hence there will be no electrophoretic force. Additionally, it is in a uniform electric field in the farfield hence there will be no net DEP force (see Equation 4.8) according to the approximate dipole moment theory. Hence, the particle should not move from its original position when we solve the equations for fluid-particle motion. Indeed, in our simulations the particle did not change its position with time.

Figure (4.6) shows a plot of $|\mathbf{E}|^2$. Note that, as expected, there is no gradient in the magnitude of the electric field in the farfield.

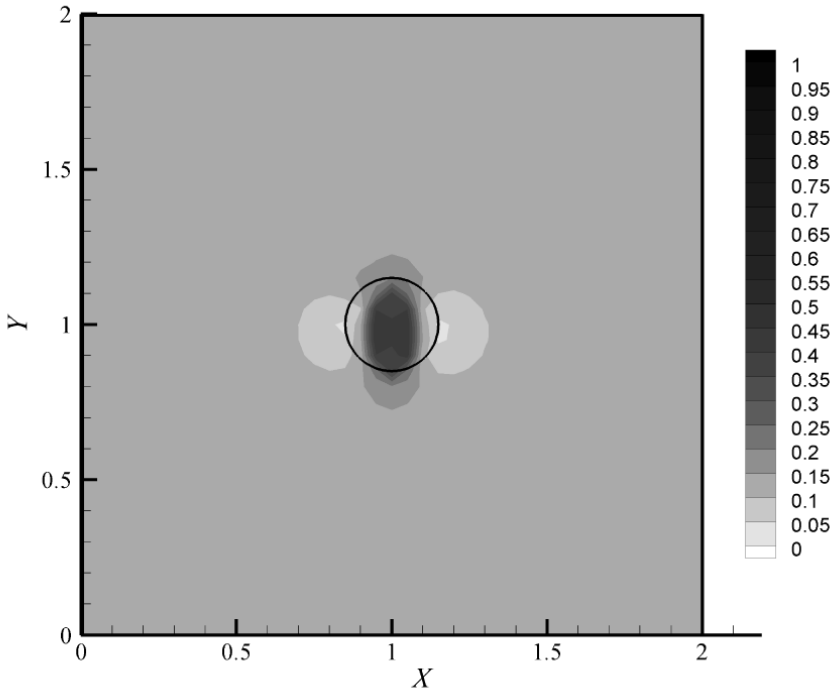

Figure 4.6. A plot of the square of the magnitude of the electric field.

4.4.2.2. Non-uniform DC electric field. As implied by Equation (4.8) positive DEP should be observed in DC fields when $\varepsilon_2 > \varepsilon_1$, and negative DEP should be observed when $\varepsilon_2 < \varepsilon_1$. In this section, the numerical approach will be tested on this aspect.

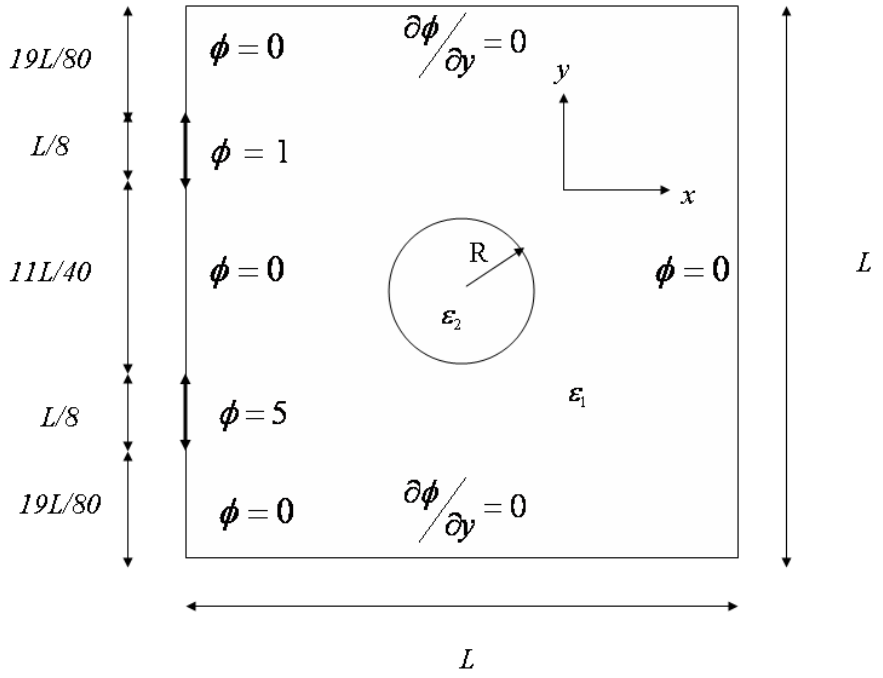

Figure 4.7. The view in a x-y plane (except the front and back walls) of a three-dimensional domain to simulate particle motion in a non-uniform DC field.

Figure (4.7) shows the domain in all x-y planes, except the front and back walls, to simulate positive and negative DEP in a non-uniform external DC field. The potential is applied on the left and right sides, as shown, to generate a non-uniform electric field. The normal components of the gradient of potential are zero at all other boundary locations. The non-uniform electric field should cause the particle to migrate due to the DEP force. The direction of migration should depend on the permittivity of the particle relative to that of the fluid. These cases are considered next corresponding to negative and positive DEP.

Negative dielectrophoresis in a DC field: To simulate negative DEP we chose particle permittivity $\varepsilon_2 = 1$ and the fluid permittivity $\varepsilon_1 = 20$. The domain size $L = 2$ in all directions, and the particle radius $R = 0.15$ (see Figure 4.7). In this case, the dipole

moment theory (Equation 4.8) implies that the particle should migrate toward a region of lower magnitude of the electric field.

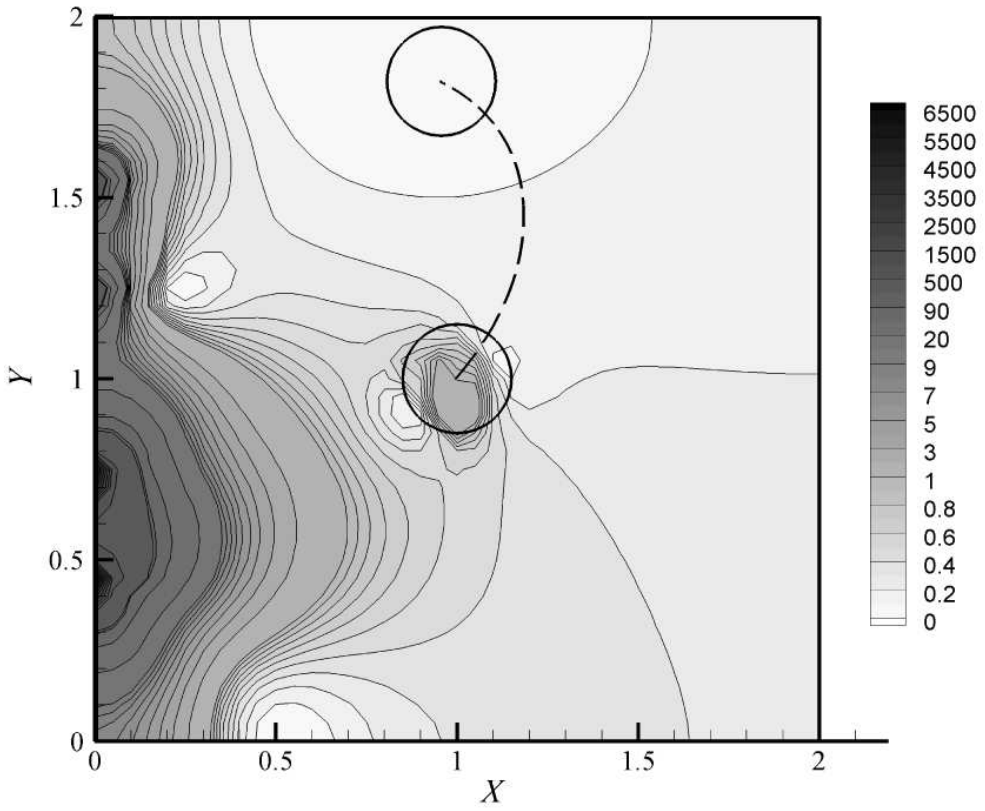

Figure 4.8. Negative DEP in a DC field: Numerically computed trajectory of the particle center in a non-uniform electric field when $\varepsilon_1 > \varepsilon_2$. The mid-$x$-$y$ plane is shown. The contour lines show $|\mathbf{E}|^2$ at the initial instant when the particle is at the center of the domain.

Figure (4.8) shows the computed trajectory of the particle center for this case. The contour lines show $|\mathbf{E}|^2$ at the initial instant when the particle is at the center of the domain. These contour lines change as the particle moves, however, the plot for the initial instant is still useful in identifying regions of high and low electric fields in the domain. It is seen that, as expected, in this case where $\varepsilon_1 > \varepsilon_2$ the particle migrates toward a region of low electric field intensity.

Positive dielectrophoresis in a DC field: To simulate positive DEP we chose particle permittivity $\varepsilon_2 = 20$ and the fluid permittivity $\varepsilon_1 = 1$. All the other parameters are same as that in the negative DEP case including the geometry (see Figure 4.7). In this case, the dipole moment theory (Equation 4.8) implies that the particle should migrate toward a region of higher magnitude of the electric field.

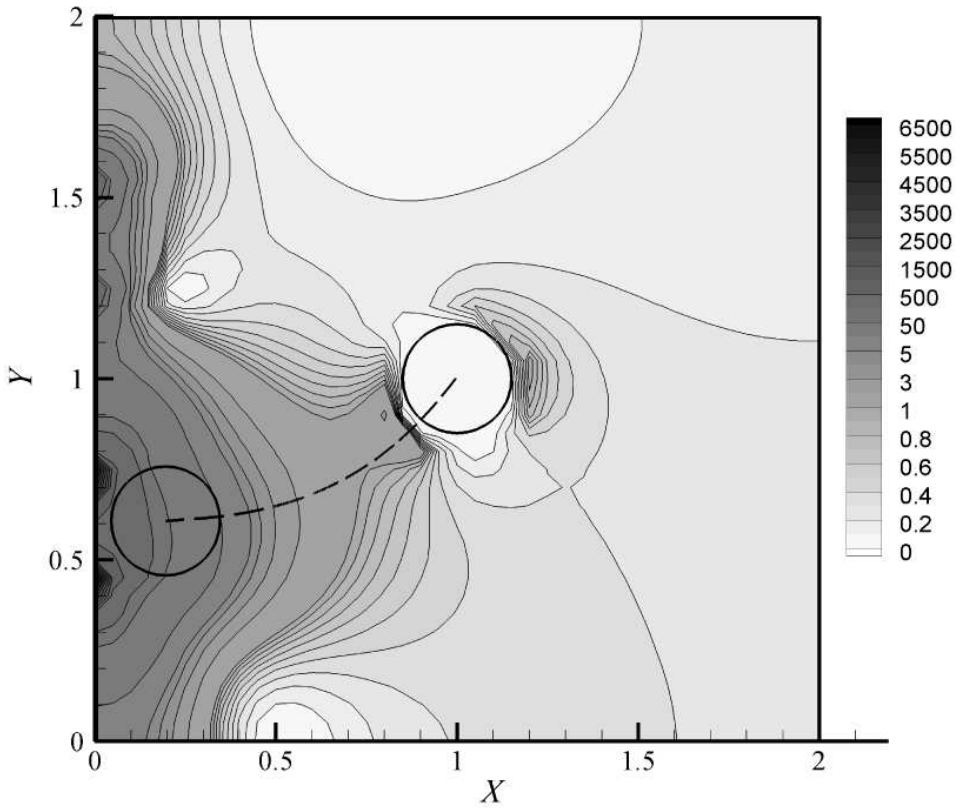

Figure 4.9. Positive DEP in a DC field: Numerically computed trajectory of the particle center in a non-uniform electric field when $\varepsilon_1 < \varepsilon_2$. The mid-$x$-$y$ plane is shown. The contour lines show $|\mathbf{E}|^2$ at the initial instant when the particle is at the center of the domain.

Figure (4.9) shows the computed trajectory of the particle center for this case. Once again the contour lines of $|\mathbf{E}|^2$ at the initial instant are shown to identify regions of high and low electric field intensity. From Figure (4.9) the maximum electric field intensity is found to be around $x = 0$ and between $y = 0.5$ and $y = 0.75$. By the dipole moment theory

(Equation 4.8) the particle should be attracted to that location. Figure (4.9) shows that the particle is indeed attracted to the location of the maximum electric field intensity.

4.4.2.3. Non-uniform AC electric field. In this part, dielectrophoresis in non-uniform AC fields is considered. Specifically we want to test the code for frequency dependent DEP behavior. Hence, we fix the material parameters. The fluid permittivity $\varepsilon_1 = 20$, and conductivity $\sigma_1 = 1.818 \times 10^{-3}$. The particle permittivity is chosen to be $\varepsilon_1 = 1$, and conductivity $\sigma_1 = 1.818 \times 10^{-1}$.

The above choice of parameters imply that $\sigma_2 > \sigma_1$ and $\varepsilon_2 < \varepsilon_1$. Using Equation (4.12), the Maxwell-Wagner charge relaxation time τ_{MW} is:

$$\tau_{MW} = \frac{\varepsilon_2 + \varepsilon_1}{\sigma_2 + \sigma_1} = \frac{20 + 1}{1.818 \times 10^{-3} + 2 \times 1.818 \times 10^{-1}} = 57.4684$$

The AC frequencies are chosen to be 10^{-6}, 10^{-5}, 10^{-3}, 10^{-1}, and 10^{3} defining Cases 1-5. According to the dipole moment theory, to determine whether there will be positive or negative DEP behavior in these cases, it is essential to know the sign of the real part of the Clausius-Mossotti factor, i.e. $Re[\underline{K}(\omega)]$ (Equation 4.11). $Re[\underline{K}(\omega)]$ vs. ω is plotted in Fig (4.10). It is seen that $Re[\underline{K}]$ is positive for Cases 1-3 at low frequencies and negative for Cases 4 and 5 at high frequencies. Hence, it is expected that Cases 1-3 should show positive DEP while Cases 4 and 5 show negative DEP.

Figure (4.11) shows the domain in all x-y planes, except the front and back walls, to simulate positive and negative DEP in a non-uniform AC field.

Positive DEP in an AC field: Figure (4.12), shows a plot for Case 1. A contour plot of the square of the RMS value of the magnitude of the electric field, i.e. E^2_{rms}, is shown in the figure. Following a derivation similar that for the mean value of the Maxwell stress, the RMS value of the electric field is given by

$$E^2_{rms} = \frac{1}{2}|\hat{\underline{\mathbf{E}}}|^2 = \frac{1}{2}\hat{\underline{\mathbf{E}}} \cdot \hat{\underline{\mathbf{E}}}^*. \tag{4.48}$$

The contour plot is shown for the initial location of the particle and identifies regions of high and low electric field intensities. According to the dipole moment theory (equation

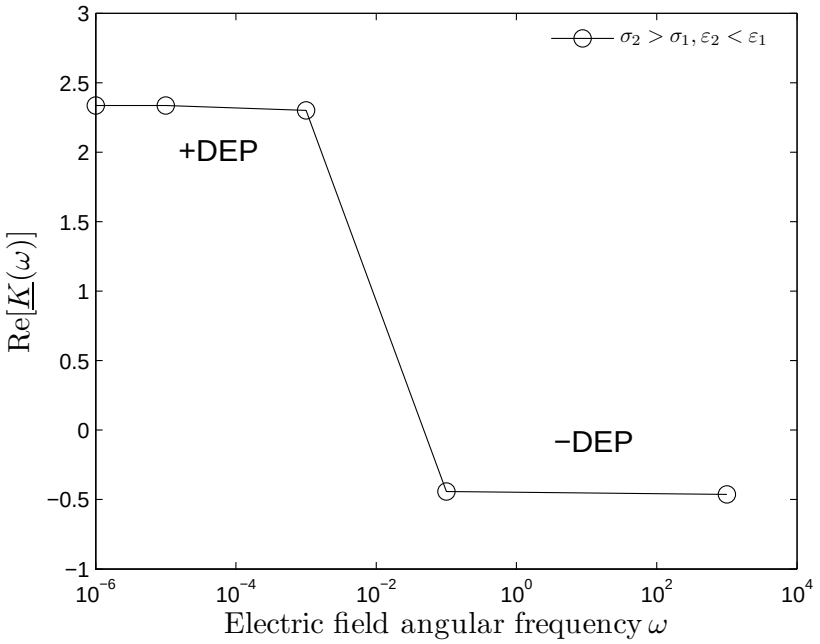

Figure 4.10. Plot of Clausius-Mossotti factor as a function of ω for the cases chosen to study positive and negative DEP in AC fields.

4.9) Case 1 should exhibit positive DEP and the particle should migrate toward the region of high electric field intensity. Figure (4.12) shows the numerically computed trajectory of the particle. As expected it migrates toward the region of high electric field intensity, thus showing positive DEP behavior. We verified that Cases 2 and 3 also show positive DEP behavior as was expected according to the dipole moment theory.

Negative DEP in an AC field: Figure (4.13), shows a plot for Case 5. A contour plot of E^2_{rms} is shown for the initial location of the particle and identifies regions of high and low electric field intensities. The figures also shows the numerically computed trajectory of the particle. As expected it migrates toward the region of low electric field intensity, thus showing negative DEP behavior. We verified that Case 4 also shows negative DEP behavior as was expected according to the dipole moment theory.

4.5. Conclusion

In this chapter a numerical technique for fully coupled simulation of electrohydrodynamic particulate flows was developed. Such a tool was not reported previously in literature

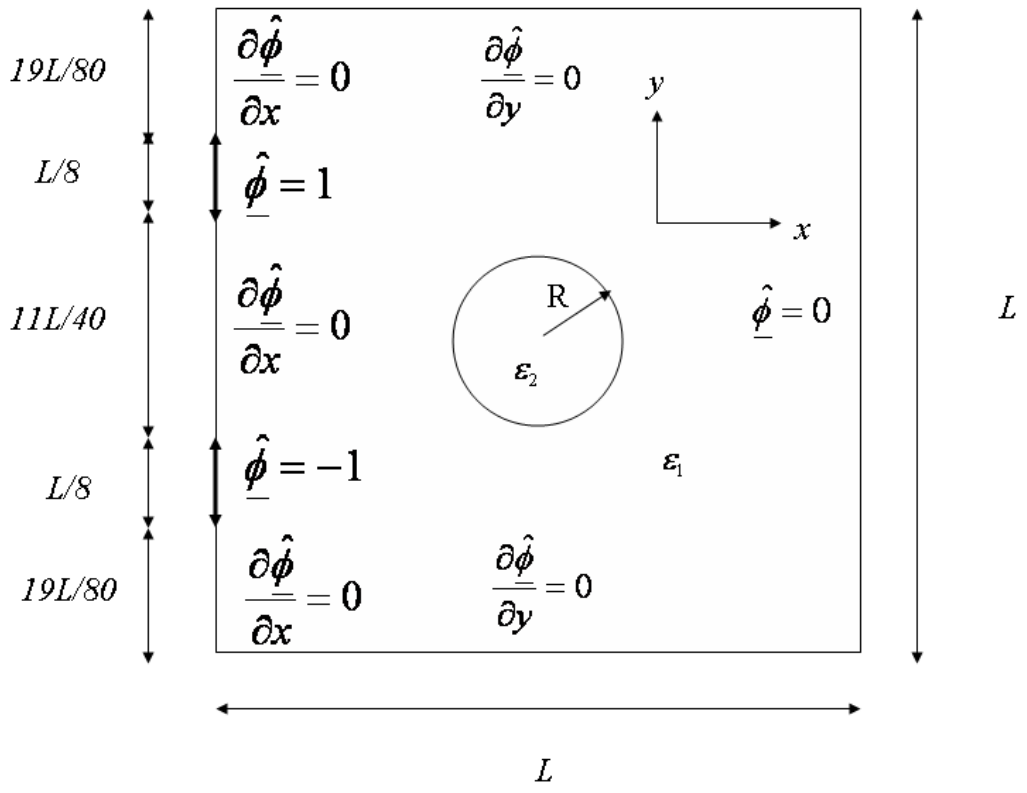

Figure 4.11. The view in a x-y plane (except the front and back walls) of a three-dimensional domain to simulate particle motion in a non-uniform AC field.

and has potential use in several micro- and nano-scale fabrication processes that rely on electrohydrodynamic self-assembly of particles. We have tested this approach for all the basic dielectrophoretic behaviors expected in DC and AC fields. Further development of this approach was undertaken in collaboration with Prof. W.-K. Liu, and more details on its quantitative performance and its application to carbon nanotubes can be found elsewhere [**44**].

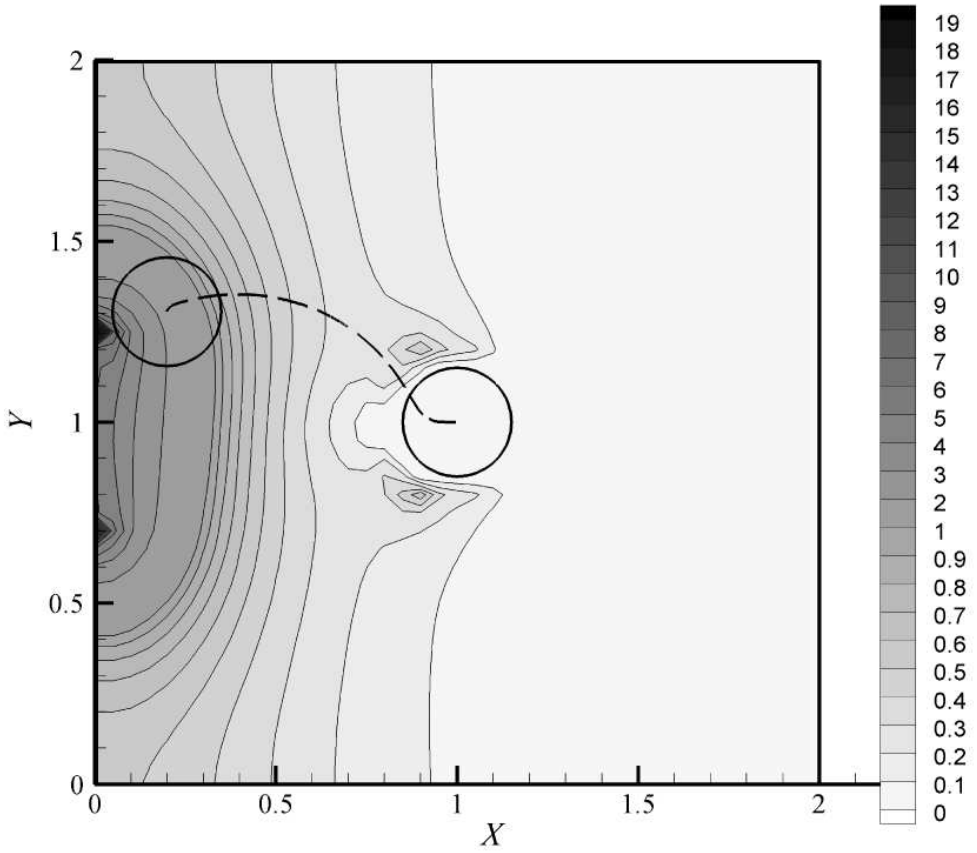

Figure 4.12. Positive DEP in an AC field: The contour lines show E^2_{rms} for Case 1 ($\varepsilon_1 = 20, \varepsilon_2 = 1, \sigma_1 = 1.818 \times 10^{-3}, \sigma_2 = 1.818 \times 10^{-1}$, and $\omega = 10^{-6}$) at the initial instant when the particle is at the center of the domain. The mid-x-y plane is shown. A numerically computed trajectory of the particle center is also shown.

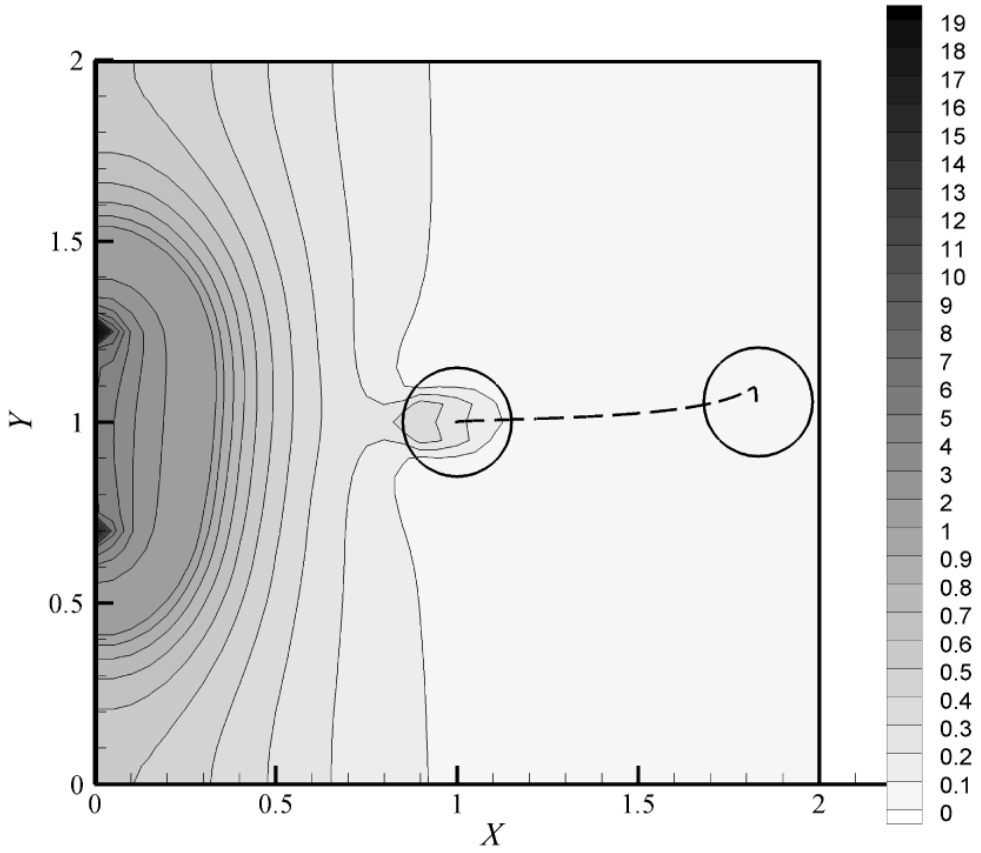

Figure 4.13. Negative DEP in an AC field: The contour lines show E^2_{rms} for Case 5 ($\varepsilon_1 = 20, \varepsilon_2 = 1, \sigma_1 = 1.818 \times 10^{-3}, \sigma_2 = 1.818 \times 10^{-1}$, and $\omega = 10^3$) at the initial instant when the particle is at the center of the domain. The mid-x-y plane is shown. A numerically computed trajectory of the particle center is also shown.

CHAPTER 5

A continuum approach to reproduce molecular scale slip behavior

5.1. Introduction

In continuum fluid dynamics, the no-slip boundary condition is typically used. This implies that fluid adjacent to the surface of a solid boundary moves at the same tangential velocity as the solid. The resistance in micro and nano scale channels is large due to which it costs more energy to pump the fluid through the channel. In this case, slip next to the wall can be helpful to reduce the flow resistance and thus reduce the energy requirement [**27, 28, 29, 30, 31**].

Slip at the fluid-solid interface has been investigated experimentally, numerically, and analytically [**17, 18, 20, 21, 3, 22, 55, 23, 24, 25, 56, 57, 58, 59**]. Molecular dynamic (MD) simulations have been useful to study the molecular behavior at the fluid-solid interface. The most common approach is the soft sphere model with Lennard-Jones potential [**32, 2, 23, 18, 19, 20, 21, 3, 22, 55, 24**]. Prior work in literature, based on molecular methods, has provided important insights into the mechanism of slip. However, the best methodology to seamlessly couple the near wall slip behavior to continuum approaches needs to be explored.

Coupling near wall slip, governed primarily by molecular scale effects, with continuum equations in the outer region is necessary in multiscale simulation of micro/nanoscale channels. Such simulations are useful for micro/nanofluidic device design. Typical strategies include coupling a molecular domain at the fluid-solid interface, where molecular dynamic simulations are performed, with outer regions where continuum simulations are reasonable [**60, 61**]. These strategies are computationally challenging for at least two reasons. First, in multiscale problems with fluids, the molecules in the molecular domain do not have fixed identity. This is unlike multiscale approaches for solid mechanics where molecules do not

diffuse in and out of the molecular domain. It is not trivial to resolve this issue [**60**]. Second, continuum scale phenomena outside the molecular domain are typically governed by time scales that are much longer than the molecular times scales at which molecular dynamic simulations must be done. Resolution of this issue is also non-trivial. One way to address these issues is to explore if molecular scale effects can be included in the continuum equations by suitably modifying them.

In this chapter it is explored if it is possible to reproduce molecular scale slip behavior through continuum equations. The primary objective is to gain insights into the molecular scale mechanism of slip in the context of continuum equations. Successful completion of this goal is potentially useful in developing multiscale computational strategies that resolve the two key challenges stated above.

5.2. Background

In the discussion to follow, we will refer to slip velocity and slip length. For the purposes of the discussion in this chapter, these variables are as defined in Figure (5.1). It shows shear flow next to a wall, where the wall molecules (or atoms) are located at $y = 0$. The mean velocity of any wall molecule is zero. Next to the wall molecules are shown the first two layers of fluid molecules (or atoms). As will be discussed later, the first layer of fluid molecules plays a dominant role in the mechanism of slip. The first layer is defined as the location of the first peak in the density profile of the fluid next to the wall.

The velocity profile of the fluid is linear in a Couette flow. This profile when extrapolated to the location of the wall molecules, i.e. to $y = 0$, should give velocity equal to zero if no-slip is valid. However, it has been reported that this velocity can be non-zero. This is called the slip velocity V_s (see Figure 5.1). The velocity profile of the fluid can also be extrapolated further to find the location where the velocity is zero. That gives the slip length L_s (see Figure 5.1). The slip velocity and slip length are related by

$$V_s = L_s \dot{\gamma}, \tag{5.1}$$

where $\dot{\gamma}$ is the shear-rate as shown in Figure (5.1).

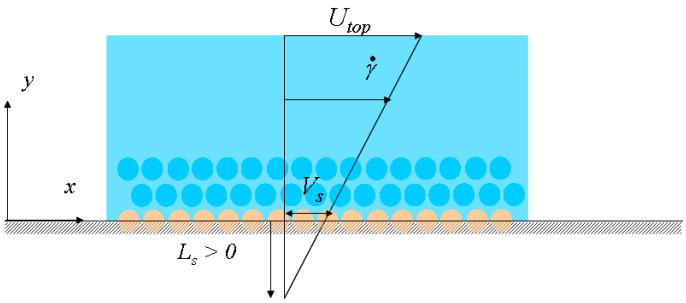

Figure 5.1. Definition of slip velocity and slip length.

Slip velocity for flows next to both hydrophobic and hydrophilic surfaces has been studied experimentally. The reported slip lengths range from 20nm to $1\mu m$ [**56, 25, 58**]. While the accuracy of the values has been debated, it is generally agreed that slip occurs at fluid-solid interfaces [**57**].

The presence of slip next to solid walls has been attributed to the depletion of fluid density next to solid walls [**62, 57**]. The primary motivation for this suggestion is the observation that hydrophobic surfaces, which tend to cause high depletion of fluid density [**63**], exhibit much larger slip [**58**].

Good insight into the mechanism of slip is obtained from prior analytic and computational work in literature [**32, 2, 23, 18, 19, 20, 21, 3, 22, 55, 24, 64, 65, 66, 67**]. Specifically, Lichter and co-workers [**21, 22, 3, 20, 55**] have elucidated the various mechanisms of slip. They note that fluid molecules next to the wall experience an interaction potential (e.g. the Lennard-Jones potential). As a result, the fluid molecules tend to occupy locations of low potential along the wall and stay away from locations of high potential. They showed, by using MD and a new variable-density Frenkel-Kontorova model, that local defects in the occupancy of the low potential locations propagate in the presence of shear. This leads to slip of the fluid molecules in the first layer at low shear rates. This was termed the defect propagation mechanism of slip [**22, 3**]. At high shear rates it was shown that slip occurs concurrently, i.e., the fluid molecules slip collectively rather by defect propagation. In this case the wall potential does not play an important role; instead slip is primarily dependent

on the heat transfer between the fluid and wall molecules [**55, 3**]. Thus, in this regime, slip depends on the high shear rate friction coefficient between the fluid and wall molecules.

The above results can summarized by a plot of slip length vs. shear rate. At low shear rates the slip length is almost constant. After a critical shear rate the slip length increases. The rise in the slip length is unbounded if the wall molecules are fixed [**55, 3**] (i.e. there is no dissipation of heat from the fluid molecules to the wall molecules) as seen in the MD results by Thompson and Troian [**2**] in Figure (5.2). However, if the wall molecules have thermal motion, then heat can be dissipated to the wall molecules. In this case, the slip length reaches another constant value at high shear rates after the transition [**55, 3**](see Figure 5.3).

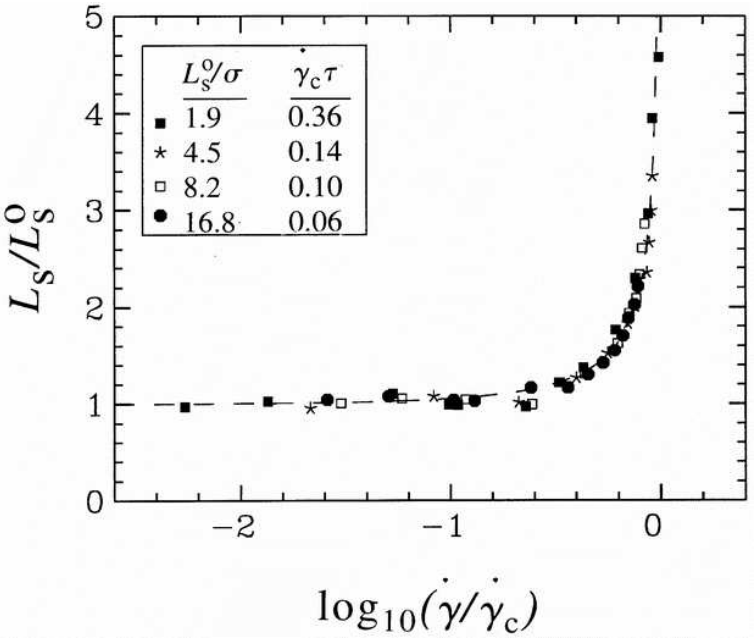

Figure 5.2. Slip length vs. shear rate from MD simulations [**2**].

In this work we ask the question: Is it possible to reproduce molecular scale slip behavior, described above, by using continuum equations? To that end we note that the continuum model must incorporate the following: i) near the wall, the fluid experiences a potential from the wall molecules and correspondingly a force due to the gradient in the potential, ii) the fluid density responds to the wall potential, hence, fluid compressibility is relevant, and iii) the fluid looses momentum to the wall at high shear rates even if the wall potential does

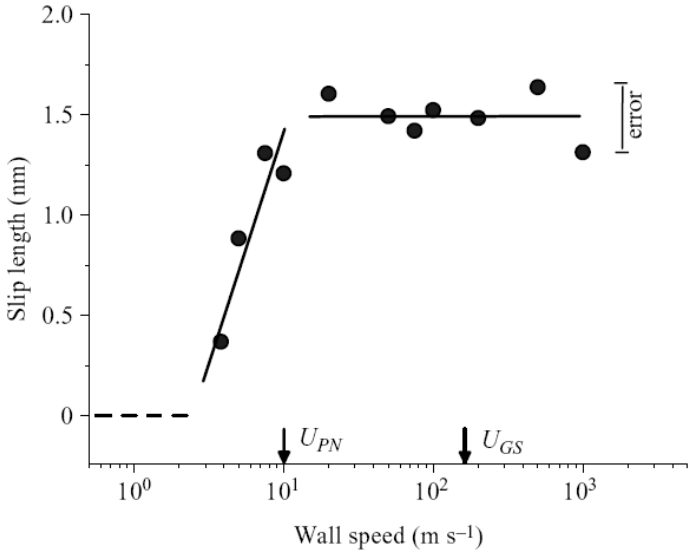

Figure 5.3. Slip length at high shear rate from MD simulations [**3**].

not play a significant role. To incorporate the above features, we simulate shear flow of a compressible fluid in the presence of a wall potential. A body force due to the wall potential is included in the momentum equation. Finally, a friction coefficient is used to capture the high shear rate dissipation at the wall.

It will be shown that this approach reproduces all the trends of slip length discussed above.

5.3. Governing equations

Shear flow of a compressible fluid is considered as shown in Figure (5.1). A two-dimensional domain is considered for simplicity. Conservation of mass for a compressible fluid is given by:

$$\frac{\partial \rho}{\partial t} + \nabla \cdot (\rho \mathbf{u}) = 0, \tag{5.2}$$

where $\mathbf{u}$ is the velocity field, and ρ is the density of the fluid. The momentum equation is:

$$\rho \frac{\partial \mathbf{u}}{\partial t} + \rho(\mathbf{u} \cdot \nabla)\mathbf{u} = -\nabla p + \mu \nabla^2 \mathbf{u} + \frac{1}{3}\mu \nabla(\nabla \cdot \mathbf{u}) - \rho \nabla \phi, \tag{5.3}$$

where p is the thermodynamic pressure, μ is the fluid viscosity, and ϕ is the potential imposed due to the wall molecules. The last term $-\rho\nabla\phi$ is the local body force per unit volume experienced by the fluid due to the wall potential. It will be seen that this term is crucial to reproduce the low shear rate slip behavior where the force due to the potential plays an important role. Gravity is not considered. Note that the fluid inertia is not important in this problem. This will be shown later. However, inertial and unsteady terms are retained while presenting the equations because the commercial code (FLUENT [**68**]) did not exclude these terms during computations.

Since the fluid is considered compressible, an equation of state is required. Here we make a simplifying assumption by considering an ideal gas equation of state. Once the viability of this approach to reproduce molecular scale slip is established then complex state equations for realistic fluids can be considered. The ideal gas state equation is:

$$p = \rho RT, \tag{5.4}$$

where T is the temperature in Kelvin, and R is the specific gas constant which depends on the molecular mass of the gas. $R = R_{\text{universal}}/M_{\text{molecular}}$, where $R_{\text{universal}} = 8314.34\text{J} - \text{kmol/K}$, and $M_{\text{molecular}}$ is the molecular weight of the gas in kg/kmole. An isothermal system will be assumed, hence, an energy equation for temperature will not be considered.

Our goal is to study slip next to a wall due to an imposed shear flow. To replicate that scenario, a non-zero potential ϕ is considered only next to the bottom wall. No potential is imposed next to the top wall. The potential ϕ will be discussed in section (5.4).

To impose a shear flow the x velocity component at the top boundary of the fluid domain is set to U_{top} (see Figure 5.1). The y velocity component is zero. At the location of the bottom wall, i.e. at $y = 0$, the following Navier boundary condition is applied:

$$\mu\frac{\partial u}{\partial y} = \eta_w(u - U_b), \tag{5.5}$$

where u is the x component of fluid velocity, η_w is the friction coefficient at the wall, and U_b is the x velocity component of the bottom wall. In our simulations, we use $U_b = 0$ i.e. the bottom wall is stationary. The y velocity component of the fluid at $y = 0$ is set to zero.

Some comments about the Navier boundary condition at $y = 0$ are in order. This condition by itself leads to slip between the fluid velocity and the wall velocity at $y = 0$. It will be seen that this boundary condition dominates the slip behavior only at high shear rates. Thus, η_w is a critical parameter to reproduce the high shear rate slip behavior. It is the friction coefficient that would arise due to the energy dissipated to the wall molecules (i.e. if there is heat transfer to the wall) in MD simulations at high shear rates. If the wall molecules are assumed fixed, then no energy is dissipated to the wall molecules (i.e. there is no heat transfer to the wall) [**55**] and it would correspond to $\eta_w = 0$.

Periodic boundary conditions are used with respect to the x direction.

The governing equations are solved in a non-dimensional form (see section 5.5) using a commercial solver FLUENT [**68**]. Only steady state solution to the governing equations are reported. Grid sensitivity tests were done to ensure that the solution is not dependent on the grid size.

5.4. The wall potential

In this section, the choice of potential ϕ used in equation (5.3) is discussed. In prior results it has been suggested that the influence of the wall potential on the first fluid layer is dominant [**22**]. Thus, one approach to obtain ϕ is to suitably integrate the molecular potential imposed by the wall molecules on the fluid molecules. This would imply integrating the Lennard-Jones potential for Lennard-Jones solid and fluid.

Another approach is based on deducing the effective potential ϕ based on the density profile obtained from MD simulation of a stationary fluid next to the wall. Consider, for example, the density profile of a stationary fluid as a function of the distance from the wall molecules obtained from MD simulations (Figure 5.4). This density profile shows the well known layering of fluid molecules next to the wall as indicated by the successive peaks in

density. Using this density profile, equation (5.3) with $\mathbf{u} = \mathbf{0}$, and the ideal gas equation of state, ϕ can be obtained as follows:

$$\left.\begin{aligned} &-\nabla(\rho RT) - \rho\nabla\phi = 0, \\ &\Rightarrow -RT\nabla(\ln\rho) - \nabla\phi = 0, \\ &\Rightarrow \nabla(\ln\rho) = -\frac{\nabla\phi}{RT}, \\ &\Rightarrow e^{-\frac{\phi}{RT}} = \frac{\rho}{\rho_{\text{bulk}}}, \\ &\Rightarrow \phi = -RT\ln(\frac{\rho}{\rho_{\text{bulk}}}), \end{aligned}\right\} \tag{5.6}$$

where ρ_{bulk} is the density of the fluid far from the wall where the ϕ is zero. Figure (5.5) shows ϕ computed according to equation (5.6) by using the density profile shown in Figure (5.4). This ϕ can be used in equation (5.3) for shear flow simulations as well.

It should be noted that ϕ obtained from equation (5.6) is an effective potential experienced by the fluid. It is not equal to the wall potential. ϕ from equation (5.6) will be dominated by the wall potential in the first fluid layer, however, the undulating nature of ϕ beyond the first layer (see Figure 5.5) is also influenced by the potential exerted by the fluid molecules on subsequent layers.

By using ϕ as obtained from equation (5.6) for shear flows as well, we assume that it is not strongly dependent on the shear rate. While this is a simplifying assumption, a favorable comparison between our results, to be presented later, with prior MD calculations suggests that this is reasonable.

In summary, one MD computation near the wall at stationary state can be done to yield a density profile. The effective potential ϕ can then be computed according to equation (5.6). ϕ thus computed can be used in equation (5.3) for continuum calculations of shear flows.

In this work, for convenience of numerical simulation and parametric investigation, a potential function is used that emulates the trends in Figure (5.5) [**69**]

$$\phi = \phi_{amp}e^{-ky}\cos(my)(1.1 + b\sin(nx)), \tag{5.7}$$

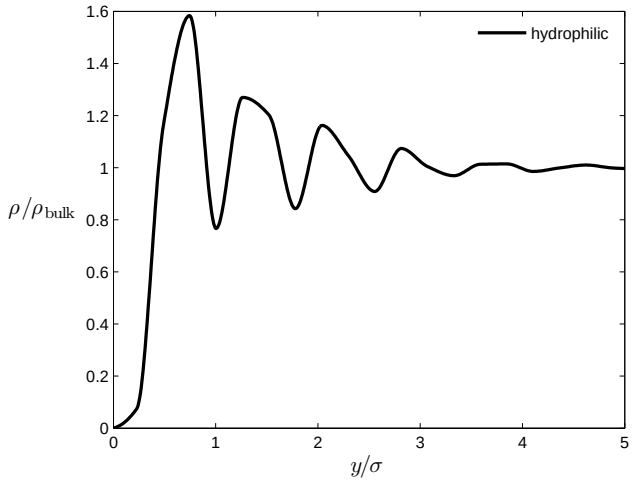

Figure 5.4. A typical profile of fluid density vs. the distance from the center of the wall molecules computed from MD calculations. Successive peaks indicate the layering of fluid molecules next to the wall. σ is the diameter of the fluid molecules in our MD calculations.

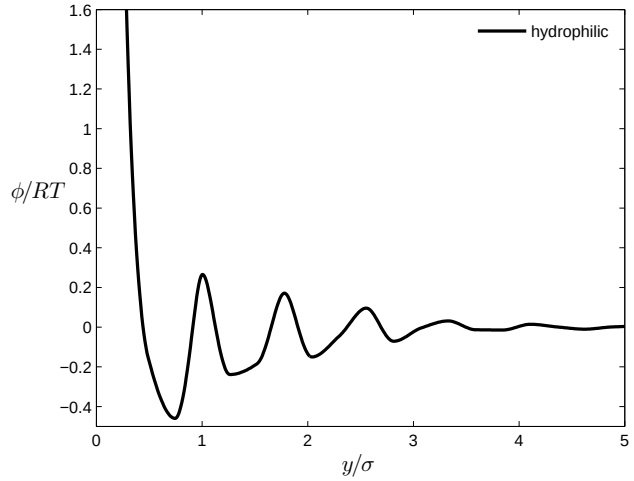

Figure 5.5. A typical profile of ϕ computed according to equation (5.6) by using the density profile shown in Figure (5.4).

where ϕ_{amp} is a parameter which controls the amplitude of the potential, k is a parameter for the exponential decay away from the wall, m and n are the wave numbers for the undulations in potential along the x and y directions. Note that undulations in the x direction are due to periodic spacing of the wall molecules along the wall, and undulations in the y direction are due to the layering of fluid molecules as seen in Figure (5.5). Adding 1.1 in the last part of equation (5.7) prevents ϕ from being equal to zero at $y = 0$, when $\sin(nx) = -1$. b is

another parameter that determines the degree of corrugation of the potential ϕ. Larger b implies more corrugation and vice-versa.

All computations in this work are done by using ϕ given by equation (5.7). The governing equations are solved in non-dimensional form. This is discussed in the next section.

5.5. Non-dimensionalization

To minimize roundoff errors, the governing equations were solved in non-dimensional form. The scales used are the following:

$$\left.\begin{aligned} &[\text{length}] = h, \\ &[\text{density}] = \rho_{\text{bulk}}, \\ &[\text{temperature}] = T_0, \\ &[\text{pressure}] = \rho_{\text{bulk}} R T_0, \\ &[\text{potential}] = R T_0, \end{aligned}\right\} \tag{5.8}$$

where h is the height of the domain in the y direction (see Figure 5.1), and T_0 is the constant specified temperature.

Using the scales above, the momentum equation (5.3) is non-dimensionalized as follows:

$$\begin{aligned} &\frac{[\text{density}][\text{velocity}]}{[\text{time}]}(\rho^* \frac{\partial \mathbf{u}^*}{\partial \text{t}^*}) + \frac{[\text{density}][\text{velocity}]^2}{[\text{length}]}\rho^*(\mathbf{u}^* \cdot \nabla^* \mathbf{u}^*) = -\frac{[\text{pressure}]}{[\text{length}]}\nabla^* p^* \\ &+ \frac{\mu[\text{velocity}]}{[\text{length}]^2}\nabla^{*2}\mathbf{u}^* + \frac{1}{3}\mu\frac{[\text{velocity}]}{[\text{length}]^2}\nabla^*(\nabla^* \cdot \mathbf{u}^*) - \frac{[\text{density}][\text{potential}]}{[\text{length}]}\rho^* \nabla^* \phi^*, \end{aligned} \tag{5.9}$$

where superscript $*$ denotes non-dimensional variables. By using time scale (if a transient problem is solved) equal to the length scale divided by velocity scale, equation (5.9) can be simplified as

$$\rho^* \frac{\partial \mathbf{u}^*}{\partial t^*} + \rho^*(\mathbf{u}^* \cdot \nabla^* \mathbf{u}^*) = -\frac{R T_0}{[\text{velocity}]^2}\nabla^* p^* + \frac{\mu}{\rho_{\text{bulk}}[\text{velocity}][\text{length}]}\nabla^{*2}\mathbf{u}^*$$

$$+\frac{\mu}{\rho_{\text{bulk}}[\text{velocity}][\text{length}]}\frac{1}{3}\nabla^*(\nabla^*\cdot\mathbf{u}^*)-\frac{RT_0}{[\text{velocity}]^2}\rho^*\nabla^*\phi^*. \tag{5.10}$$

The velocity scale is chosen as (it sets the coefficient of pressure equal to one)

$$[\text{velocity}]=\sqrt{RT_0}. \tag{5.11}$$

Note that velocity scale $\sqrt{RT_0}$ is not the actual velocity scale of the flow which is set by the velocity U_{top} of the top boundary of the domain. We keep U_{top} as a parameter of the problem just like it is done is typical MD calculations. The momentum equation can be rewritten in non-dimensional form as

$$\rho^*\frac{\partial\mathbf{u}^*}{\partial t^*}+\rho^*(\mathbf{u}^*\cdot\nabla^*\mathbf{u}^*)=-\nabla^*p^*+\mu^*\nabla^{*2}\mathbf{u}^*+\frac{1}{3}\mu^*\nabla^*(\nabla^*\cdot\mathbf{u}^*)-\rho^*\nabla^*\phi^*, \tag{5.12}$$

where μ^* is given by

$$\mu^*=\frac{\mu}{\rho_{\text{bulk}}\sqrt{RT_0}h}. \tag{5.13}$$

The non-dimensionalized continuity equation is given by

$$\frac{[\text{density}][\text{velocity}]}{[\text{length}]}\frac{\partial\rho^*}{\partial \text{t}^*}+\frac{[\text{density}][\text{velocity}]}{[\text{length}]}\nabla^*(\rho^*\mathbf{u}^*)=0, \tag{5.14}$$

$$\Rightarrow\frac{\partial\rho^*}{\partial t^*}+\nabla^*(\rho^*\mathbf{u}^*)=0. \tag{5.15}$$

The dimensionless form of the ideal gas equation of state is

$$[\text{pressure}]p^*=[\text{density}]\text{R}[\text{temperature}]\rho^*T^*, \tag{5.16}$$

$$\Rightarrow p^*=\rho^*, \tag{5.17}$$

where $T^* = 1$ by the choice of the temperature scale and the fact that the temperature is assumed constant. Similarly, the non-dimensional form of the potential equation becomes

$$\phi^* = \phi_a e^{-k^* y^*} \cos(m^* y^*)(1.1 + b^* \sin(n^* x^*)), \tag{5.18}$$

where $k^* = kh$, $m^* = mh$, $n^* = nh$, $b^* = b$, and $\phi_a = \phi_{amp}/RT_0$. Note that this is the potential due to the bottom wall only. No potential is imposed next to the top wall.

The boundary condition at the top boundary is $u^* = U^*_{top}$, where $U^*_{top} = U_{top}/\sqrt{RT_0}$. At the bottom boundary, i.e. at $y^* = 0$, the Navier boundary condition in equation (5.5) becomes

$$\left.\begin{aligned} &\mu \frac{\partial u}{\partial y} = \eta_w u, \\ &\Rightarrow \mu \frac{[\text{velocity}]}{[\text{length}]} \frac{\partial u^*}{\partial y^*} = \eta_w [\text{velocity}] u^*, \\ &\Rightarrow \frac{\partial u^*}{\partial y^*} = \frac{\eta_w h}{\mu} u^*, \\ &\Rightarrow \frac{\partial u^*}{\partial y^*} = f_w u^*, \end{aligned}\right\} \tag{5.19}$$

where f_w is the non-dimensional wall friction coefficient.

The scales chosen would be as follows if we consider values typical for air at room temperature:

$$\left.\begin{aligned} &T_0 = 300\text{K}, \\ &\text{R} = 287\text{J/kg} - \text{K}, \\ &\mu = 1.85 \times 10^{-5}\text{Ns/m}^2, \\ &\rho_{\text{bulk}} = 1.19\text{kg/m}^3, \\ &\mu^* = \frac{\mu}{\rho_{bulk}\sqrt{RT_0}h} = 52.98, \\ &[\text{length}] = 1\text{nm}, \\ &[\text{pressure}] = \rho_{\text{bulk}} RT_0 = 1.024 \times 10^5\text{Pa}, \\ &[\text{velocity}] = \sqrt{RT_0} = 293.43\text{m/s}, \\ &[\text{time}] = \frac{[\text{length}]}{[\text{velocity}]} \approx 3 \times 10^{-12}\text{s}. \end{aligned}\right\} \tag{5.20}$$

In typical MD simulations the scales are:

$$\left.\begin{aligned} &[\text{length}] \sim 1\text{nm}, \\ &[\text{time}] = \tau \sim \sqrt{\text{m}\sigma^2/\epsilon} \sim 10^{-12}s, \\ &[\text{velocity}] \sim (\sigma/\tau) \sim 10^2\text{m/s}, \end{aligned}\right\} \tag{5.21}$$

where m is the molecular mass, τ is the time scale for molecular motion, σ is the scale of the molecular diameter, and ϵ is a Lennard-Jones interaction parameter. Our choice of scaling is similar to the typical scaling used in MD calculations. It is also noted that it is not essential to use these scales, however, we have chosen these to make it easier to draw parallels with the MD results.

5.6. Results

Equations (5.12), (5.15), (5.17), and (5.18) are solved together with the boundary conditions at the top and bottom boundaries. Periodic boundary conditions are used in the x^* direction. The non-dimensional channel height h^* and length L^* are equal to one. Steady state solution is considered.

In the non-dimensional equations presented above, the parameters of the problems are μ^*, U^*_{top}, f_w, ϕ_a, b^*, k^*, m^*, and n^*. In the following subsections results are presented.

In the rest of this chapter, dimensionless dependent variables will be denoted by superscript $*$. Dependent variables without superscript $*$ are dimensional.

5.6.1. Effect of shear rate on the slip length

In this section the basic trends in the velocity profile and the slip length vs. the imposed shear rate are identified. The parameters chosen to solve shear flows are: $\mu^* = 10$, $\phi_a = 0.01$, $k^* = 8.5$, $m^* = n^* = 16\pi$, and $b^* = 1$. First, we consider $f_w = \dfrac{\eta_w h}{\mu} \to \infty$ which implies that the fluid velocity $u = 0$ at $y = 0$ which is the location of the bottom wall.

The shear flow is solved for different value of U^*_{top} so that different shear rates are imposed above the bottom wall. Higher the value of U^*_{top} higher is the imposed shear rate and vice-versa.

Figure (5.6) shows $\langle u \rangle / U_{top}$ with respect to y/h, where $\langle u \rangle$ is the value of the x component of fluid velocity that is averaged with respect to the x direction at any given y coordinate. It is seen that the normalized velocity profile has two limiting solutions (see a zoomed in view of the profile in Figure 5.7). At high shear rates (i.e. large values of U^*_{top}) the normalized velocity profile is linear and does not change upon further increasing the imposed shear rate. At low shear rates (i.e. small values of U^*_{top}) the normalized velocity profile does not change upon further decreasing the imposed shear rate.

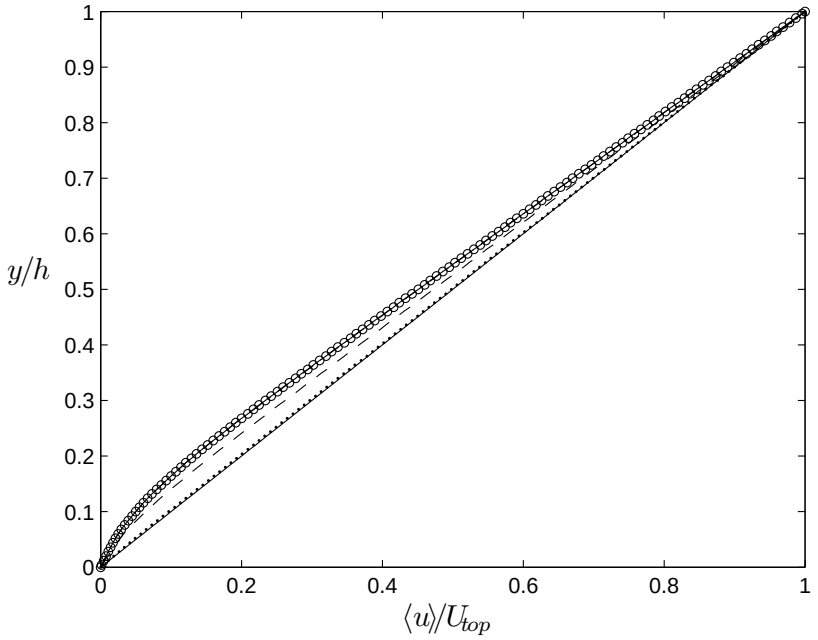

Figure 5.6. The mean velocity profile $\langle u \rangle / U_{top}$ vs. y/h. The parameters are: $\mu^* = 10$, $\phi_a = 0.01$, $k^* = 8.5$, $m^* = n^* = 16\pi$, $b^* = 1$, and $f_w \to \infty$. Legend: $(-)$ $U^*_{top} = 1$, $(\cdots)$ $U^*_{top} = 10^{-2}$, $(--)$ $U^*_{top} = 10^{-3}$, $(- \cdot -)$ $U^*_{top} = 10^{-5}$, and $(-\mathrm{o}-)$ $U^*_{top} = 10^{-7}$.

The imposed potential in equation (5.18) is sinusoidal with respect to the y direction to replicate the layering of fluid molecules next to the wall. Given our choice of $m^* = 16\pi$, this implies that the extent of the first layer is up to $y/h = 0.125$. It is seen from Figures (5.6) and (5.7) that the low shear rate limiting velocity profile is non-linear up to approximately $y/h = 0.125$ and linear beyond that. Thus, it is apparent that the first layer plays a dominant role by imposing an additional force that slows down the fluid next to the wall at low shear

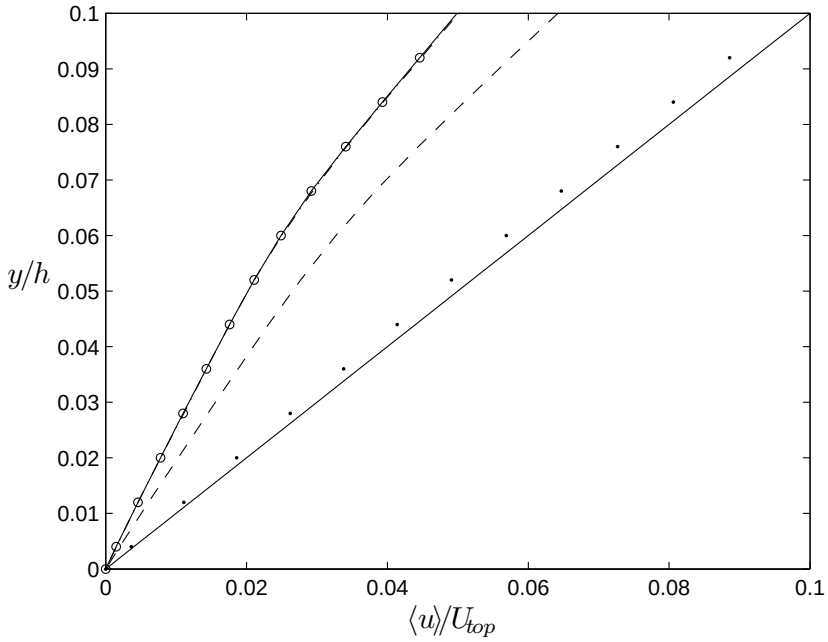

Figure 5.7. A zoomed in view of the mean velocity profile shown in Figure (5.6). Legend: $(-)$ $U^*_{top} = 1$, $(\cdots)$ $U^*_{top} = 10^{-2}$, $(--)$ $U^*_{top} = 10^{-3}$, $(- \cdot -)$ $U^*_{top} = 10^{-5}$, and $(-\text{o}-)$ $U^*_{top} = 10^{-7}$.

rates. This force balance and the mechanism of slip will be discussed further in section (5.6.2).

The transition from the limiting velocity profile in Figure (5.6) at low shear rates to that at high shear rate occurs beyond a critical shear rate. During transition the velocity profile is intermediate between the two limiting profiles. The mean imposed shear rate $\langle\dot{\gamma}\rangle$ is calculated as the slope of the velocity profile beyond the first fluid layer. The non-dimensional slip length L_s/h is calculated by extrapolating the linear velocity profile obtained beyond the first fluid layer in Figure (5.6) to the location of zero velocity (as depicted in Figure 5.1). In the present case, the slip length is negative since the intercept of the outer linear profile with the y/h axis happens above the coordinate of the wall (see the sign convention for the slip length in Figure 5.1).

The slip length L_s/h calculated as discussed above is shown in Figure (5.8). It is seen that at low shear rates the slip length is constant which transitions to another constant value at high shear rates. The constant slip lengths at low and high shear rates are a direct

consequence of the limiting profiles of the normalized velocity at low and high shear rates, respectively, depicted in Figure (5.6). This trend of slip length is consistent with prior MD calculations [**3**] and has been reproduced for the first time using a continuum approach. The transition from the low shear rate to the high shear rate slip lengths happens at a critical value of the shear rate; the estimation for which will be discussed in section (5.6.2). This estimation will also explain the scaling used for the imposed shear rate $\langle\dot{\gamma}\rangle$ in Figure (5.8).

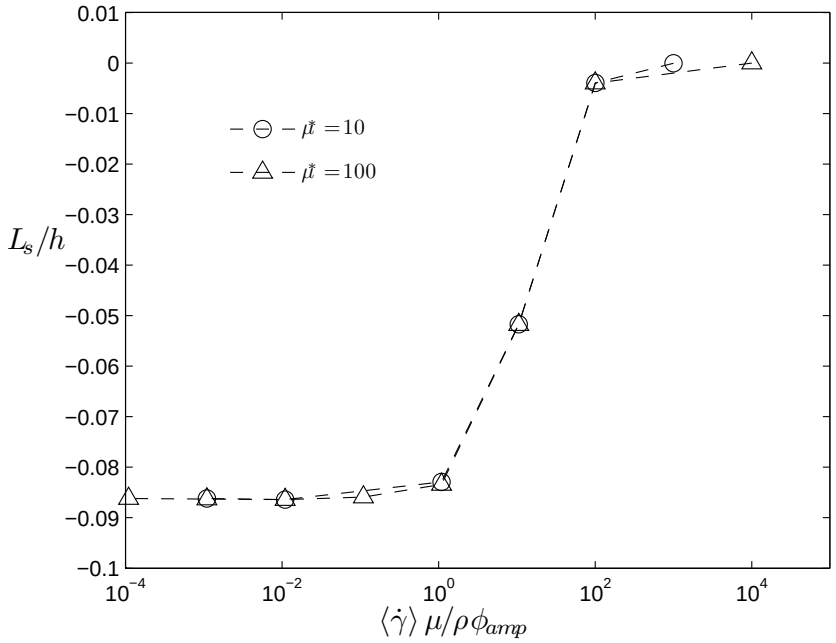

Figure 5.8. L_s/h vs. non-dimensionalized shear rate for $\phi_a = 0.01$, $k^* = 8.5$, $m^* = n^* = 16\pi$, $b^* = 1$, and $f_w \to \infty$.

To ensure that inertia does not play an important role, all calculations were repeated with $\mu^* = 100$. The resultant plot of the slip length did not change (see Figure 5.8). It was confirmed that in all the simulations the flow Reynolds number $Re = \dfrac{\rho_{bulk} U_{top} h}{\mu}$ was less than order one.

The overall trend of the velocity profile remains the same irrespective of the friction parameter f_w in the Navier boundary condition at the bottom wall (equation 5.5). Figure (5.9) shows velocity profiles for $f_w = 0.75$ and Figure (5.10) shows profiles for $f_w = 0$. Reducing the friction coefficient compared to the cases in Figure (5.6) leads to positive slip lengths at higher shear rate. Note that the limiting velocity profile at high shear rate for

$f_w = 0$ is vertical which corresponds to an infinite slip length. The effect of f_w on the slip length will be discussed in further details in section (5.6.3).

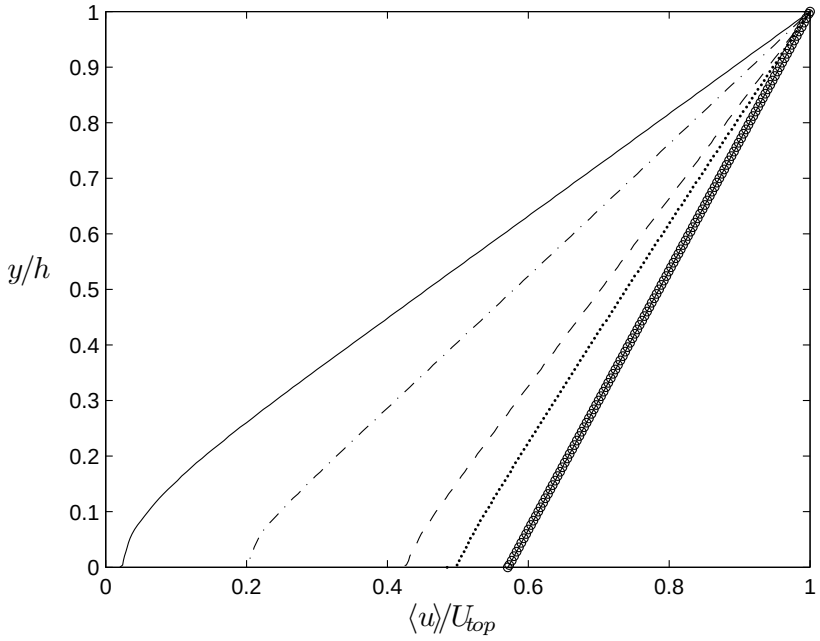

Figure 5.9. The mean velocity profile $\langle u \rangle / U_{top}$ vs. y/h. The parameters are: $\mu^* = 10$, $\phi_a = 0.01$, $k^* = 8.5$, $m^* = n^* = 16\pi$, $b^* = 1$, and $f_w = 0.75$. Legend: $(-\text{o}-)$ $U^*_{top} = 10^{+2}$, $(\cdots)$ $U^*_{top} = 3 \times 10^{-2}$, $(--)$ $U^*_{top} = 2 \times 10^{-2}$, $(- \cdot -)$ $U^*_{top} = 1.5 \times 10^{-2}$, $(-)$ $U^*_{top} = 1 \times 10^{-5}$.

Next we will focus on explaining the low and high shear rate behavior discussed above, and estimating the critical shear rate for transition.

5.6.2. The mechanism of slip

To understand the trends discussed in the previous section, we will focus on cases with the following parameters: $\mu^* = 10$, $\phi_a = 0.01$, $k^* = 8.5$, $m^* = n^* = 16\pi$, $b^* = 1$, and $f_w = 0.75$. The normalized velocity profiles corresponding to this case are shown in Figure (5.9) at different values of the imposed shear rate.

As discussed earlier, the velocity profiles at low shear rates imply that there is a net body force in the x direction acting in the first layer of fluid molecules next to the wall. At high shear rates this body force is unimportant as indicated by the linear velocity profile

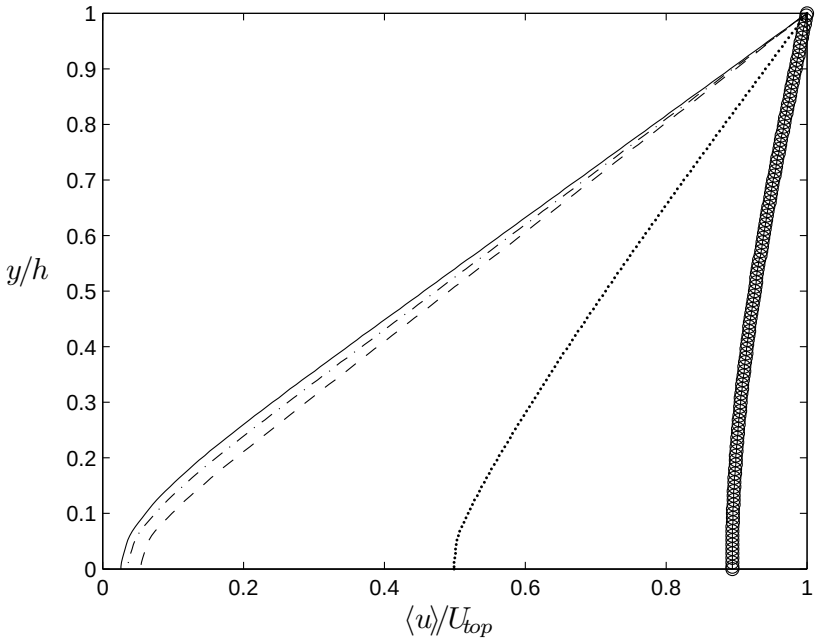

Figure 5.10. The mean velocity profile $\langle u \rangle / U_{top}$ vs. y/h. The parameters are: $\mu^* = 10$, $\phi_a = 0.01$, $k^* = 8.5$, $m^* = n^* = 16\pi$, $b^* = 1$, and $f_w = 0$. Legend: $(-\text{o}-)$ $U^*_{top} = 10^{-2}$, $(\cdots)$ $U^*_{top} = 2 \times 10^{-3}$, $(--)$ $U^*_{top} = 10^{-3}$, $(- \cdot -)$ $U^*_{top} = 5 \times 10^{-4}$, $(-)$ $U^*_{top} = 1 \times 10^{-6}$.

in the high shear rate limit. To understand the origin of this body force we consider the momentum equation (5.3). Given that inertia is unimportant (note that even if inertia were important this contribution would be zero due to the periodic boundary condition in the x direction), the flow is in steady state, and there is no net pressure gradient imposed in the x direction, the only source for the net body force in the x direction is the term due to the potential ϕ, i.e. $-\rho\nabla\phi$.

5.6.2.1. Density profiles at high and low shear rates. The force due to the potential is dependent on the density profile. Hence, we consider that next. Figure (5.11) shows the density profile with respect to the y direction at $x^* = 0.5$ which is the mid-axial location of the computational domain (similar plots can be drawn for other x locations). It is seen that the density profile shows layering, as expected, due to the imposed potential ϕ. This profile does not change significantly with the imposed shear rate. Specifically, the locations of peaks and valleys remain unchanged.

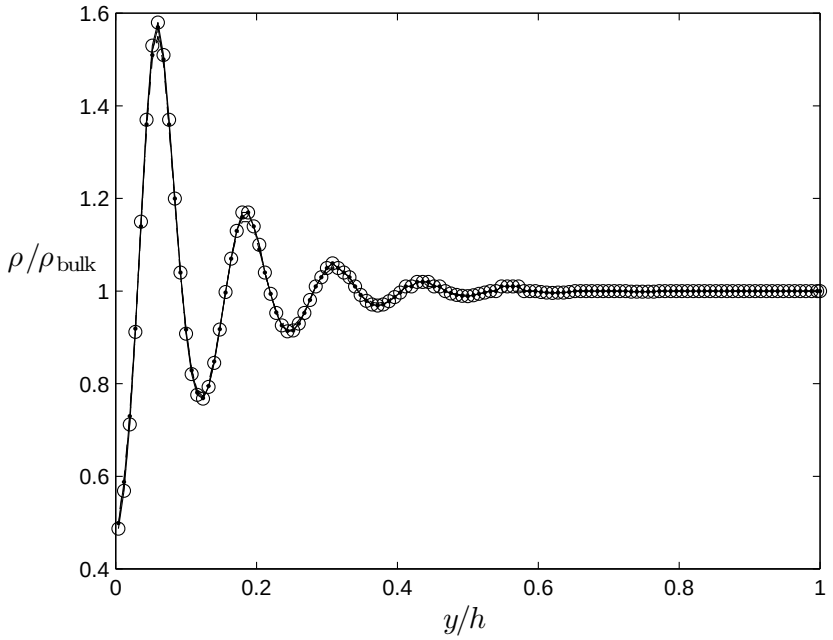

Figure 5.11. The density profile with respect to y/h at $x/h = 0.5$. The parameters are $\mu^* = 10$, $\phi_a = 0.01$, $k^* = 8.5$, $m^* = n^* = 16\pi$, $b^* = 1$, and $f_w = 0.75$.Legend: $(-\text{o}-)$ $U^*_{top} = 10^2$, $(\cdots)$ $U^*_{top} = 2 \times 10^{-2}$, $(--)$ $U^*_{top} = 1.5 \times 10^{-2}$, $(- \cdot -)$ $U^*_{top} = 10^{-2}$, $(-)$ $U^*_{top} = 10^{-5}$.

Figures (5.12) and (5.13) show the density profile with respect to the x direction at $y/h = 0.06$ which is the location of the first peak in fluid density next to the wall (see Figure 5.11). Thus, this is a plot of the density in the first layer of fluid molecules next to the wall. It is seen that the density profile strongly depends on the imposed shear rate. As the shear rate increases there are two effects: the peaks are reduced, and they shift. At high shear rates the density profile is almost constant with no undulations. The reduction of undulations in the density profile with respect to the imposed shear rate is quantified in Figure (5.14), where $\delta\rho = \rho_{max} - \rho_{min}$. $\delta\rho$ is calculated based on the density profiles as shown in Figure (5.12). Figure (5.14) delineates two distinct zones − one at low shear rates and another at high shear rates with a transition region beyond a critical shear rate. As expected, these low and high shear rate regions are in one-to-one correspondence with the limiting velocity profiles at low and high shear rates, respectively, shown in Figure (5.9).

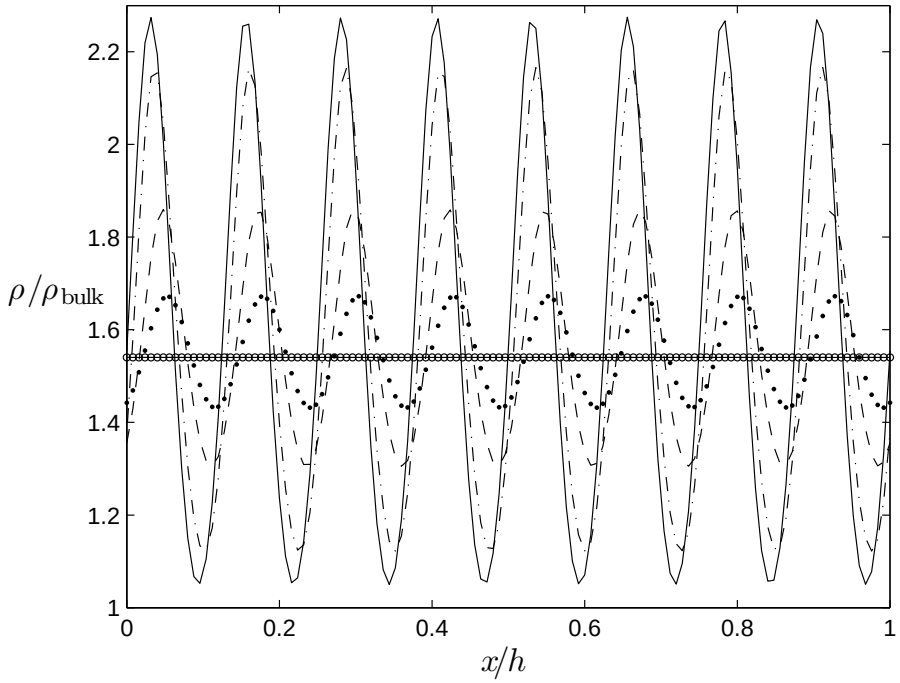

Figure 5.12. The density profile with respect to x/h at $y/h = 0.06$. The parameters are $\mu^* = 10$, $\phi_a = 0.01$, $k^* = 8.5$, $m^* = n^* = 16\pi$, $b^* = 1$, and $f_w = 0.75$. Legend: $(-\text{o}-)$ $U^*_{top} = 10^2$, $(\cdots)$ $U^*_{top} = 2 \times 10^{-2}$, $(--)$ $U^*_{top} = 1.5 \times 10^{-2}$, $(- \cdot -)$ $U^*_{top} = 10^{-2}$, $(-)$ $U^*_{top} = 10^{-5}$.

The above trend in the density profile with respect to the x direction is consistent with the results based on molecular methods [**21, 22, 3, 20, 55**]. Specifically, the low shear rate density profiles are consistent with the molecular scale mechanism based on defect propagation [**22, 3**]. The near constant density profile with respect to the x direction at high shear rates is also consistent with the molecular scale mechanism of collective slip [**22, 3**]. Thus, our approach is a valid continuum representation of the molecular scale dynamics that are relevant to reproduce the appropriate slip behavior.

5.6.2.2. Force balance at low and high shear rates. The force balance to explain the non-linear velocity profile at low shear rates and the linear velocity profile at high shear rates (Figure 5.9) is considered next. Integrating the x component of equation (5.3) with respect to the x direction leads to the following equation:

$$\mu \frac{d^2\langle u \rangle}{dy^2} = \langle \rho \frac{\partial \phi}{\partial x} \rangle, \tag{5.22}$$

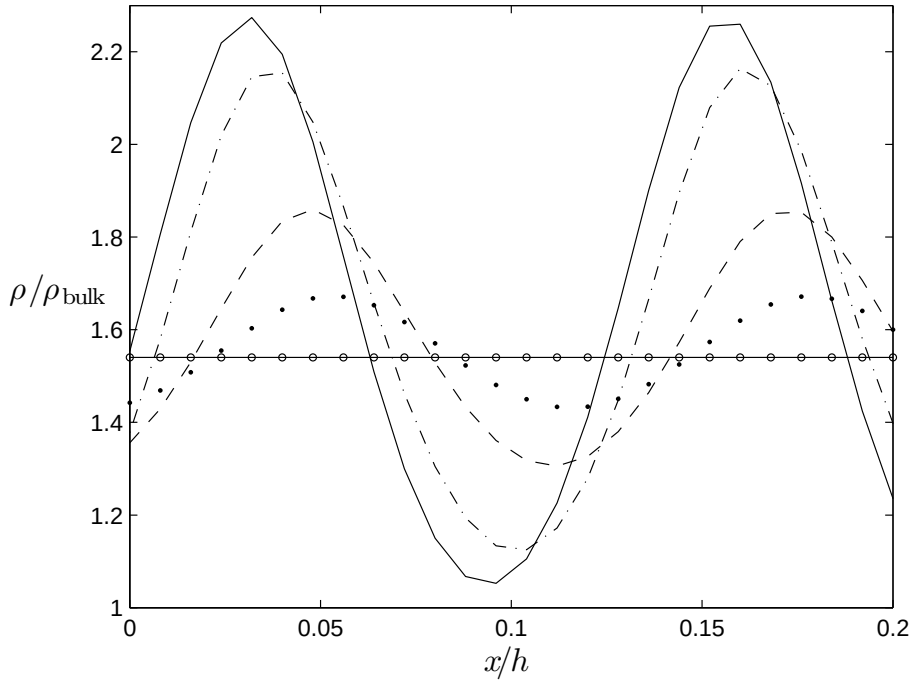

Figure 5.13. A zoomed in view of the density profile shown in Figure (5.12). Legend: $(-\text{o}-)$ $U^*_{top} = 10^2$, $(\cdots)$ $U^*_{top} = 2 \times 10^{-2}$, $(--)$ $U^*_{top} = 1.5 \times 10^{-2}$, $(-\cdot-)$ $U^*_{top} = 10^{-2}$, $(-)$ $U^*_{top} = 10^{-5}$.

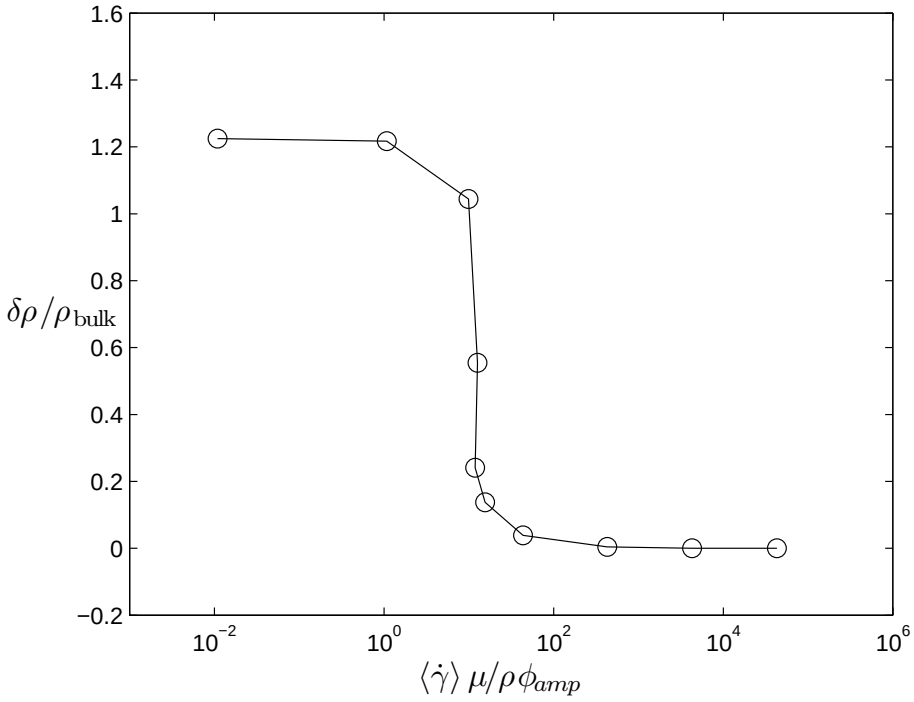

Figure 5.14. $\delta\rho/\rho_{bulk}$ vs. $\langle\dot{\gamma}\rangle\mu/\rho\phi_{amp}$ that includes cases depicted in Figure (5.12).

where $\langle\cdot\rangle$ indicates average with respect to the x direction. Integrating this equation with respect to the y direction yields

$$\tau_1 - \tau_2 = \int\int \rho \frac{\partial \phi}{\partial x} dxdy, \tag{5.23}$$

where τ_1 is the total shear force on the fluid at the top boundary of the domain and directed in the positive x direction. τ_2 is the total shear force on the fluid at the bottom boundary of the domain and directed in the negative x direction.

The limiting velocity profiles at low and high shear rates in Figure (5.9) can be discussed in the context of equations (5.22) and (5.23). At low shear rates, the body force due to the potential on the right hand side of equation (5.22) is non-zero in the first layer of fluid molecules, and rapidly decays in the outer regions. That gives rise to a velocity profile for $\langle u\rangle$ that is non-linear in the first layer and linear beyond that. Consequently, the total shear forces at the top and bottom walls are different with the difference being equal to the right hand side of equation (5.23).

At high shear rates, the density profile is almost constant with respect to the x direction (Figures 5.12-5.14). The body force due to the potential on the right hand sides of equations (5.22) and (5.23) are zero if the density does not vary with the x direction. Thus, the force due to the wall potential plays no role in the force balance at high shear rates. It follows from equation (5.22) that the velocity profile for $\langle u\rangle$ is linear and consequently $\tau_1 - \tau_2 = 0$. This is in agreement with the velocity profiles in Figure (5.9).

All the terms in equation (5.23) can be calculated from the numerical solution. In Figure (5.15) we confirm that equation (5.23) is indeed satisfied by the numerical results. The plots for the left and right hand sides of equation (5.23) are in excellent agreement at all values of the imposed shear rates. Specifically, it is noted that the body force due to the potential is important only at low shear rates and negligible at high shear rates. This is consistent with the trends of the velocity and density profiles discussed above.

It was confirmed that the above force balance is valid for all the cases considered in this chapter.

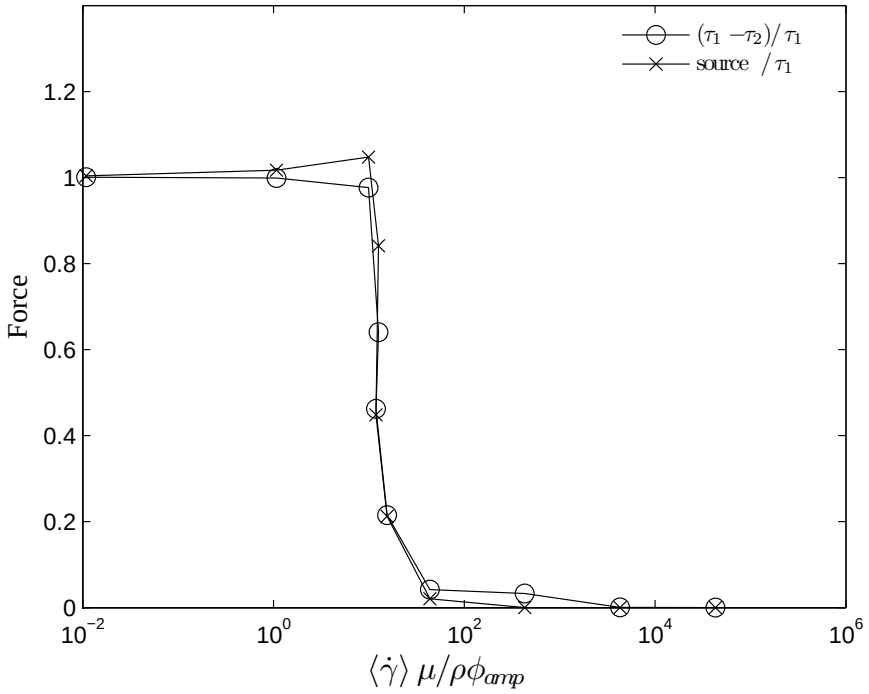

Figure 5.15. Verification of force balance given by equation (5.23). The variable "source" is the net body force due to the potential given by the right hand side of equation (5.23). The parameters are the same as those for Figures (5.9) and (5.12).

5.6.2.3. Estimation of the critical shear rate for transition. The scale of the body force term due to the potential, on the right hand side of equation (5.22), is $\rho_{\text{bulk}}\phi_{amp}b/\lambda$, where λ is the wavelength of the potential ϕ along the x direction. Similarly, the scale of the net viscous force on the left hand side of equation (5.22) is $\mu U_{top}/h^2$. At high shear rates the viscous term dominates the body force due to the potential. Thus, for transition from low shear rate behavior to high shear rate behavior to occur the following condition must be satisfied:

$$\left.\begin{aligned} &\frac{\mu U_{top}}{h^2} \gg \frac{\rho_{\text{bulk}}\phi_{amp}b}{\lambda}, \\ &\Rightarrow \frac{U_{top}\mu}{h\rho_{\text{bulk}}\phi_{amp}} \gg \frac{h}{\lambda}b, \\ &\Rightarrow \frac{\langle\dot{\gamma}\rangle\mu}{\rho_{\text{bulk}}\phi_{amp}} \gg \frac{h}{\lambda}b, \end{aligned}\right\} \tag{5.24}$$

where it is assumed that $\langle\dot{\gamma}\rangle \sim U_{top}/h$. Note that $h/\lambda = 8$ in our simulations because we have $n^* = 16\pi$, and $b = b^* = 1$ in all cases except some in section (5.6.5). Thus, for these parameters the transition to high shear rate behavior should be expected when $\frac{\langle\dot{\gamma}\rangle\mu}{\rho_{\text{bulk}}\phi_{amp}} \sim 8$. This estimate is in agreement with the results shown in Figures (5.8), (5.14) and (5.15). It is also in qualitative agreement with the estimate based on molecular scale analysis [**3**].

Equation (5.24) also explains the non-dimensionalization of the shear rate $\langle\dot{\gamma}\rangle$ in Figures (5.8), (5.14) and (5.15).

5.6.3. Effect of friction coefficient f_w on the slip length

At high shear rates, the limiting velocity profile is linear and determined completely by the boundary condition at the top and bottom boundaries. Thus, the slip length at high shear rate is fully determined by the friction coefficient f_w. This will be shown in this section.

To study the effect of the friction coefficient, especially at high shear rates, simulations with the following parameters are considered: $\mu^* = 10$, $\phi_a = 0.01$, $k^* = 8.5$, $m^* = n^* = 16\pi$, and $b^* = 1$. Different values of f_w are chosen. For each value of f_w, shear flows are solved for a range of values of U^*_{top}. As discussed in section (5.6.1) velocity profiles for different imposed values of shear rate are plotted and the slip length is computed.

Figure (5.16) shows a plot of slip length vs. non-dimensional shear rate for different values of f_w. It is seen that the slip length is constant at low shear rates and increases beyond the critical shear rate as estimated in equation (5.24). The slip length at high shear rates is unbounded if $f_w = 0$, and equal to another constant value for non-zero values of f_w. Thus, the high shear rate slip length crucially depends on f_w. It arises because of frictional heat loss to the solid molecules as shown in prior MD simulations [**55, 3**]. If MD calculations are done with rigidly fixed wall molecules, then the liquid molecules cannot dissipate energy to the wall molecules. This implies that the effective friction coefficient $f_w = 0$ for such simulations. These type of simulations were reported by [**2**] (see Figure 5.2). Their slip length was indeed unbounded in agreement with the trend in Figure (5.16) [**55, 3**].

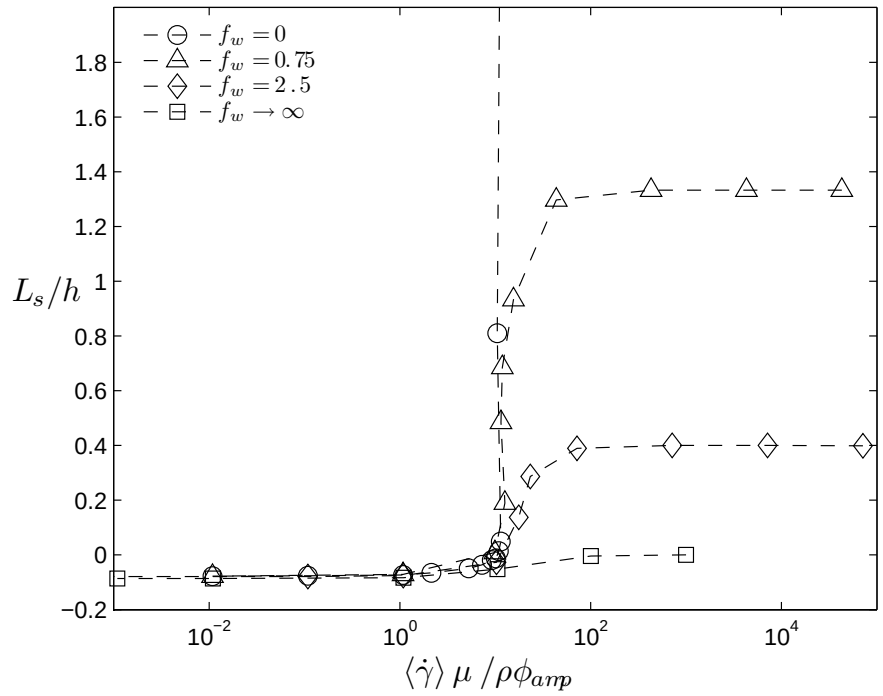

Figure 5.16. The slip length as a function of nondimensional shear rate at different values of $f_w = \eta_w h/\mu$. The fixed parameters are: $\mu^* = 10$, $\phi_a = 0.01$, $k^* = 8.5$, $m^* = n^* = 16\pi$, and $b^* = 1$.

Next we quantitatively verify that the high shear rate slip length is indeed solely determined by f_w. At high shear rates the x averaged velocity $\langle u\rangle$ is governed by

$$\frac{d^2\langle u\rangle}{dy^2} = 0, \tag{5.25}$$

which follows from equation (5.22) and the fact that the body force due to the potential is negligible. The x averaged boundary conditions become:

$$\begin{cases} \langle u\rangle = U_{top}, \text{at } y = h, \\ \mu\dfrac{d\langle u\rangle}{dy} = \eta_w\langle u\rangle, \text{at } y = 0. \end{cases} \tag{5.26}$$

The solution for $\langle u\rangle$ is:

$$\frac{\langle u\rangle}{U_{top}} = \frac{1}{(f_w+1)}(f_w(\frac{y}{h}) + 1). \tag{5.27}$$

We verified that the high shear rate limiting velocity profiles are the same as that given by equation (5.27) for all the cases considered. The slip length at high shear rate follows from the Navier boundary condition:

$$\frac{L_s}{h} = \frac{\mu}{\eta_w h} = \frac{1}{f_w}. \tag{5.28}$$

Figure (5.17) shows that the slip length obtained from Figure (5.16) is in agreement with the theoretical prediction in equation (5.28).

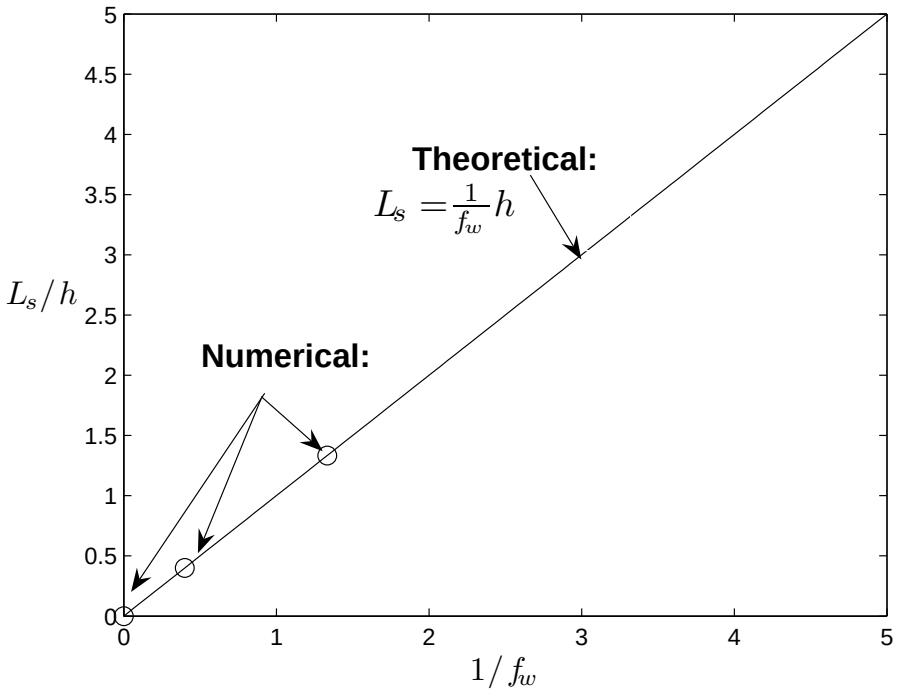

Figure 5.17. A comparison of the slip length obtained from Figure (5.16) with the theoretical prediction in equation (5.28).

5.6.4. Effect of ϕ_a on the slip length

To test the effect of ϕ_a, which is the non-dimensional amplitude of the potential, the following parameters are fixed: $\mu^* = 10$, $k^* = 8.5$, $m^* = n^* = 16\pi$, $b^* = 1$, and $f_w = 0.75$. Figure (5.18) shows the plot of slip length vs. the non-dimensional shear rate at different values of ϕ_a. As expected [**2**], the slip length increases as ϕ_a decreases. This is because the body force on the first fluid layer is smaller at smaller values of ϕ_a, thus allowing greater slip. The value

of ϕ_a has no influence on the slip length at high shear rates because it depends only on f_w as discussed in the previous section. Note that the non-dimensional shear rate at which the slip length transitions to its high shear rate value is approximately same for all values of ϕ_a. This implies that the effect of ϕ_{amp} on the transition is fully accounted for in the scaling of the shear rate. This further supports the estimation for the critical shear rate for transition given in equation (5.24).

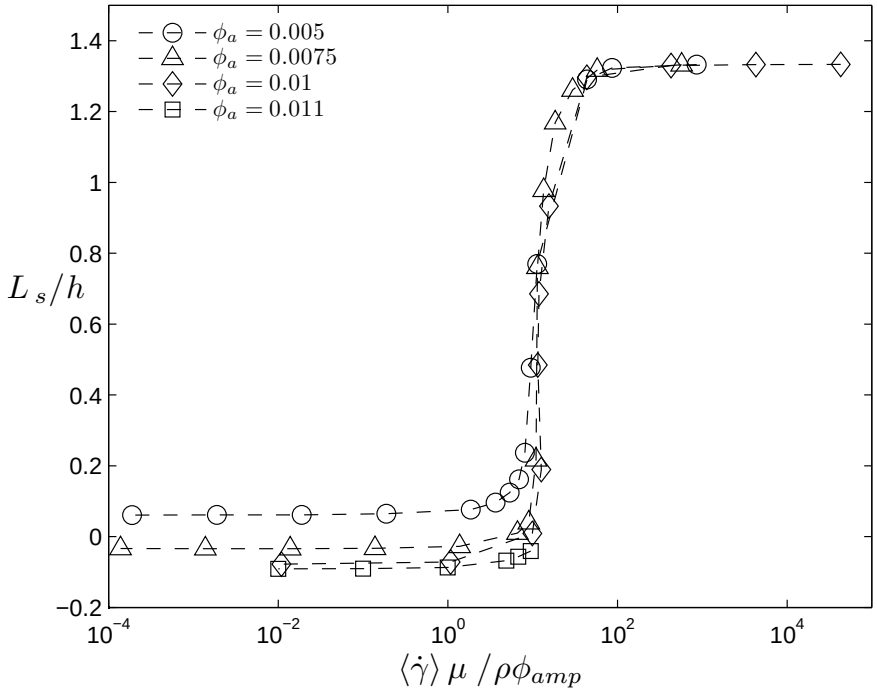

Figure 5.18. The slip length as a function of the non-dimensional shear rate for different values of ϕ_a. The fixed parameters are: $\mu^* = 10$, $k^* = 8.5$, $m^* = n^* = 16\pi$, $b^* = 1$, and $f_w = 0.75$.

Figure (5.19) shows the constant slip length at low shear rates in Figure (5.18) as a function of ϕ_a. A non-linear reduction in slip length with increasing ϕ_a is observed. A formal explanation of this trend based on a theoretical solution of the limiting velocity profile at low shear rates is being explored.

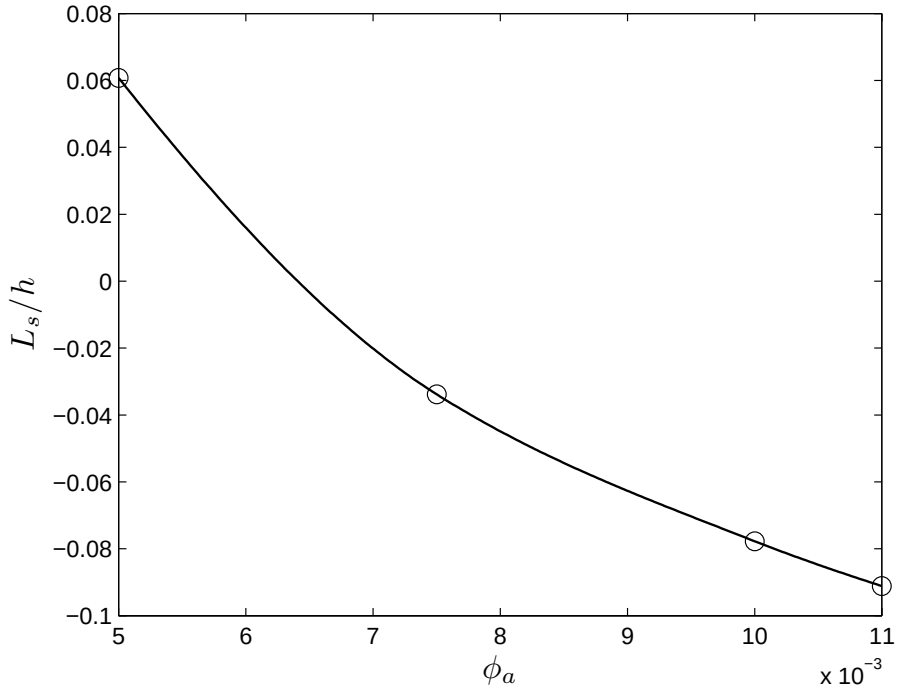

Figure 5.19. The low shear rate slip length vs. ϕ_a in Figure (5.18).

5.6.5. Effect of b^* on the slip length

The effect of b^* is expected to be similar to that of ϕ_a. To that end, simulations are done with the following fixed parameters: $\mu^* = 10$, $\phi_a = 0.01$, $k^* = 8.5$, $m^* = n^* = 16\pi$, and $f_w = 0$. Figure (5.20) shows the plot of slip length vs. the non-dimensional shear rate at different values of b^*. The slip length increases as b^* decreases. Less corrugated potential leads to greater slip at low shear rates.

Figure (5.21) shows the constant slip length at low shear rates from Figure (5.20) as a function of b^*. A non-linear reduction in slip length with increasing b^* is observed; a theoretical explanation for which is being explored.

Equation (5.24) implies that the critical shear rate for transition should scale linearly with b^*. Figure (5.20) shows that the critical shear rate for transition indeed increases as b^* increases. However, we find that this increase is non-linear and closer to quadratic, i.e. scales with b^{*2}, for this case where there is no friction at the bottom wall ($f_w = 0$). To show this we normalized the shear rate by b^{*2} and re-plotted the data from Figure (5.20) in Figure

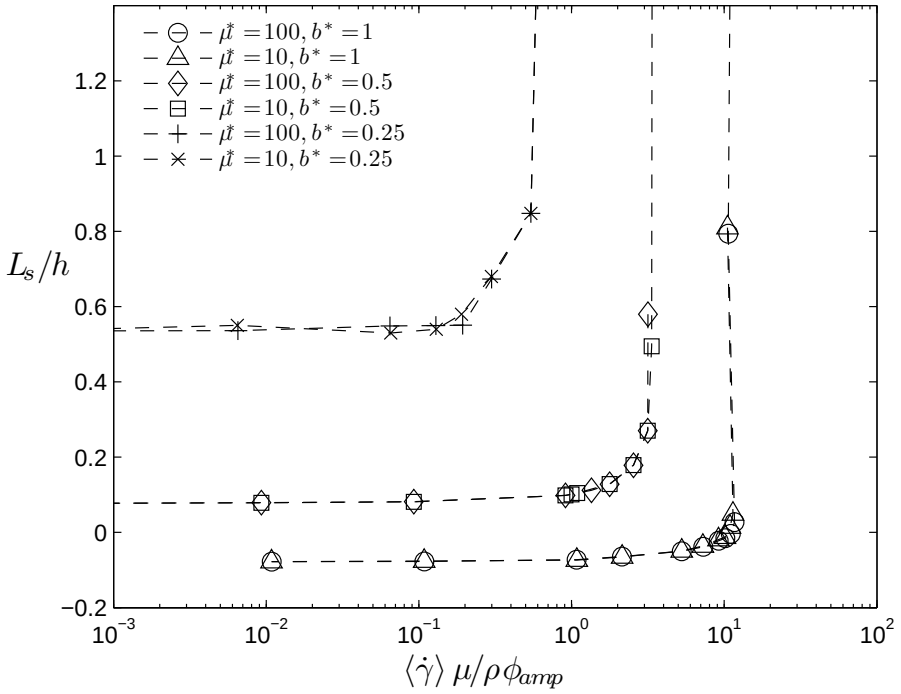

Figure 5.20. The slip length as a function of the non-dimensional shear rate for different values of b^*. The fixed parameters are: $\mu^* = 10$, $\phi_a = 0.01$, $k^* = 8.5$, $m^* = n^* = 16\pi$, and $f_w = 0$.

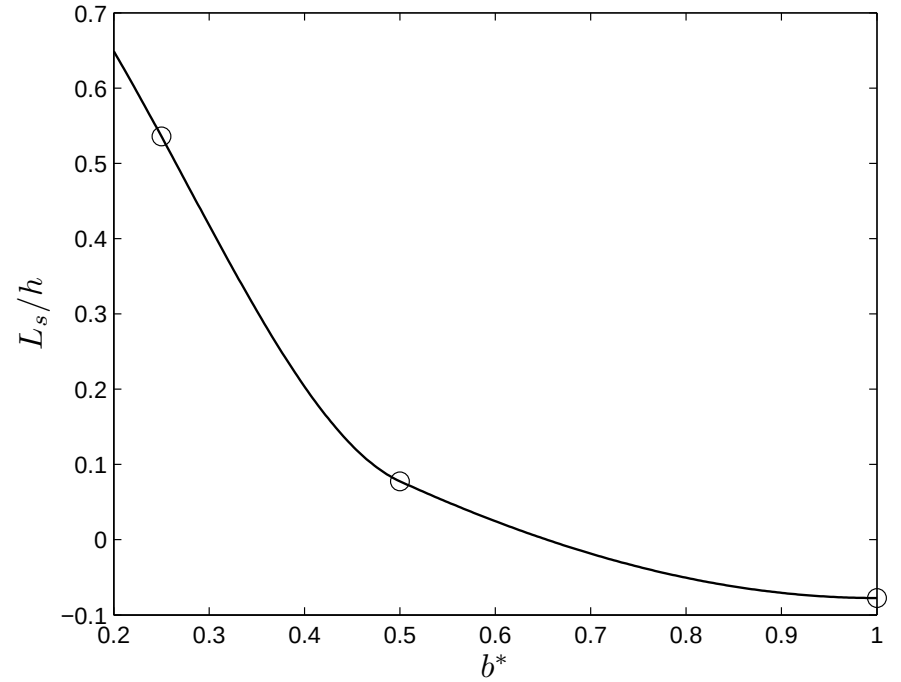

Figure 5.21. The low shear rate slip length vs. b^* in Figure (5.20).

(5.22). The b^{*2} scaling could be due to non-linear effects in the governing equations that become important when slip is large for cases with $f_w = 0$.

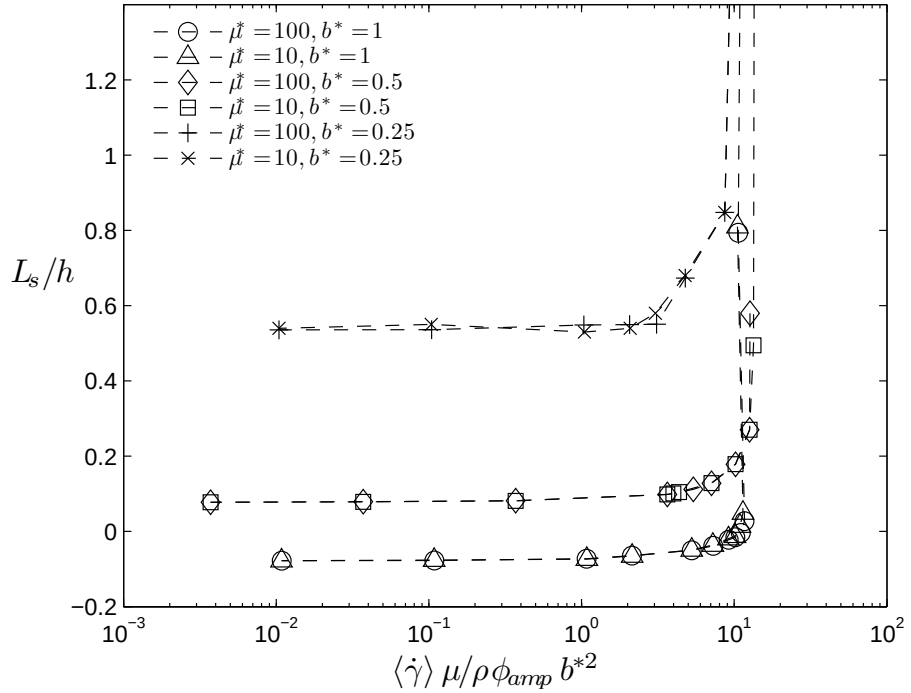

Figure 5.22. The slip length as a function of the non-dimensional shear rate normalized by b^{*2} for different values of b^*. The data are same as that in Figure (5.20)

5.7. Conclusion

In this chapter we asked the question: Is it possible to reproduce molecular scale slip behavior by using continuum equations? To that end we noted that: i) near the wall, the fluid experiences a potential, ii) the fluid density responds to the wall potential, hence, fluid compressibility is relevant, and iii) the fluid can loose momentum to the wall. To incorporate these features we simulated shear flow of a compressible fluid in the presence of a wall potential. It was found that compressibility is important only in the near wall region. The slip length was calculated from the mean velocity profile. The slip length vs. shear rate trend was found to be similar to that in molecular dynamic calculations. First, there is a constant value of slip length at low shear rates. Then, the slip length increases

beyond a critical shear rate. Lastly, the slip length reaches another constant value if the wall friction coefficient is non-zero. The scaling for the critical shear rate emerged from our results. The value of the slip length increases if the wall potential is less corrugated and if the momentum loss to the wall is low. An understanding of the overall force balance during various slip modes emerged from the governing equations. This work could be useful to develop continuum simulation tools for nanoscale problems without the need for expensive hybrid computations.

CHAPTER 6

Conclusion

This thesis is summarized as:

(1) Instability in electrolytic system also called "electrokinetic" instability has been studied.(Chapter 2 and Chapter 3)

(2) A direct numerical simulation scheme has been developed to solve the motion of a single particle under a DC or AC electric field. (Chapter 4)

(3) A continuum approach with an external wall potential to capture the molecular scale slip phenomenon has been developed. (Chapter 5)

6.1. Micromixing of fluid region

The instability at the interface between two miscible liquids with identical mechanical properties but different electrical conductivities was analyzed. Linear stability analysis was done by considering a sharp interface between adjacent liquids in the base state. This approach enabled, for the first time, an analytic solution for the critical condition of the electrokinetic instability. For the perpendicular electric field case, it was seen that the instability depends on a non-dimensional parameter P_Σ defined in the Equation (2.38). This parameter was not identified in any of the prior studies.

This approach also enabled an analysis of the mechanism of instability which was not clearly understood from prior work. Specifically, it was found that any velocity perturbation at the interface leads to a varying electrical conductivity in its vicinity due to the electrohydrodynamic coupling in the following interface condition

$$\|\sigma\mathbf{u} - D_\sigma \nabla\sigma\| \cdot \mathbf{n} = 0. \tag{6.1}$$

The above interface condition as the source of electrohydrodynamic coupling was not previously identified. This in turns leads to a bulk charge density that gives a body force in the fluid equations. The body force generates a cellular motion that results in the instability.

We showed, consistent with prior experimental results, that the perpendicular electric field case is more unstable compared to the parallel electric field case. The reason for this is the greater asymmetry in the perpendicular field case that results in larger destabilizing electrohydrodynamic force.

Detailed experimental investigation of the perpendicular electric field case is not available in literature at this time. Hence, a quantitative comparison with experiments is not possible in this case like it was possible for the parallel electric field case [**37**].

Typical experimental devices have microchannels. We also consider the geometry effect in Chpater 3. The future work will be focused on solving the instability problem in an AC electric field. Also we know that mixing is not always desirable. The application of field ampliefied sample stacking (FASS) which involves fluid regions with different ionic strengths and species which induced intabilities under electric field is desirable and is known to decrease the separation efficiency. We will have to solve additional equations for the concentration of the charge species.

6.2. Self-Assembly

A numerical technique for fully coupled simulation of electrohydrodynamic particulate flows was developed. Such a tool was not reported previously in literature and has potential use in several micro- and nano-scale fabrication processes that rely on electrohydrodynamic self-assembly of particles. We have tested this approach for all the basic dielectrophoretic behaviors expected in DC and AC fields. Further development of this approach was undertaken in collaboration with Prof. W.-K. Liu, and more details on its quantitative performance and its application to carbon nanotubes can be found elsewhere [**44**]. A prolate spheroid simulation can be done in our future work. It can help us to understand the self-assembly of carbon nanotubes in microfluidics. Our approach could lead to study aggregation and

cluster formation. We should also consider the Brownian motion effect by using fluctuating hydrodynamic equations for micron/nanoscale objects.

6.3. Continuum approach to study the fluid slip

We asked the question: Is it possible to reproduce molecular scale slip behavior by using continuum equations? To that end we noted that: i) near the wall, the fluid experiences a potential, ii) the fluid density responds to the wall potential, hence, fluid compressibility is relevant, and iii) the fluid can loose momentum to the wall. To incorporate these features we simulated shear flow of a compressible fluid in the presence of a wall potential. It was found that compressibility is important only in the near wall region. The slip length was calculated from the mean velocity profile. The slip length vs. shear rate trend was found to be similar to that in molecular dynamic calculations. First, there is a constant value of slip length at low shear rates. Then, the slip length increases beyond a critical shear rate. Lastly, the slip length reaches another constant value if the wall friction coefficient is non-zero. The scaling for the critical shear rate emerged from our results. The value of the slip length increases if the wall potential is less corrugated and if the momentum loss to the wall is low. An understanding of the overall force balance during various slip modes emerged from the governing equations. This work could be useful to develop continuum simulation tools for nanoscale problems without the need for expensive hybrid computations.) The future work will be focused on the slip behavior under the effect of channel height.

References

[1] J. Chung, K. H. Lee, J. H. Lee, and R. Ruoff. Toward large-scale integration of carbon nanotubes. *Langmuir*, 20:3011, 2004.

[2] P. A. Thompson and S. M. Troian. A general boundary condition for liquid flow at solid surfaces. *Nature*, 389:360, 1997.

[3] A. Martini, A. Roxin, R. Q. Snurr, Q. Wang, and S. Lichter. Molecular mechanisms of liquid slip. *J. Fluid Mech.*, 600:257–269, 2008.

[4] C. S. Peskin. The immersed boundary method. *Acta Numerica*, 11:479–517, 2002.

[5] A. M. Roma, C. S. Peskin, and M. J. Berger. An adaptive version of the immersed boundary method. *J. Comput. Phys.*, 153:509, 1999.

[6] M. H. Oddy, J. G. Santiago, and J. Mikkelsen. Electrokinetic instability micromixing. *Anal. Chem*, 73:5822, 2001.

[7] B. D. Storey, B. S. Tilley, H. Lin, and J. Santiago. Electrokinetic instabilities in thin microchannels. *Phys. Fluids*, 17:018103, 2005.

[8] H. Lin, B.D. Storey, M. H. Oddy, C. H. Chen, and J. G. Santiago. Instability of electrokinetic microchannel flows with conductivity gradient. *Phys. Fluids*, 16:1922, 2004.

[9] F. E. P Mikkers, F. M. Everaerts, and Th. P. E. M. Verheggen. Concentration distributions in free zone electrophoresis. *Journal of Chromatography*, 169:1–10, 1979.

[10] R. Bharadwaj and J. G. Santiago. Dynamics of field-ampliefied sample stacking. *J. Fluid. Mech.*, 543:57, 2005.

[11] S. Iijima. Helical microtubules of graphitic carbon. *Nature*, 354:56, 1991.

[12] A. Nitzan and M. A. Ratner. Electron transport in molecular wire junctions. *Science*, 300:1384, 2003.

[13] J. Cumings and A. Zettl. Low-friction nanoscale linear bearing realized from multiwall carbon nanotubes. *Science*, 289:602, 2000.

[14] P. L. McEuen, M. S. Fuhrer, M. S, and H. Park. Single-walled carbon nanotube electronics. *IEEE Trans. Nanotech.*, 1:78, 2002.

[15] J. Koplik, J. R. Banavar, and J. F. Willemsen. Molecular dynamics of fluid flow at solid surfaces. *Phys. Fluids A*, 1:781, 1989.

[16] C. Neto, D. R. Evans, E. Bonaccurso, H. J. Butt, and V. S. J. Craig. Boundary slip in newtonian liquids: a review of experimental studies. *Rep. Prog. Phys.*, 68:2859, 2005.

[17] Y. Zhu and S. Granick. Rate-dependent slip of newtonian liquid at smooth surfaces. *Phys. Rev. Lett.*, 87(9):096105, 2001.

[18] L. Bocquet and J. L. Barrat. Large slip effect at a nonwetting fluid-solid interface. *Phys. Rev. Lett.*, 82(23):4671, June 1999.

[19] L. Bocquet and J. L. Barrat. Influnce of wetting properties on hydrodynamic boundary conditions at a fluid/solid interface. *Farady Discuss*, 112:119, 1999.

[20] A. Martini, Y. Liu, R. Q. Snurr, and Q. Wang. Molecular dynamics charaterization of thin film viscosity for ehl simulation. *Tribol. Lett.*, 21(3):217, 2006.

[21] S. Lichter, A. Martini, R. Q. Snurr, and Q. Wang. Liquid slip as a rate process. *Phys. Rev. Lett.*, 98(22):226001, 2007.

[22] S. Lichter, A. Roxin, and S. Mandre. Mechanisms for liquid slip at solid surfaces. *Phys. Rev. Lett.*, 93(8):086001, August 2004.

[23] N. V. Priezjev and S. M. Troain. Molecular origin and dynamics behavior of slip in sheared polymer films. *Phys. Rev. Lett.*, 92(1):018302, 2004.

[24] P. A. Thompson and M. O. Robbins. Shear flow near solids: Epitaxial order and flow boundary conditions. *Phys. Rev. A*, 41(12):6830, 1990.

[25] R. Pit, H. Hervet, and L. Leger. Direct experimental evidence of slip in hexadecane: solid interfaces. *Phys. Rev. Lett.*, 85(5):980, 2000.

[26] L. Bocquet and J. L. Barrat. Influence of wetting properties on the hydrodynamic boundary condition at a fluid-solid interface. *Soft Matter*, 3:658, 2007.

[27] J. K. Holt, H. G. Park, Y. Wang, M. Stadermann, A. B. Arthyukhin, C. P. Grigoropoulos, A. Noy, and O. Bakajin. Fast mass transport through sub-2-nanometer carbon nanotubes. *Science*, 312:1034, 2006.

[28] M. Majumder, N. Chopra, R. Andrews, and B. J. Hinds. Nanoscale hydrodynamics: enhanced flow in carbon nanotubes. *Nature*, 438:44, 2005.

[29] M. Urbakh, J. Klafter, D. Gourdon, and J. Israelachvili. The nonlinear nature of friction. *Nature*, 430:525, 2004.

[30] D. S. Sholl and J. K. Johnson. Making high-flux membranes with carbon nanotubes. *Science*, 312:1003, 2006.

[31] J. C. T. Eijkel and A.can den Berg. Nanofluidics: what is it and what can we expect from it? *Microfluid. Nanofluid*, 1:249, 2005.

[32] J. M. Haile. *Molecular Dynamics Simulation*. John Wiley and Sons,Inc, 1997.

[33] M. H. Oddy and J. G. Santiago. Multiple-species model for electrokinetic instability. *Phys. Fluids*, 17:064108, 2005.

[34] S. Pennathur and J.G. Santiago. Electrokinetic transport in nanochannels. 1. theory. *J. Colloid Interface Sci.*, 261:402–410, 2003.

[35] Chen, H. Lin, S. K. Lele, and J. G. Santiago. Convective and absolute electrokinetic instability with conductivity gradients. *J. Fluid Mech.*, 524:263, 2005.

[36] K. Jonathan. Honey, i shrunk the lab. *Nature*, 418:475, 2002.

[37] N. A. Patankar. Electrokinetic mixing instability: The sharp interface limit. *Phys. Fluids*, submitted.

[38] D. Saville. Electrohydrodynamics: The Taylor-Melcher leaky dielectric model. *Ann. Rev. Fluid Mech.*, 29:27, 1997.

[39] J. Hoburg and J. R Melcher. Internal electrohydrodynamic instability and mixing of fluids with orthogonal field and conductivity gradients. *J. Fluid Mech.*, 73:333, 1976.

[40] J. R. Melcher. *Continuum Electromechanics*. MIT Press, 1981.

[41] P. K. Kundu and I. M. Cohen. *Fluid Mechanics*. Elsevier Academic Press, third edition, 2004.

[42] H. A. Pohl. The motion and precipitation of suspensoids in divergent electric fields. *J. Appl. Phys*, 22:869–871, 1951.

[43] W. K. Liu, Y. Liu, D. Farrell, L. Zhang, X. S. Wang, Y. Fukui, N. A. Patankar, Y. Zhang, C. Bajaj, J. Lee, J. Hong, X. Chen, and H.Y. Hsu. Immersed finite element method and its applications to biological systems. *Computer Methods in Applied Mechanics and Engineering*, 195:1722–1749, 2006.

[44] Y. Liu, W. K. Liu, T. Belytschko, N. A. Patankar, A. To, A. Kopacz, and J. H. Chung. Immersed electrokinetic finite element method. *Internal Journal for Numerical Methods in Engineering*, 71(4):379–405, 2007.

[45] T. B. Jones. *Electromechanics of Particle*. Cambridge University Press, 1995.

[46] F. A. Sauer. Force on suspended partilces in the electromagnetic field. *Coherent excitations in biology systems*, page 134, 1983.

[47] N. A. Patankar, P. Singh, D. D. Joseph, and R. Glowinski. A new formulation of the distributed lagrange multiplier/fictious domain method for particulate flows. *Int. J. Multiphase Flow*, 26:1509–1524, 2000.

[48] N. Sharma and N. A. Patankar. Direct numerical simulation of the brownian motion of particles by using fluctuating hydrodynamic equations. *J. Comput. Phys.*, 201(2):466–486, 2004.

[49] N. Sharma. *Direct Numerical Simulation of particulate flows for three different length scales: Macro, Micro, and Meso*. Thesis, 2005.

[50] H. H. Hu. Direct simulation of flows of solid-liquid mixtures. *Int. J. Multiphase Flows*, 22:335, 1996.

[51] H. H. Hu, N. A. Patankar, and M. Y. Zhu. Direct numerical simulations of fluid solid using arbitrary lagrangian-eulerian technique,. *J. Comput. Phys*, 169:427, 2001.

[52] H. H. Hu, D. D. Joesph, and M. J. Crochet. Direct numerical simulation of fluid particle motions. *Theoret. Comput. Fluid Dyn*, 3:285, 1992.

[53] J. Kim and P. Moin. Application of a fractional-step method to incompressible Navier-Stokes equations. *Journal of Computational Physics*, 59(2):308, JUN 1985.

[54] S. V. Patankar. *Numerical Heat Transfer and Fluid Flow*. Hemisphere Pub, June 1980.

[55] A. Martini, H. Y. Hsu, N. A. Patankar, and S. Lichter. Slip at high shear rate. *Phys. Rev. Lett.*, 100:206001, 2008 June.

[56] E. Bonnacurso, M. Kappl, and H.J. Butt. Hydrodynamics force measurement: Boundary slip of water on hydrophilic surface and electrokinetic effect. *Phys. Rev. Lett.*, 88(7):076103, 2002.

[57] Y. Zhu and S. Granick. Rate-dependent slip of a newtonian liquid at smooth surfaces. *Phys. Rev. Lett.*, 87, 2002.

[58] C. H. Choi, K. Johan, A. Westin, and K. S. Breuer. Apparent slip flow in hydrophilic and hydrophobic microchannels. *Phys. Fluids*, 15(10):2897, 2003.

[59] D. C. Tretheway and C. D. Meinhart. Apparetn fluid slip at hydrophobic microchannel walls. *Phys. Fluids*, 14(3):2001, 2001.

[60] N. G. Hadjiconstantinou. Hybrid atomistic-continuum formulations and the moving contact-line problem. *J. Comput. Phys.*, 154:245, 1999.

[61] X. B. Nie, S. Y. Chen, W. N. E, and M. O . Robbins. A continuum and molecular dynamics hybrid method for micro- and nano-fluid flow. *J. Fluid Mech.*, 500:55, 2004.

[62] X. Zhang, Y. Zhu, and S. Granick. Hydrophobicity at a janus interface. *Science*, 295:663, 2002.

[63] D. A. Doshi, E. B. Watkins, J. N. Israelachvili, and J. Majewski. Reduced water density at hydrophobic surfaces: Effect of dissolved gases. *PNAS*, 102(27):9458, 2005.

[64] A. Jabbarzadeh, J. F. Atkinson, and R. I. Tanner. Rheological properties of thin liquid films by molecular dynamics simulations. *Newtonian Fluid Mech.*, 77:2612, 1998.

[65] R. Khare, J. J. de Pablo, and A. Yethiraj. Rheology of confined polymer melts. *Macromolecules*, 29:7910, 1996.

[66] S. A. Gupta, H. D. Cochran, and P. T. Cummings. Molecular dynamics simulations of the rheology of normal decane, hexadecane, and tetracosane. *J. Chem. Phys.*, 107:10316, 1997.

[67] N. V. Priezjev. Effect of surface roughness on rate-dependent slip in simple fluids. *J. Chem. Phys.*, 127:144708, 2007.

[68] Fluent INC. ANSYS, 2007.

[69] W. A. Steele. The physical interaction of gases with crystalline solids *1 i. gas-solid energies and properties of isolated adsorbed atoms. *Surf. Sci.*, 36:317–352, 1973.